5-2014

TARGETING BREAST CANCER WITH BACTERIOPHAGE ASSOCIATED SILICON PARTICLES

Srimeenakshi Srinivasan

TARGETING BREAST CANCER WITH BACTERIOPHAGE ASSOCIATED SILICON PARTICLES

by

Srimeenakshi Srinivasan, B.D.S., M.S.

APPROVED:

_____
Mauro Ferrari, Ph.D. – Advisory Professor

_____
Biana Godin-Vilentchouk, Ph.D.

_____
David Gorenstein, Ph.D. – Chair, Advisory committee

_____
Menashe Bar-Eli, Ph.D.

_____
Funda Meric-Bernstam, MD

APPROVED:

_____
Dean, The University of Texas
Graduate School of Biomedical Sciences at Houston

TARGETING BREAST CANCER WITH BACTERIOPHAGE ASSOCIATED SILICON PARTICLES

A

DISSERTATION

Presented to the Faculty of

The University of Texas

Health Science Center at Houston

and

The University of Texas

MD Anderson Cancer Center

Graduate School of Biomedical Sciences

in Partial Fulfillment

of the Requirements

for the Degree of

DOCTOR OF PHILOSOPHY

by

Srimeenakshi Srinivasan, B.D.S., M.S.

Houston, Texas

May, 2014

Dedication

This thesis is dedicated to my wonderful husband, Diwakar, and my dear son, Chinmay. Thank you for being there for me when I needed you the most and for being a constant source of support and encouragement during the challenges of school and life. I am truly thankful for having you in my life and give my deepest expression of love and appreciation for all the sacrifices you made during this graduate program. This thesis would have not been possible without you. I am eternally grateful. You are everything to me. I love you, always and forever.

I would also like to dedicate this work to my parents, Jaya Srinivasan and Srinivasan Thiagarajan and my brother, Shivkumar Srinivasan, who have always loved me unconditionally and whose good examples have taught me to work hard and not give up at any hardship.

This work is also dedicated to my parents-in-law, Meenakshi Ramamurthy and Ramamurthy Subramaniam, who supported and encouraged my interest in pursuing research and was there for our family whenever we needed them.

Acknowledgements

I would first like to express my gratitude to my advisors Dr. Mauro Ferrari and Dr. Biana Godin for their guidance and support that was crucial for the development of my project. Their knowledge of the field and their attitude and passion for their job motivated me to persist in my professional goals.

I would also extend my utmost appreciation to my advisory, exam as well as my supervisory committee members: Dr. David Gorenstein, Dr. Menashe Bar-Eli, Dr. Funda Meric-Bernstam, Dr. Ananth Annapragada, Dr. Renata Pasqualini, Dr. Gabriel Loper-Berestein, Dr. Vasanthi Jayaraman and Dr. Chun Li, for the time they dedicated to me and their useful critiques that changed my approach to a scientific problem and helped me be a better researcher.

I am also thankful to Dr. Xuewu Liu for porous silicon particle fabrication, Dr. Kenji Yokoi, Dr. Tomonori Tanei, Dr. Fransisca Leonard and Dr. Enrica DeRosa for their contribution in the animal studies, Mr. Kenneth Dunner for his contributions with TEM microscopy, Mr. Matt Landry for the help with graphical renditions for journal covers.

My utmost gratitude to all my lab members, who are more my friends than co-workers – Jenolyn Alexander, Dr. Fransisca Leonard and Dr. Hamsa Jagannathan, my friends, Dr. Nicoletta Quattrocchi, Janani Krishnamurthy, Dr. Anu Ramabhadran, Dr. Arun Senthil Nathan and all the others for the tremendous assistance throughout my PhD training and for being there for me during all the insane times in my project where I was suffering with data and results and whenever I was feeling low. Their humor, love and support made

this journey easy for me and instilled confidence and kept me going. You are all like my family.

This research work was supported by DoD Breast Cancer Research Program Innovator Award (W81XWH-09-1-0212), NCI-NIH (1U54CA143837-01) and Alliance for Nanohealth (ANH) and NASA/DOE Graduate Student Research Training Fellowship 2009.

TARGETING BREAST CANCER WITH BACTERIOPHAGE ASSOCIATED SILICON PARTICLES

Srimeenakshi Srinivasan, Ph.D.*

Supervisory Professor: Mauro Ferrari, Ph.D.

Nanoparticle based therapeutics have been successfully used in the treatment of breast cancer. Development of nanovectors targeted to cancer cells or elements in the tumor microenvironment has been pursued to improve their site specific accumulation while reducing the non-specific delivery to normal tissues. However, addition of targeting ligands to the surface of nanovectors while maintaining their payload carrying potential is generally challenging. Therefore, there is a critical need to develop surface decoration strategies that allow for effective combination of targeting and payload delivery to the tumor.

In this study, we propose a novel strategy for covering the surface of mesoporous silicon particles (S1MP) with targeting entities (bacteriophage) and gold nanoparticles (AuNP) while maintaining their payload carrying potential. Retention of payload carrying potential after the formation of BASP was demonstrated by loading different types of nanoparticles and macromolecules into the porous structure of S1MP. Additionally, the BASP displayed enhanced near infrared (NIR) absorbance that could be used for thermal ablation of the tumor as well as for *in vivo* monitoring using NIR surface enhanced Raman spectroscopy (NIR-SERS). *In vitro* targeting studies under static and shear flow conditions, as experienced in healthy microvasculature ($100s^{-1}$), did not display significant targeting

efficiency of the CRKL targeted BASP. However, in shear rates relevant to the tumor microvasculature ($10s^{-1}$), CRKL targeted BASP demonstrated 2-fold higher adhesion than S1MP to endothelial cells. These results were further exaggerated in *in vivo* conditions evidenced by intravital microscopy studies that showed up to 4 fold increase in the number of CRKL targeted BASP accumulating in the tumor vasculature compared to both S1MP and fd-tet non-targeted BASP. *In vivo* experiments also showed that BASP maintain their integrity following intravenous administration in mice and a 3-fold higher tumor accumulation than S1MP. Furthermore, treatment of breast tumor bearing mice with Abraxane loaded CRKL targeted BASP showed significantly reduced tumor growth in comparison to Abraxane or Abraxane loaded S1MP controls. Overall, this study demonstrates a simple and efficient strategy to target S1MP to breast cancer while maintaining their ability to carry large amounts of therapeutic payload.

Table of Contents

List of Illustrations

List of Tables

CHAPTER 1: INTRODUCTION

1.1 Breast cancer as a disease

1.1.1 Pathophysiology

The structure of the female breast is complex – comprising of (i) milk producing glands called *lobules*, (ii) *ducts* that carry milk from the lobules to the nipple and (iii) *stroma* that is made up of connective tissue, blood vessels and lymphatic vessels (Figure 1). Breast cancer is a disease where cells in the breast divide and grow without normal control. Depending on the location of the tumor, breast cancer can be lobular or ductal. These can be further divided into invasive and non-invasive carcinoma. About 70 – 80% of breast cancers are invasive ductal carcinomas. A third type of cancer is inflammatory breast cancer where the cancer cells block the lymph vessels, causing redness and warmth in the breast. Breast cancers are staged according to the TNM staging given by the American Joint Committee on Cancer (AJCC), based on their tumor size (T), nodal involvement and size (N) and metastatic involvement (M). This staging is very important in deciding the overall prognosis and the treatment of patients. Staging is done by a combination of physical examinations, various imaging tests, such as x-ray and computed tomography (CT) scan, blood tests and biopsies. In spite of advancements in detection techniques, breast cancer is the second leading cause of cancer related deaths in women in the US [1]. Early detection techniques and primary tumor treatments have markedly improved, however occurrence of distant metastasis and the inefficiency in their treatment make breast cancer the second leading cause of cancer related death in women in the U.S. [2].

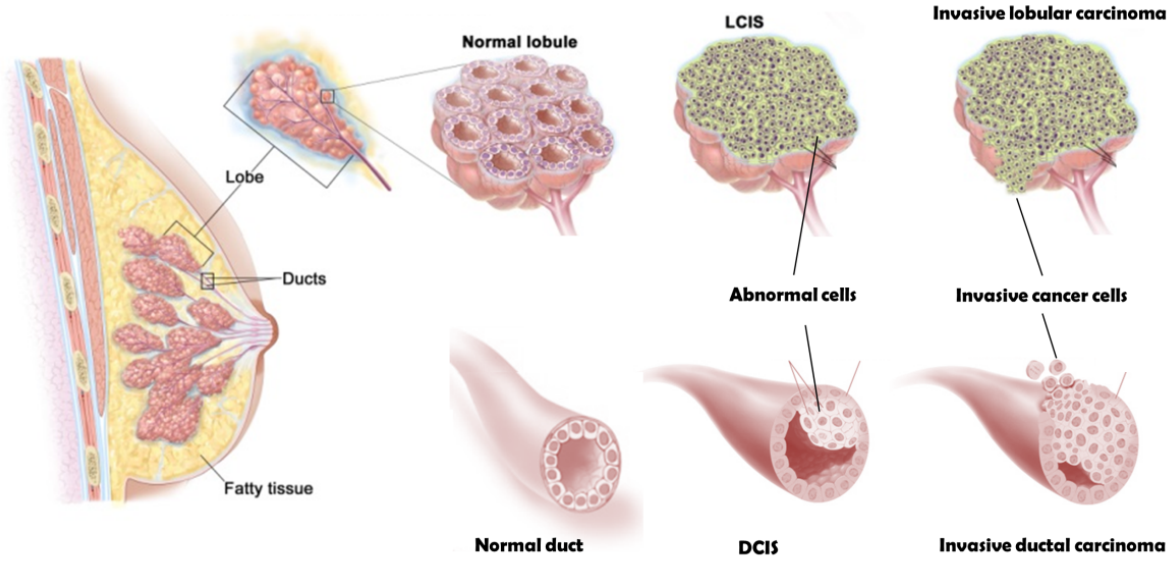

Figure 1: Schematics of breast cancer. Top row, lobular carcinoma and bottom row, ductal carcinoma. Adapted from the website of the National Cancer Institute (http://www.cancer.gov)

1.1.2 Current therapeutic strategies for breast cancer

Depending on the TNM staging the schedule of therapy varies. The first line therapy in breast cancer includes surgery, radiation therapy, cytotoxic chemotherapy, hormone therapy and targeted molecular therapy [3]. Surgery is usually prescribed when the tumor is localized and has defined margins. Radiation therapy typically follows surgery to help lower the chance of recurrence in the breast or nearby lymph nodes. Radiation is also the choice of treatment when distant metastases are seen. Chemotherapy is the treatment using cytotoxic drugs either injected intravenously or given orally. The most common cytotoxic chemotherapeutic drugs used in breast cancer include anthracyclines (Doxorubicin), taxanes (Paclitaxel) and platinum compounds (Cisplatin) among others. Nanoparticle formulations of doxorubicin (Doxil®)[4] and paclitaxel (Abraxane^{TM})[5] have also been successfully used in

the clinic for breast cancer therapy for many years now. Molecularly targeted therapeutic agents based on identified biomarkers are also used in combination with chemotherapeutic drugs. Examples include Herceptin® [6], a monoclonal antibody which interferes with overexpressed HER2 thereby inhibiting the cell proliferation caused by HER2. Another example is Lapatinib [7], a synthetic tyrosine kinase inhibitor that affects HER2 and epidermal growth factor receptor (EGFR) pathways. Table 1 lists therapeutic agents that are either clinically approved or under clinical trials.

Therapeutic agents currently used in the clinic			
Chemical name	**Brand name**	**Type**	**Mode of action**
Trastuzumab	Herceptin	Monoclonal antibody	HER-2/neu inhibitor
Lapatinib	Tykerb	Drug	Tyrosine kinase inhibitor
Bevacizumab	Avastin	Monoclonal antibody	Angiogenesis inhibitor
Pertuzumab	Perjeta	Monoclonal antibody	Prevents HER-2 dimerization
Everolimus	Afinitor	Drug	mTOR inhibitor
T-DM1	Kadcyla	Monoclonal antibody/drug conjugate	HER-2/neu inhibitor Antimitotic
Therapeutic agents under clinical trials			
Name	**Phase**	**Type**	**Mode of action**
AUY922	Phase I,II	Drug	Heat Shock Protein 90 inhibitor
BEZ235	Phase I	Drug	PI3 kinase inhibitor
BGT226	Phase I,II	Drug	PI3 kinase/mTOR inhibitor
PF-04691502	Phase II	Drug	PI3 kinase/mTOR inhibitor
XL765	Phase I,II	Drug	PI3 kinase/mTOR inhibitor
BKM120	Phase I	Drug	PI3 kinase inhibitor
GDC-0941	Phase I,II	Drug	PI3 kinase inhibitor
MK-2206	Phase I	Drug	Akt inhibitor
CDX-011	Phase II	Monoclonal antibody/drug conjugate	Antimitotic

Table 1: List of therapeutic agents used in clinic/under clinical trials for breast cancer. Source www.clinicaltrials.gov.

1.1.3 Disavantages of conventional chemotherapy

Conventional chemotherapeutic as well as targeted antibody molecules, when injected into the blood stream, either get degraded or sequestered by the reticuloendothelial system (RES). Further, owing to their small size, they easily penetrate the endothelial barrier and non-specifically enter the tissue space in any organ, leading to undesired cytotoxic side effects in uninvolved organs, such as hypersensitivity reactions (Paclitaxel) and cardiotoxicity (Doxorubicin) [8]. Thus, the probability of a drug molecule reaching the target site is as low as 1 in 100,000 molecules [9]. Due to the inefficiency of conventional chemotherapy and the low quality of life experienced by patients, better alternatives had to be identified. Nanomedicine showed promising results in improving both the quality and efficiency of treatments.

1.2 Nanomedicine research and its application in breast cancer

1.2.1 What is nanomedicine?

Nanomedicine is the field of medicine that employs materials that are themselves or have components in the nanoscale, i.e. 1 to 1000nm. Both designing nanovectors for delivery of diagnostic and therapeutic agents as well as precise patterning of surfaces are subfields of nanomedicine [10]. Owing to the small size of these nanovectors, their interactions with biological systems at the molecular level are unique. Various nanovectors have been developed for use in cancer detection, diagnosis, imaging, treatment and disease monitoring. Nanovectors may be made from a spectrum of materials including lipids, phospholipids, dextran, carbon, silica, gold and silver [11], among others. Nanovector design has evolved over the years. The first generation of nanovectors were generally composed of a single class of particles (liposome, micelle, etc.) encapsulating a payload and accumulates in the tumor

due to enhanced permeation and retention (EPR) effect. The accumulation of such nanovectors in the tumor cells solely depend on their size [12]. The second generation of nanovectors encompasses delivery systems with added functionalities such as decoration of the nanovector surface with targeting moieties for active targeting and active/triggered release of payload at site of action [13]. Active targeting refers to the biomolecular recognition of cancer cell surface epitopes by recognition moieties on nanovector surfaces, such as antibodies, peptides or aptamers. Contemporary nanovectors are more complex and may employ multiple classes of nanoparticles that are designed to perform distinct functions [13].

1.2.2 Advantages of nanovectors

Unlike conventional chemotherapeutic drugs that are small molecules able to cross most endothelial barriers and reach the tissue beyond, nanovectors are large enough to avoid transmigration across normal endothelial barrier, but small enough to "leak" through fenestrations in the tumor vasculature and concentrate in the tumor tissue [10]. The ability of nanovectors to carry substantial amounts of therapeutic agent to the intended site is the major advantage over conventional cytotoxic/immunotargeted drugs, whereas the chance of a drug molecule reaching the tumor site is only 1 in 100,000 [10]. Another important advantage of nanovectors is their protective effect on the payload. The first barrier faced by intravenously injected drugs or siRNA or monoclonal antibodies is degradation. Encapsulation of the therapeutic agent in nanoparticles protects the active ingredient from such degradation, until they reach the disease site. This protection of drug indirectly translates to minimized interaction with normal tissues by virtue of size exclusion, thereby reducing unwanted side effects [8]. While intravenously administered free drug molecules get cleared from the

plasma either through the kidneys (hydrophilic molecules [14]) or through enzymatic metabolism in the liver (lipophilic molecules [15]), larger nanovectors (< 15 nm is the renal cut off [16]) do not get cleared by the renal system quickly as well as protect the active ingredient from enzymatic metabolism in the liver [17] .

Many cancer chemotherapies rely on combination therapy, i.e. co-administration or sequential administration of multiple drugs, to overcome resistance and enhance the therapeutic efficacy. Multidrug encapsulation in nanoparticles has been demonstrated in various studies. Examples include doxorubicin loaded liposomes covered by layers of siRNA loaded poly-L-lysine films for the treatment of triple-negative breast cancer [18] and liposome encapsulated formulation of irinotecan and floxuridine for solid tumors [19]. This enhances the probability of 2 individual drugs reaching the same tumor site than when injected as free drug molecules [20].

Formulation of nanoparticles can be altered to facilitate sequential release of drugs, if required. For example, the biodegradability of most materials used in the design of nanovectors, facilitate the release of the payload after degradation [21]. Other approaches include pH [22] and/or heat triggered [23] release of the active ingredient. Nanoparticles are also beneficial due to their ability to penetrate cell membranes through receptor mediated endocytosis and lysosomal escape after endocytosis [24] thereby facilitating the release of drug directly inside the cells to enhance therapeutic effect.

1.2.3 Nanotechnology in breast cancer

Nanotechnology has made major contributions in breast cancer. Liposomal doxorubicin (Doxil®) was the first and representative nanovector that was approved for clinical use about two decades ago for Kaposi's sarcoma [25]. Now they have also been used

in breast [26; 27] and ovarian cancer [28]. Nanoparticle albumin-bound paclitaxel, Abraxane, is another drug that has been approved for metatstatic breast cancer therapy [29; 30]. There are a few more nanovectors that are undergoing clinical trials for the treatment of breast cancer, such as paclitaxel incorporating micelles [31] and TNF-bound colloidal gold (Aurmine) [32; 33]. A list of nanovectors clinically approved/under clinical trials for use in breast cancer therapy are summarized in Table 2. Other nanoparticle formulations for breast cancer therapy that are still under pre-clinical evaluation include polymeric nanoparticle encapsulating tamoxifen [34], adenovirus type 5 E1A (against ERBB2) [35], p53 loaded nanoparticles [36] and nanoparticle-siRNA complexes directed to *Ras* [37].

Nanoparticles have also been used for various other applications in breast cancer. Use of nanoparticles such as carbon nanotubes (CNT) [38], silicon nanowires (SiNW) [39], quantum dots [40], gold nanoparticles [41] and silver nanoparticles *ex vivo* has allowed rapid, label free, multiplexed detection of biomarkers at ultralow detection limits, which can contribute substantially to the early diagnosis and accurate prognosis of cancers [42]. *In vivo* tumor imaging using nanoparticles is also a very fast developing field of research. Magnetic nanoparticles such as superparamagnetic iron oxide nanoparticles (SPION) and bismuth sulfide nanoparticles [43] are attractive systems as they can be used as MRI contrast agents.

Therapeutic agent	Type	Clinical phase	Indication
Doxorubicin	Liposomal	Approved and in clinical trials	Breast cancer
	Magnetic targeted beads	Phase I,II	Liver metastasis
Paclitaxel	Abraxane	Approved and in clinical trials	Breast cancer
	Polymeric micelles	Phase IV	Breast cancer
	Synthetic phospholipids and cholesterol	Phase II	Breast cancer
siRNA against PLK1 gene product	Stable Nucleid Acid Lipid Particles (SNALP)	Phase I	Liver metastasis
Tumor Necrosis Factor	Colloidal gold	Phase 0	Breast cancer
Cytarabine	Liposomal	Phase II	CNS metastasis
Annamycin	Liposomal	Phase II	Anthracycline resistant breast cancer
Docetaxel	Liposomal	Phase I	Advanced breast cancer

Table 2: List of nanovectors clinically approved/under clinical trials for the use of breast cancer therapy. Source www.clinicaltrials.gov.

1.2.4 Limitations of currently investigated nanovectors

Inspite of all the advantages described in Chapter 1.2.2, other than the few nanovectors described above, no new nanovectors have been approved for clinical use in the last two decades. There are various challenges that need to be addressed to enable the design of more efficient nanovectors. Delivery of nanovectors to the tumor tissue faces various obstacles from the site of injection until they reach the tumor tissue. Some of the barriers include but are not limited to enzymatic degradation, recognition and sequestration by reticulo-endothelial system (RES) and vascular endothelium (Figure 2).

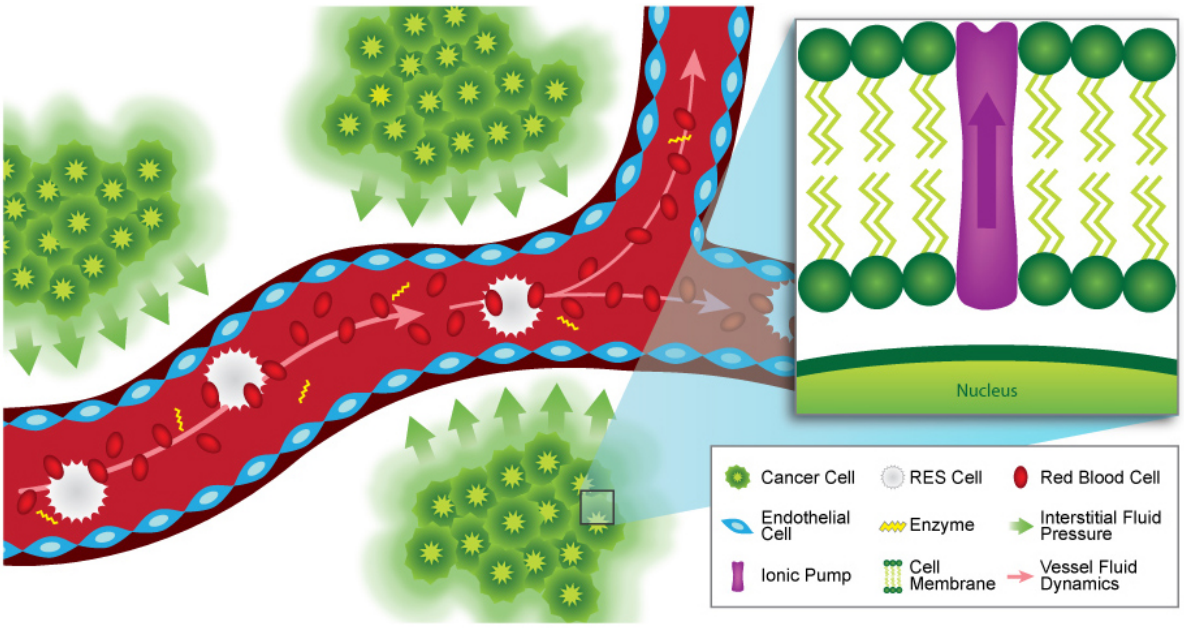

Figure 2: Sequential biological barriers experienced by a drug molecule or nanoparticle when in circulation from the point of injection to the tumor site. Reproduced with permission from [44].

Each of these barriers has to be overcome before the nanovector can efficiently deliver therapeutics to the tumor cells. Many strategies have been put forward for overcoming some of these barriers [45; 46]. For example, molecular targets on tumor cells have been used to advantage for homing nanoparticles to the tumor site. Various peptide [47], antibodies [48; 49], oligonucleotides [50; 51] and other molecules [52; 53] have been conjugated to the surface of nanoparticles to enhance tumor specific accumulation. However, the limited access of nanoparticles to the blood vessel walls diminishes the effectiveness of

the targeting moiety in enhancing nanoparticle accumulation in the tumor [54]. Another technique used for increasing tumor accumulation is the conjugation of polyethylene glycol (PEG) to the surface of nanoparticles, to delay or avoid their sequestration by the RES organs. PEGylation prevents opsonization of the particles by immune cells, thereby increasing the circulation time and chance for the nanovectors to accumulate in the tumor [55]. PEGylation, however, masks targeting moieties conjugated on nanoparticles, thus negating the advantage of targeting moieties [56]. Thus, we can understand that adding functionalities to a single nanoparticle doesn't solve the limitations. There is an emerging requirement for a multimodular nanoassembly, in which different components with individual and distinct functions act in a synergistic manner to circumvent each barrier sequentially.

1.3 Multistage nanovectors

1.3.1 Rational design

A nanovector must be able to travel from the site of injection to the tumor site after bypassing sequential biobarriers mentioned earlier. A single nanoparticle would not be able to overcome all of the barriers successfully. Thus far, tumor specific accumulation of nanoparticles has relied on EPR effect. This limits the versatility of nanoparticles in various ways. First, the size of the particles is limited to the size of fenestrations present in the tumor vasculature (380 – 780 nm) [57]. Most current nanovectors are approximately in this size range (100 – 300 nm) and hence have been shown to extravasate through the fenestrations and accumulate in the tumor mass [57]. Even this is not a constant feature as the size of the fenestrations depends on the stage and type of tumors [58]. To address these issues, the concept of multistage vectors (MSV) was developed [59]. MSV were designed as vasculature

targeting nanovectors (Stage 1 MicroParticles, S1MP) that can release smaller payloads (Stage 2 NanoParticles, S2NP) containing imaging/therapeutic agents. They were engineered to overcome biological barriers by decoupling the multiple functions typically required by nanovectors and distributing them onto multiple stages [21].

Most of the nanoparticles that are currently in the clinics or under investigation are synthesized using bottom-up fabrication or self-assembly technique and hence acquire an energetically favorable spherical shape. However, when in circulation, it has been shown that the size and shape of particles affect their trajectory as well as specific (ligand-receptor type) and non-specific (van der Waals, electrostatic and steric) interactions with the vessel wall [60]. The size of the particles dictates their interaction with the red blood cells in the circulation. Smaller nanoparticles (<500nm) stay in the middle of blood vessels because they "fit" in the pockets between RBCs, while larger particles (micron sized) get pushed to the "cell-free" zone of blood vessels by RBCs [54]. This process of "margination" has two main functions: (1) it facilitates the "drift" of particles from the center of the vessel to the vessel wall thereby (2) allowing higher probability of interaction of the particles with the endothelial cells to "identify and bind" to molecular targets [60]. Spherical particles require an external force, such as gravitational or magnetic, to induce a lateral shift/margination towards the vessel wall [61]. On the other hand, non-spherical particles, depending on their orientation in the circulation and the forces exerted by the blood on them, easily marginate without the requirement of additional forces. The velocity with which the particles marginate is directly proportional to their aspect ratio. Thus, spherical particles, with aspect ratio of 1 have the least propensity of marginating while discs (aspect ratio of infinity) have the highest chance and velocity of marginating to the vessel walls [60].

Another important aspect affected by the shape and size of the particles is their ability to adhere to the vessel wall, following margination. As mentioned before, the interaction with the vessel wall can be specific due to ligand-receptor interactions or non-specific, caused by various physical forces. In both cases, the stronger these interactions are, the more force will be required to dislodge the particles. Non-spherical particles, again, depending on their orientation on the vessel wall, can have higher surface area interacting – both specific and non-specific. This means, that the force required to dislodge the particle will be more than if a spherical particle of similar volumes were to interact with the surface [60].

1.3.2 S1MP

Based on the above, our group rationally designed non-spherical S1MP that are made of porous silicon S1MP. Porous silicon is a biocompatible and biodegradable [62; 63; 64] material that has been investigated increasingly for its application in drug delivery [62; 65; 66; 67]. S1MP is manufactured by a combination of photolithography and electrochemical etching in hydrofluoric acid. The etching offers tunable pore size and porosity rendering it suitable for drug loading and conjugation of multiple targeting ligands [68] (Figure 3).

Photolithographic patterning of silicon wafers enables production of particles with various geometries [69] (Figure 3), which are important for tuning their biodistribution and tumor accumulation [70; 71]. The S1MP have been rationally designed for overcoming various barriers en route to the tumor site. One of the major functions of S1MP is the effective interaction with the microvasculature and docking to the endothelial cells or fenestrations. Another task of the S1MP is to protect S2NP from degradation while in circulation following intravenous administration.

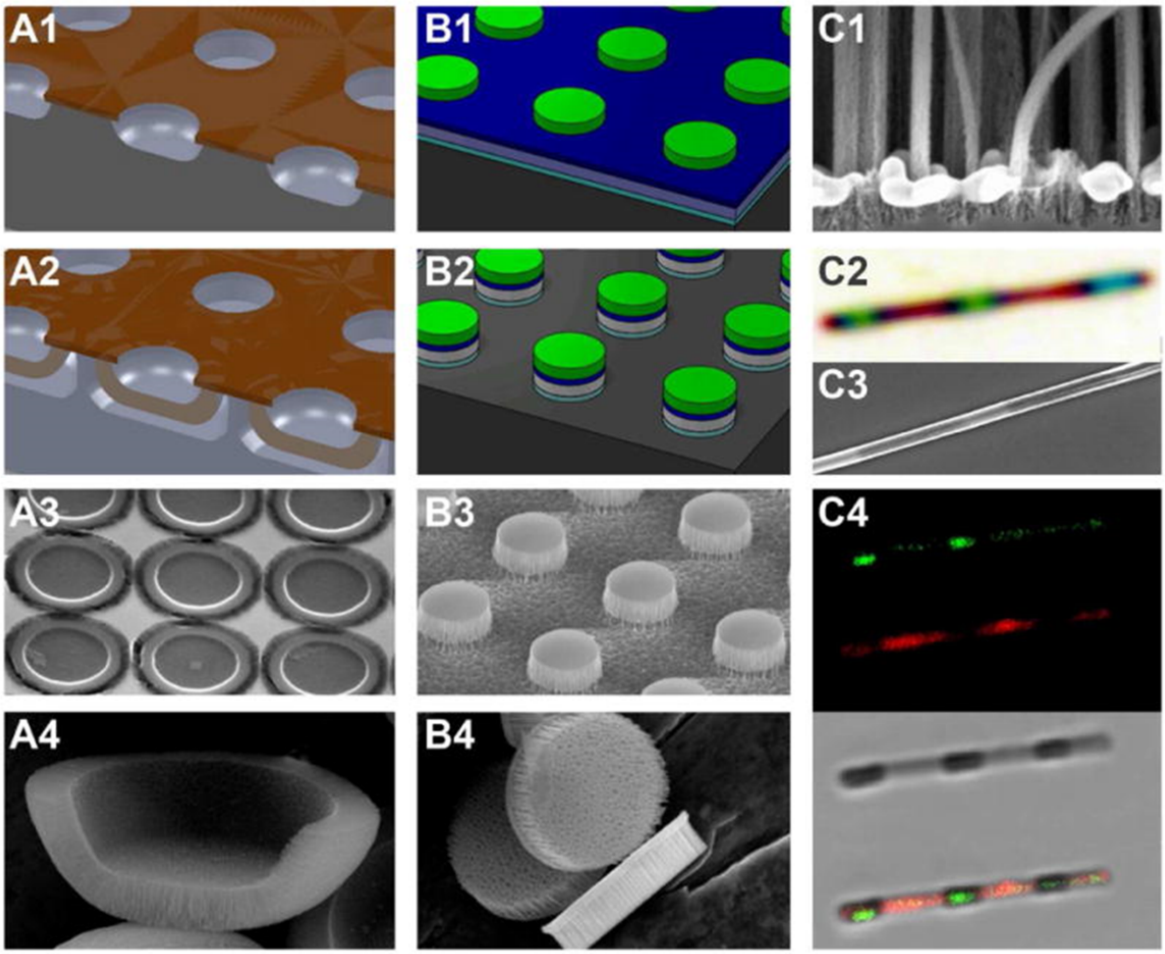

Figure 3: Tailoring geometry and porosity of S1MP. A1: Patterned SiN layer and trenches etched into silicon. A2: Electrochemically etched S1MPs with release layer. A3: S1MP array on wafer after removal of SiN. A4: Cross-section of hemispherical S1MP. B1: Photoresist pattern on LTO capped porous silicon film with release layer. B2: Particle array on wafer after RIE. B3: Discoidal S1MP array on wafer after LTO removal. B4: Released discoidal S1MPs. C1: Silver nanopattern etched into silicon forming porous silicon nanowires. C2: Nanowire barcode under white light. C3: SEM image of nanowire barcode. C4: 3-channel confocal microscopy images of nanowire barcode with green Q-dot loaded in small pore segment and red Q-dot in bigger pore segment. Reproduced with permission from [72]. Copyright 2014 American Chemical Society.

Further, S1MP can be surface modified with various entities including, polyethylene glycol (PEG) and other polymers [62], fluorescent probes [63], contrast agents, and biologically active tumor-microenvironment targeting moieties including antibodies [73], peptides [74], thioaptamers [75] and biomimetic membranes [76]. These studies demonstrate that active targeting of S1MP to molecules overexpressed in the tumor microenvironment is very efficient. For example, conjugation of E-Selectin targeted thioaptamer (ESTA) [75] or arginine-glycine-aspartate (RGD) peptide [74] to the surface of S1MP enabled 20% and 10% of injected dose (ID) accumulation in the tumor associated vasculature.

1.3.3 S2NP

Subsequent to accumulating in tumor associated vasculature, S1MP can release second stage nanoparticles (S2NP) that are encapsulated in their pores. Liposomes[77], quantum dots [59], SPION [78], polymeric micelles [79], gadolinium nanotubes [80] and hollow gold nanospheres [81] are some examples of S2NP that have been successfully loaded into S1MP. Figure 4 displays an overview of the different studies where S2NP were loaded into S1MP.

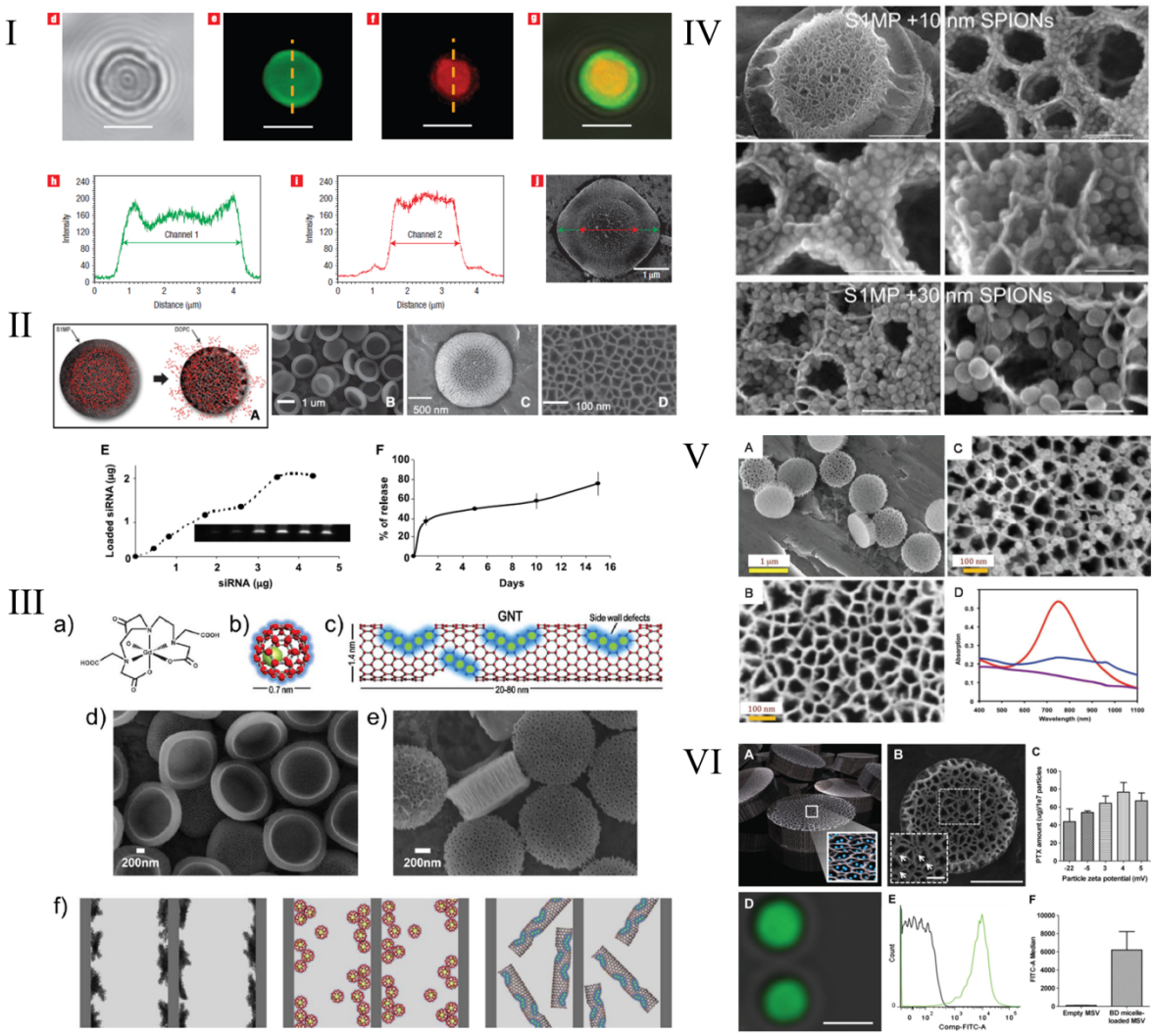

Figure 4: S2NP loading into S1MP. Various studies involving loading of different S2NP into the pores of S1MP are presented; (I) quantum dots [59], (II) liposomes [77], (III) gadolinium nanotubes[80], (IV) SPION [78], (V) hollow gold nanospheres [81] and polymeric micelles containing paclitaxel [79]. All figures are reproduced with permission from the respective journal.

1.3.4 Challenges in designing molecularly targeted MSV

As described in earlier sections, loading of S2NP into S1MP and conjugation of various targeting agents onto the surface of S1MP have been previously demonstrated independently. However, effective combination of the two processes poses several challenges. Chemical conjugation of targeting ligands on the surface of S1MP reduces the available surface area of pores available for the encapsulation of S2NP by as much as 75% [75] (Figure 5). Additionally, chemical conjugation of peptides, antibodies or thioaptamers to the surface of S1MP poses several technical challenges such as use of organic solvents for the conjugation, difficulty in the synthesis of the ligands, etc. all of which could adversely affect the receptor-ligand binding capability [82] and may damage delicate S2NP [83].

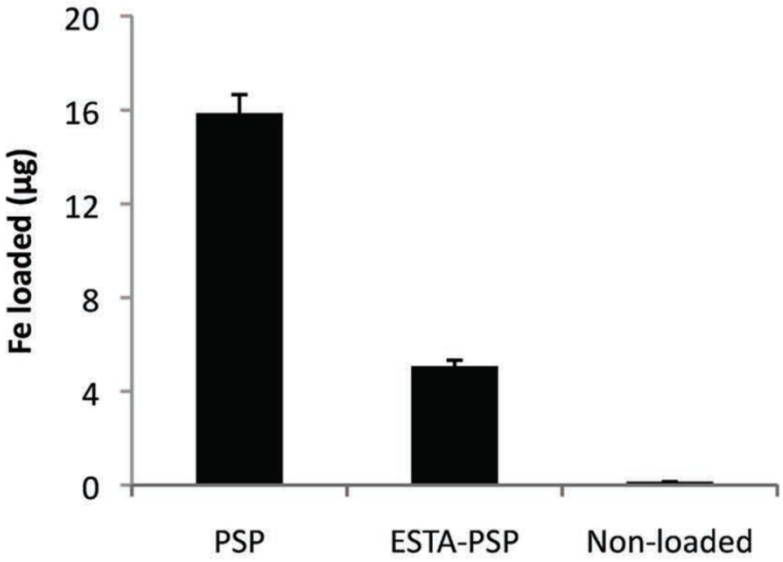

Figure 5: Loading of S1MP with SPION following conjugation with ESTA. Iron content in S1MP as measured by Inductively Coupled Plasma spectroscopy showing the decrease in the amount of iron loaded into the S1MP following conjugation of thioaptamers on the surface of S1MP. Reproduced with permission from [84].

To overcome these challenges while combining both targeting S1MP and loading of S2NP, we proposed a new technique that involves, first loading of the S1MP with S2NP followed by decoration of the surface of S1MP with tumor targeted bacteriophage by electrostatic interactions.

1.4 Targeting vascular zipcodes with bacteriophage

1.4.1 Filamentous bacteriophage and phage display

Bacteriophage are bacteria-specific virus which can be genetically modified to express a tumor-homing peptide on one of its 5 coat proteins, without compromising its infectivity [85]. This technique is called phage display [86]. The most commonly used phage for this purpose is the filamentous fd-tet bacteriophage. These are nanowire-like virus, measuring approximately 900nm in length and 7nm in width and having about 3900 copies of the major coat protein (pVIII) and 5 copies each of the minor coat proteins (pIII, pVI, pVII and pIX) (Figure 6). Bacteriophage expressing a tumor-targeting peptide on its coat proteins offers various advantages over monoclonal antibodies and conventional polymers such as; (i) non-toxicity, (ii) chemical and thermal stability, (iii) error-free and cost efficient mass production and (iv) mono-dispersity [87]. Using this technology, several tissue-specific surface receptor homing peptides have been identified. These peptides can be used to target therapeutic or imaging agents to the tumor cells. One of the main features of phage display is their ability to identify tissue-specific endothelial markers and the peptides that home to these endothelial cells. Various endothelial-specific markers have been identified in prostate cancer [88], *in vitro* HUVEC cultures [89], melanoma [90] and so on. Molecular signatures on vascular endothelium can also be used to target and enhance the accumulation of circulating nanovector at the tumor site [8]. Unlike tumor cells, these “vascular zip codes” seem to be

more stable and do not give into chemotherapeutic resistance [91]. Further, endothelial cell markers are the most accessible markers for any vascularly injected therapeutic agent, in comparison to markers expressed on tumor cells or stromal cells. Thus, these markers should be taken advantage of and used for homing therapeutic agents and nanoparticles to the tumor site.

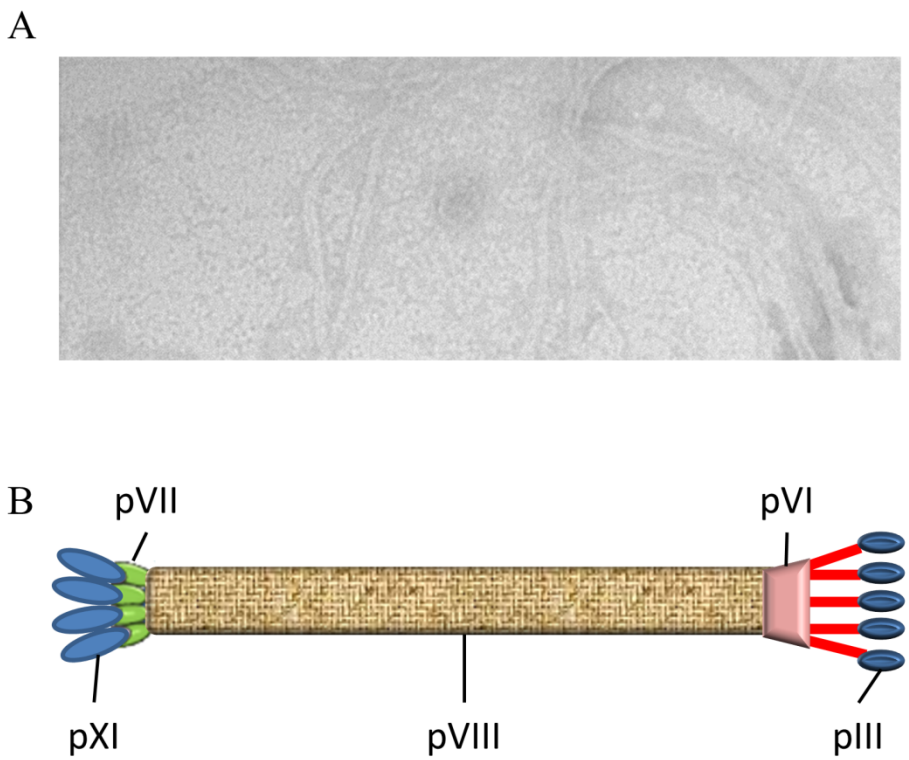

Figure 6: Bacteriophage structure and phage display. (A) TEM micrograph of filamentous bacteriophage; (B) Schematic presentation of bacteriophage with the 5 coat proteins.

1.4.2 Identification of targeting ligand – CRKL binding peptide

Recently Mintz et al. identified a new peptide sequence, YRCTLNSPFFWEDMTHECHA using phage display that showed marked tumor-homing in prostate cancer xenografts [92]. This peptide had sequence similarity with the plexin-semaphorin integrin (PSI) domain of β1 integrin. Unexpectedly, the peptide bound to the extracellular fraction of an intracellular adaptor protein, CRKL.

CRKL, a member of the Crk (CT10 Regulator of Kinase) protein family, was originally identified as an intracellular adaptor protein in primary leukemic neutrophils from patients with chronic myeloid leukemia (CML) [93]. The Crk group of proteins have been implicated in a wide variety of intracellular signaling pathways involving tumor cell migration, invasion and survival [94]. Tissue expression of CRKL has been observed in various solid tumors like gastric [95], lung [96; 97], prostate [92], hepatocellular carcinoma [98] and breast cancers [99; 100] as a novel prognostic marker. A recent study by Fathers et al. [99] established the role of Crk proteins in regulating aggressive basal breast cancers. In these studies, over-expression of CRKL was associated with high-grade and proliferative breast cancers with poor prognosis and decreased survival.

Proteins located in various intra and extracellular compartments can have multiple functions based on their location [101]. When found intracellularly, CRKL has been implicated in integrin mediated signaling by binding to various tyrosine phosphorylated scaffold proteins such as C3G, paxillin and p130Cas, thus affecting adhesion and migration. CRKL can also translocate to the nucleus and act as a nuclear adaptor protein for Stat5 regulating gene transcription through DNA binding [102]. While most of the studies on CRKL have shown that it acts as an intracellular adaptor protein in cytoplasmic or nuclear

compartments, a recent work by Mintz et al. demonstrated that the unphosphorylated form of the protein is secreted out either by ABC transporters or when the tumor cell dies and can be found in the extracellular compartment of tumor [92]. The proposed mechanism of action of secreted CRKL involves binding to the PSI domain of β1 integrin to activate MAP kinase pathway causing nuclear transcription and eventual cell migration and proliferation (Figure 7) [103]. Furthermore, a study with mutant cells lacking CRKL suggest an important role of CRKL in β1 integrin mediated cell adhesion to extracellular matrix [104].

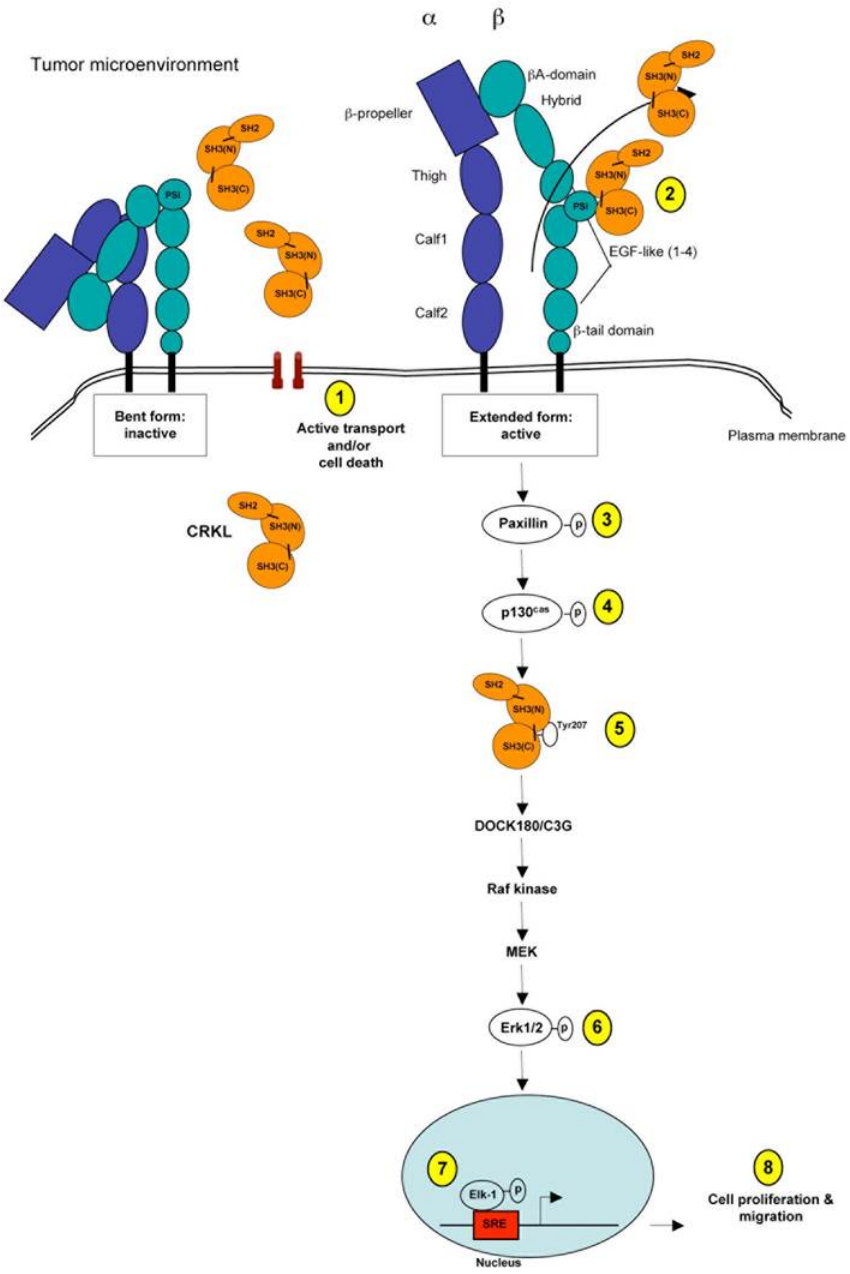

<u>Figure 7:</u> A working model based on the switchblade integrin activation. A hypothetical pathway used by extracellular (secreted and/or released) CRKL to activate the integrin-mediated MAPK cascade to promote cell proliferation and migration is shown. Reproduced with permission from [103].

Based on these, we hypothesized that the secreted CRKL from tumor cells would also bind to β1 integrins on endothelial cells of tumor associated vasculature and the CRKL targeting peptide can be used to target nanovectors to the endothelial cell surface bound CRKL.

1.4.3 AuNP-bacteriophage networks

Peptide displaying bacteriophage themselves has been used in the past for multiple biomedical applications such as biological sensing [105], stem cell differentiation [106] and therapeutic delivery [82; 85; 107]. The bacteriophage can be also be used as building blocks for bottom-up nanofabrication. Souza et al. demonstrated that these biocompatible and cell-targeting bacteriophage can spontaneously organize into dense networks when combined with gold nanoparticles (AuNP) [108], without the requirement for genetic modifications of the pVIII major coat proteins or chemical conjugation between the bacteriophage and AuNP (Figure 8). The AuNP-bacteriophage networks have unique optical properties that can function as signal reporters for fluorescence and dark-field microscopy as well as near infrared surface enhanced Raman scattering (NIR-SERS) spectroscopy [105]. The cell-targeting ability of bacteriophage was enhanced due to the presence of AuNP in *in vitro* melanoma cells. Au-bacteriophage networks were also detected in real-time by non-invasive NIR-SERS *in vivo* [109].

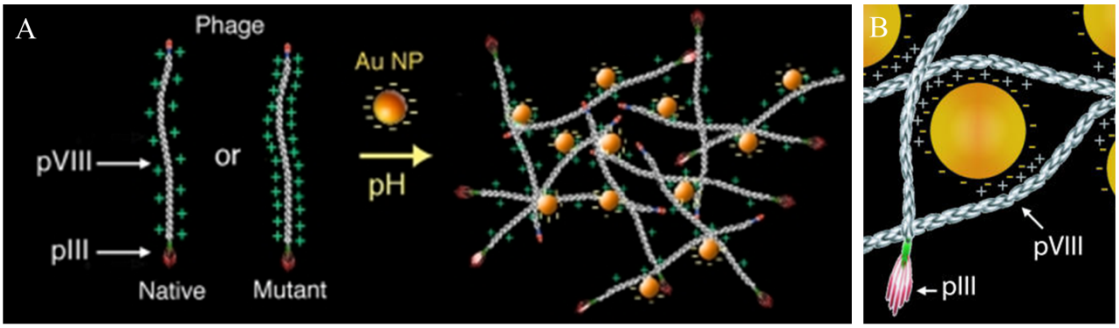

Figure 8: Schematic illustrating the electrostatic interaction of AuNP and bacteriophage. Adapted with permission from from [105; 108].

1.5 Hypothesis

The hypothesis of this work is that porous silicon S1MP can spontaneously form complexes with CRKL targeted Au-bacteriophage networks, to form Bacteriophage Associated Silicon Particles (BASP) while preserving the payload carrying potential and enhancing the tumor specific accumulation of the S1MP (Figure 9).

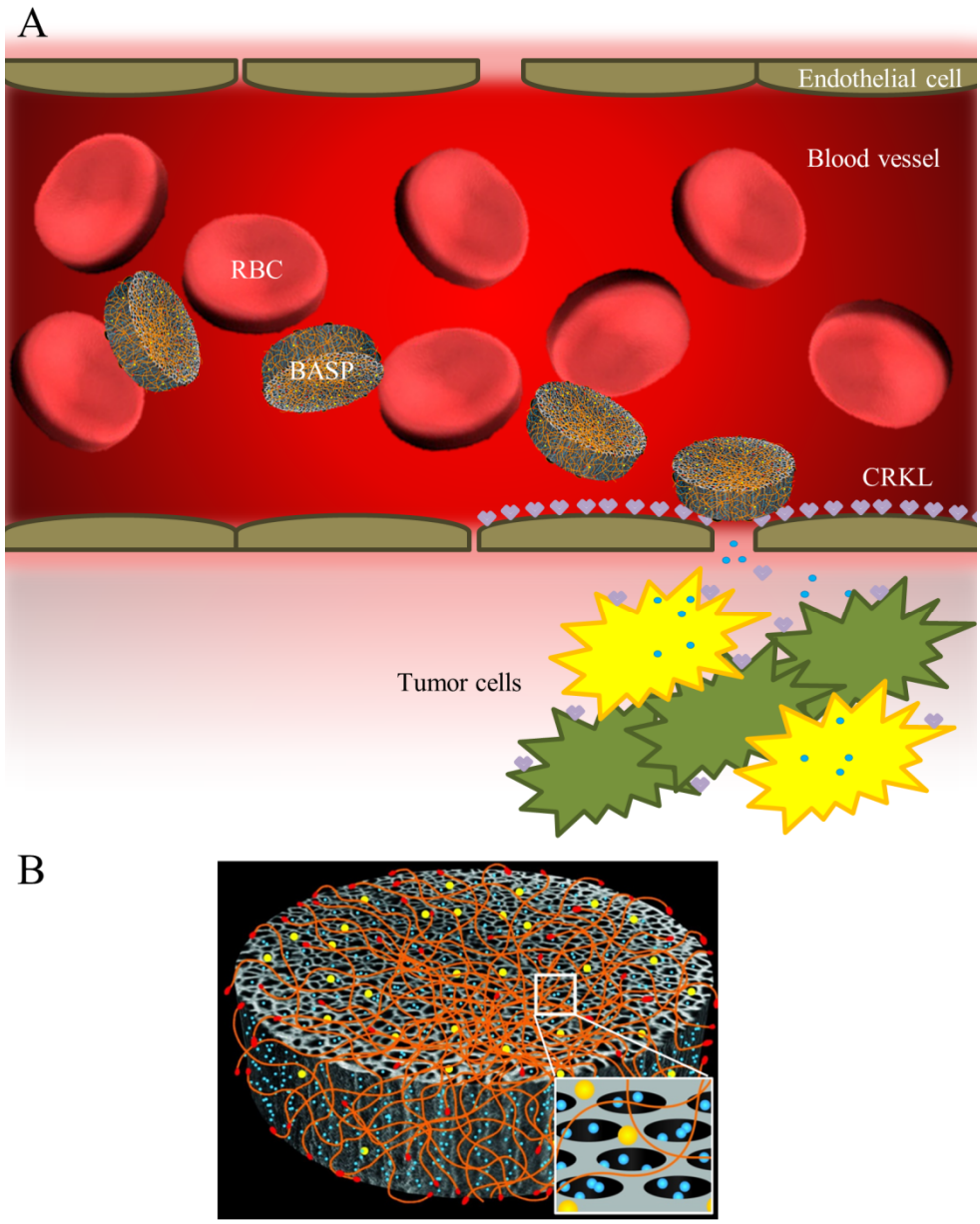

Figure 9: Schematic presentation of (A) Bacteriophage Associated Silicon particles (BASP) that exhibit enhanced ability to marginate within blood vessels and adhere to tumor associated endothelium. Once positioned at the tumor site, the BASP can release its therapeutic or imaging payload to achieve the desired effect prior to complete biodegradation of the carrier particle and (B) The assembly of BASP: Au-bacteriophage and non-spherical S1MP. Reproduced from [83] with permission from The Royal Society of Chemistry.

1.6 Significance

The aim of this study is to design multicomponent nanovectors capable of overcoming sequential biobarriers using specific and independent components at each stage and delivering substantial therapeutic agent to breast cancer tissue. The novelty of this project lies in the use of simple, electrostatic interactions for targeting MSV to tumor vasculature, while maintaining the superior payload carrying potential of the S1MP.

1.7 Objectives

The overall objective of this work was to develop a multifunctional drug delivery vector targeted to breast cancer tissues with good payload carrying potential. To achieve this, the following objectives were identified:

- To identify a suitable vascular biomarker that can be used to target MSV in breast cancer.
- To design and characterize BASP
- To evaluate payload carrying potential of BASP
- To evaluate *in vitro* and *in vivo* targeting ability of BASP
- To evaluate therapeutic efficiency of BASP

CHAPTER 2: MATERIALS AND METHODS

2.1 Identification and evaluation of CRKL expression in *in vitro*, *in vivo* and clinical samples

2.1.1 Cell culture

Human breast cancer cell lines MCF7, MDA-MB-231 and SUM159 were maintained in Dulbecco's Modified Eagles Medium (DMEM, Life Technologies™, NY, USA) supplemented with 10% fetal bovine serum (FBS, Life Technologies™, NY, USA) and 1% penicillin (100units/mL) and streptomycin (100µg/mL). Human breast epithelial cell line (MCF10A) was maintained in DMEM/F12 media (Life Technologies™, NY, USA) supplemented with 5% horse serum (Life Technologies™, NY, USA), 20ng/mL epidermal growth factor (EGF, PeproTech, NJ, USA), 500µg/mL hydrocortisone (Sigma-Aldrich Co., MO, USA), 100ng/mL cholera toxin (Sigma-Aldrich Co., MO, USA), 10µg/mL insulin (Sigma-Aldrich Co., MO, USA) and 1% penicillin and streptomycin.

Human umblical vein endothelial cells (HUVEC, Lonza Inc., USA) were maintained in Endothelial Basal Medium -2 (EBM-2) supplemented with EGM-2 Bulletkit (Lonza Inc. USA). Human microvascular endothelial cells (HMVEC, ATCC) were maintained in EBM-2 supplemented with EGM-MV bulletkit (Lonza).

2.1.2 Tumor models

Orthotopic mouse models of breast carcinoma were developed by inoculating $5x10^4$ EF43.*fgf4* cells into the mammary fat pad of 5 – 7 week old Balb/C mice as previously described [110]. The tumors were allowed to grow for 5 days and the mice were sacrificed to harvest the tumor for immunohistochemical and immunofluorescence staining. Patient derived tumor xenograft (2665A) and human cell line (MDA-MB-231) orthotopic xenograft sections were kindly provided by Dr. Bhuvanesh Dave. Human cell line (SUM159) xenograft sections and 4T1 cell line tumor sections were also collected for CRKL staining analysis. All animal procedures were approved by the Institutional Animal Care and Use Committee (IACUC) of Houston Methodist Research Institute.

2.1.3 Patient samples

Progressive breast cancer tissue microarrays were purchased from the Cancer Diagnosis Program (National Cancer Institute). A total of 94, formalin fixed and paraffin embedded, tumor tissue blocks corresponding to samples from different stages of disease progression classified using TNM (American Joint Committee on Cancer, VI edition) were studied. Twenty three specimens of normal breast tissue surgically removed with the cancerous tissue were used as controls. Patient related data including age, disease stage, tumor size, nodal involvement, metastatic status, estrogen and progesterone receptor status for the included specimens were provided. This study was approved by the Institutional Review Board (IRB) at the National Cancer Institute. Informed consent was not required for these samples.10x and 40x images were captured using a Nikon microscope and the intensity of staining was measured using NIS elements software.

2.1.4 Evaluation of surface bound CRKL by flow cytometry

Presence of CRKL on the surface of various cells was analyzed using CRKL antibody by flow cytometry analysis. Cells grown to 80% confluency in 6 well plates were harvested and incubated with CRKL antibody (Santa Cruz Biotechnology, TX, USA) for 45min followed by incubation with APC-labeled secondary antibody (Santa Cruz Biotechnology, TX, USA) for 1h. They were then washed and re-suspended in PBS for flow cytometric analysis. Cells incubated with the secondary antibody alone were used as controls. Cells were measured on a BD FACS Fortessa analyzer (BD Biosciences, CA, USA) using 561nm excitation laser. Twenty thousand cells were counted for each sample. Analyses of flow cytometric data focused only on live cells using electronic gate to identify the APC positive events using BD FACSDiva^{TM} software. All experiments were performed in triplicates.

2.1.5 Assessment of cellular localization of CRKL using immunofluorescence

The pattern of CRKL staining in cells was analyzed by immunofluorescence. Cells were seeded in 8 chamber slides (BD Bioscences, CA, USA) with 80% confluency and allowed to attach overnight. After fixation with 4% paraformaldehyde (PFA, Thermo Scientific, IL, USA), they were ramdomly divided into two groups. In one group the cells were permeabilized with 0.2% Triton^{TM} X-100 (Sigma-Aldrich Co., MO, USA) for 5 min and washed extensively. In the second group, the cells were not permeabilized, to specifically analyze the membranal fraction of CRKL. Both categories were incubated with CRKL antibody at 1:500 dilution for 1h at room temperature (RT), washed and incubated with Dylight 594-conjugated goat anti-rabbit secondary antibody (Thermo Scientific, IL, USA) for 45min. After the cells were washed, they were fixed again with 4% PFA, mounted with

DAPI containing Prolong gold (Life TechnologiesTM, NY, USA) and visualized under a Nikon fluorescence microscope (Nikon Instruments Inc., NY, USA).

2.1.6 Evaluation of CRKL expression in tumor using immunohistochemistry and immunofluorescence

Immunohistochemical staining was performed on paraffin-embedded tumor sections to study CRKL expression pattern. After two washes the slides were blocked for 10min in peroxidase followed by 2.5% horse serum (Life TechnologiesTM, NY, USA) for 10min; reacted with anti-CRKL antibody (1:100) for 30min; washed three times; incubated for 15min with horse anti-rabbit IgG; reacted for 4min with diaminobenzidine; rinsed; counter-stained with hematoxylin; mounted; and imaged. The intensity of staining was determined by image analysis using Nikon's imaging software – NIS elements.

Cryosections were fixed in cold acetone for 5min, air dried and subsequently blocked with 5% goat and horse serum in PBS for 30min at RT. Sections were then incubated with primary antibodies (CRKL antibody and anti-CD31 antibody) for 1h at RT or overnight at 4°C, washed and incubated for 1h with APC conjugated anti-rabbit antibody and FITC conjugated anti-mouse IgG. Tissue sections were washed, mounted and imaged using Nikon A1 confocal microscope or Nikon fluorescence microscope.

2.2 Nanovector design and fabrication

2.2.1 S1MP fabrication

"S1MP were fabricated by integration of photolithography and electrochemical etching of p-type silicon wafers in the Microelectronics Research Centre at The University of Texas at Austin, as previously described [59; 71]. Briefly, the dimensions of S1MP were defined by photolithography while the porous structure was formed by electrochemical

etching of silicon in a mixture of hydrofluoric acid (HF) and ethanol. Particles with different geometries and porosities were evaluated in this study including quasi-hemispherical and discoidal particles with mean pore sizes of 20–30nm or 50–60nm. Photolithography followed by electrochemical etching was used to make quasi-hemispherical S1MP [69]. For discoidal S1MP, electrochemical etching was performed before photolithography [9]. The current density was varied to obtain different pore sizes. Unmodified S1MP were retained on the substrate for washing steps, and then released by sonication in isopropyl alcohol (IPA). The particles were dried, and oxidized in a piranha solution (3:1 solution of sulfuric acid and 30% hydrogen peroxide) at 100-110ºC for 2h to yield S1MP with negative surface charge [S1MP(-)]. To produce S1MP with positive zeta potential [S1MP(+)], S1MP(-) were reacted with 2% 3-aminopropyltriethoxysilane (APTES, Sigma-Aldrich Co. LLC, USA) for 2h at 35°C. The modified particles were re-suspended and stored in IPA. Immediately before use, the particles were washed thrice and re-suspended in distilled water. The concentration (counts/mL) of S1MP was obtained using a Multisizer^{TM} 4 Coulter Counter (Beckman Coulter, USA). The zeta potential was measured with ZetaPALS (Brookhaven Instruments Corporation, USA).” [83]

2.2.2 AuNP synthesis

“Gold nanoparticles (AuNP) were prepared using the common Turkevich method [111] with a ratio of 1:0.8 of Gold(III) chloride and trisodium citrate (Sigma-Aldrich Co. LLC, USA) to yield ~45nm particles. The resulting AuNP colloid solution was concentrated by sequential centrifugation steps at 2600xg in Sorval Legend X1R Centrifuge (USA) for 10, 15 and 20min at 4°C to achieve an absorbance of approximately 5A.U. at 530nm. The

hydrodynamic radius and the zeta potential measurements of AuNP were performed using ZetaPALS." [83]

2.2.3 Bacteriophage isolation

"Bacteriophage particles were obtained as previously described [112]. Briefly, filamentous bacteriophage, both native (fd-tet) and YRCTLNSPFFWEDMTHECHA peptide-displaying (CRKL targeted), were grown by infection of K91 *Escherichia coli* (*E.coli*) bacteria overnight at 37°C and were subsequently isolated by PEG precipitation [82; 113]. The final pellet was resuspended in phosphate-buffered saline (PBS). Endotoxin free bacteriophage were obtained by phase separation using TritonX-114[114]. Bacteriophage titers or transducing units (TU) were determined by infecting *E.coli* and screening for tetracycline resistant colonies. Fluorescently labeled bacteriophage was used for identification by confocal microscopy when needed. The bacteriophage particles were conjugated with a 1000 fold excess of Dylight 594 (Thermo Fisher Scientific Inc., USA) for 1.5h and precipitated using PEG." [83]

2.3 Assembly of Bacteriophage Associated Silicon Particles (BASP)

"AuNP-bacteriophage networks were obtained based on the previously published method [105] with a bacteriophage input of 2.5×10^7 TU/μL. Two-fold serial dilutions of bacteriophage were done in distilled water and equal volumes of AuNP were added to each dilution and left undisturbed overnight at RT. The formation of AuNP-bacteriophage networks was noted by a change in colour of the solution from red to purple [105]. AuNP-bacteriophage networks were concentrated and incubated with S1MP for 1h with intermittent vortexing to form BASP." [83]

2.4 Characterization of BASP

2.4.1 Visualization of BASP formation

The morphology of the BASP was examined using various microscopic techniques.

2.4.1.1 Confocal microscopy

"For identification during confocal microscopy studies, S1MP(+) were loaded with fluorescein isothiocyanate conjugated bovine serum albumin (BSA-FITC, Sigma-Aldrich Co. LLC, USA). For this purpose 10^7 S1MP(+) were desiccated to remove any residual IPA. To the dry S1MP(+) 200µL of 5mg/mL aqueous solution of BSA-FITC was added and the system was incubated for 2h at 4ºC under rotation. The loaded particles were washed thrice in distilled water and incubated with Dylight 594 conjugated bacteriophage to form BASP and were visualized under a Leica DM6000 upright confocal microscope (Leica Microsystems, Germany) equipped with a 63X oil immersion objective." [83]

2.4.1.2 Transmission Electron Microscopy

"For transmission electron microscopy (TEM), samples were placed on 100 mesh coated copper grids treated with poly-l-lysine for 1h. Excess samples were blotted with filter paper and the BASP were stained with filtered aqueous 1% ammonium molybdate and 0.02% BSA, pH 7.0 for 1min. The samples were blotted, allowed to dry and imaged using the AMT Imaging System (Advanced Microscopy Techniques Corp., Danvers, MA) JEM 1010 TEM (JEOL, USA, Inc., Peabody, MA) at 80kV fitted with an AMT Advantage digital CCD camera system." [83]

2.4.1.3 Scanning Electron Microscopy

"BASP solutions were dried on cleaned SEM stubs overnight in a desiccator and sputter-coated with a 5nm layer of gold, using a Plasma Sciences CrC-150 Sputtering System

(Torr International, Inc.). Scanning electron microscopy (SEM) images were acquired under high vacuum, at 20kV, spot size 3 – 5, using an FEI Quanta 400 FEG ESEM (FEI™, USA) equipped with an ETD (SE) detector." [83]

2.4.2 Effect of porosity and zeta potential of S1MP on BASP formation

"To study the effect of surface charge and porosity of S1MP in the formation of BASP, we incubated the systems with various geometries, porosities and surface charges of S1MP. The geometries of S1MP varied from quasi-hemispherical to discoidal to cylindrical with size ranges between 0.4µm to 3µm. The pore sizes of S1MP used were either 20-30nm (huge pore, HP) or 40-60nm (giant pore, GP). The surface charge of the S1MP used was modified by oxidation to yield a negative zeta potential or by silanization to yield a positive charge as described earlier." [83]

2.4.3 Evaluation of contact angle

"The hydrophilicity of the systems was determined by measuring the contact angles made by the sample solution resting on a flat horizontal solid surface using captive bubble contact angle goniometry." [83]

2.4.4 Spectral characteristics of BASP

"Light spectroscopy was used to study the absorption characteristics of BASP during their formation. Shifts in the absorbance spectra of AuNP towards the NIR wavelengths were evaluated using SpectraMax M2 spectrophotometer (Molecular Devices, USA) or Biotek Synergy H4 hybrid multimode microplate reader (BioTek® Instruments, Inc., USA).

For SERS, BASP were excited by a fiber-optic probe delivering 785nm laser light for 10s. The resulting Raman scattering data (average of 3 results) were gathered on a PerkinElmer Raman Station 400F (PerkinElmer Inc., USA) after background subtraction

with water. The spectra were analyzed with Spectrum software (PerkinElmer Inc., USA)." [83]

2.4.5 Thermal effects of BASP

"The enhanced absorbance in the NIR region prompted the use of NIR laser to test the heating potential of BASP. 200µL of the sample solution was exposed to Delta 810nm diode laser (AngioDynamics UK Ltd.) with an output of 10J/cm^2 for 250msec at an interval of 100msec for a total of 10min using a 2mm fixed focus spot hand-piece. The resulting change in temperature was measured using an OxyLite^{TM} probe (Oxford optotronix Ltd., USA)." [83]

2.5 *In vitro* degradation of BASP

"BASP or S1MP (5x10^7, 1.6µm quasi-hemispherical) were suspended in 1mL of 100% FBS and incubated at 37°C with constant mixing in a rotary shaker for predetermined times. Aliquots (100µL) were taken at specified time intervals namely 0, 0.5, 1, 4, 8, 24 and 48h. For quantitative analysis of elemental silicon in the degradation medium, 90µL of the aliquots were filtered through a microcentrifuge filter to separate the non-degraded S1MP from the degradation products, diluted with water and analyzed using Varian 720-ES Inductively Coupled Plasma – Optical Emission Spectrometer (ICP-OES, Varian Inc., USA) set at 1kW, with plasma flow set to 15L/min, auxiliary flow of 1.5L/min and a nebulizer flow of 0.75L/min. Silicon contents in the degradation medium was detected at 250.69nm, 251.43nm, 251.61nm and 288.158nm using 1ppm of Yttrium as an internal control. The remaining 10µL were washed thrice with deionized water to remove salts and proteins and processed for SEM analysis as described above." [83]

2.6 Loading of S2NP

"S1MP ($1.5x10^8$, 1x0.4µm discoidal, 20-30nm pore size) and E-Selectin thioaptamer conjugated S1MP (ESTA-S1MP) were dried in a desiccator. For ESTA-S1MP, the S1MP were conjugated with a 10^7 fold excess of thioaptamers using PolyLink Protein Coupling kit for 1h as described earlier [75]. Amine modified SPION (15nm) suspended in PEG was centrifuged at 2000rpm for 5min at RT to remove aggregated particles. The supernatant was used as the stock for loading experiments. SPION solution (25µL) was added to S1MP and incubated for 30min with intermittent sonication. The SPION loaded S1MP were washed twice with water and then incubated with 15µL AuNP-bacteriophage networks for 1h to allow the assembly of BASP. The BASP were washed an additional time to remove any unbound SPION. NMR relaxation profiles of the SPION loaded particles were measured using a Bruker Minispec mq-60 bench-top relaxometer (Bruker Optics Inc., USA) operating at 60MHz and 37°C. The solutions were then digested for evaluation of elemental iron by heating them with nitric acid at 120°C thrice until the acid evaporated. The sediments were then resuspended in water. The iron content was detected at 238.204nm and 259.940nm using ICP-OES as previously described.

S1MP ($1.5x10^8$, 1x0.4µm discoidal, 20-30nm pore size) were loaded with 20µL of 2µM carboxylated quantum dots (QD) in a process similar to the SPION loading. Following BASP formation, the particles were visualized under fluorescence microscope to see if the QD are confined to the S1MP in the BASP or are released and entrapped in the AuNP-bacteriophage networks during the BASP formation. The samples were also digested using nitric acid and analysed for Cadmium content using ICP-OES." [83]

S1MP were loaded with Abraxane also using the wet incipient method. Abraxane was reconstituted at 1.5mg/20µL of distilled water and added to $1x10^9$ S1MP. After 1h of rotation at RT, the S1MP were either reconstituted in a total of 100µL water or AuNP-bacteriophage networks to form BASP.

2.7 *In vitro* studies

2.7.1 Evaluation of cellular association of BASP

To study the *in vitro* behavior of BASP, endothelial cell lines (HUVEC and HMVEC) and breast cancer cell line (MCF7) with the maximum amount of surface CRKL were incubated with BASP and observed. HUVEC and HMVEC were seeded at 200,000 cells/well in a 12 well plate (BD Falcon) and allowed to grow overnight at 37ºC. Cells were blocked with 30% FBS for 1h at 37ºC and were incubated with BSA-FITC (Sigma Aldrich) loaded S1MP, non-targeted BSA-FITC loaded fd-tet BASP or CRKL targeted BSA-FITC loaded BASP for upto 1h. The cells were subsequently washed, fixed with 4% PFA and resuspended in PBS for analysis by flow cytometry.

MCF7 cells seeded at 70% confluency on 8 chamber microscope slides (BD Falcon) and allowed to grow overnight at 37°C. Cells were blocked with 30% FBS for 1h at 37°C and were incubated with BSA-FITC (Sigma Aldrich) loaded S1MP, non-targeted BSA-FITC loaded fd-tet BASP or CRKL targeted BSA-FITC loaded BASP for 6h. The cells were subsequently washed and fixed with 4% PFA, permeabilized with 0.2% Triton X-100 and blocked with 1% BSA (SigmaAldrich) for 1h. The phage were stained with rabbit anti-phage primary antibody (Sigma Aldrich) followed by Dylight-594 tagged goat anti-rabbit secondary antibody. The cells were stained with nuclear stain, Draq 5 (Biostatus Ltd.), fixed and imaged using a Leica Confocal microscope.

MCF7 cells were plated in 24 well plates containing 5 x 5mm Silicon Chip Specimen Supports (Ted Pella, Inc., Redding, CA) at 70% confluency. Cells were incubated with S1MP, fd-tet BASP or CRKL targeted BASP (5 particles/cell) at 37ºC for 6h. Samples were washed with PBS and fixed in 2.5% glutaraldehyde (Sigma-Aldrich) for 30min and processed for SEM analysis as described previously [115]. Briefly, the cells were dehydrated in a step-wise manner in increasing concentrations of ethanol (30%, 50%, 70%, 90%, 95% and 100%) for 10min each. The cells were then incubated in 50% t-Butanol for 10min followed by incubation in 100% t-Butanol for 5min and overnight incubation in a dessicator. Specimens were then mounted onto SEM stubs (Ted Pella, Inc.) with conductive adhesive tape, sputter coated with 5nm layer of gold and imaged under high vacuum, at 20-30 kV, spot size 3.0-5.0, using a FEI Quanta 400 FEG ESEM equipped with an ETD (SE) detector.

MCF7 cells were grown to 70% confluency in a 24 well plate and incubated with S1MP, fd-tet BASP or CRKL targeted BASP (5 particles/cell) at 37ºC for 6h. Cells were washed and fixed in a solution of 2% PFA and 3% glutaraldehyde in PBS, pH 7.4 for 1h at RT. Samples were processed for TEM as described previously [115]. Briefly, the samples were washed with 0.1% cacodylate buffered tannic acid, fixed with 1% osmium tetroxide for 30min and stained with 1% uranyl acetate. The cells were then dehydrated in increasing concentrations of ethanol as described before, infiltrated, embedded in Poly-bed 812 medium and polymerized for 2 days at 60ºC. Ultra-thin sections were cut and stained with uranyl acetate and lead citrate. The samples were imaged in a JEM 1010 TEM microscope as described above.

2.7.2 Evaluation of interaction with endothelial cells under shear stress

HUVEC or HMVEC cells were seeded at $1.5x10^7$ cells/mL density on fibronectin coated Bioflux microfluidic 48 well plates (0-20 dynes/cm^2) and allowed to grow overnight. To activate endothelial cells, cells were seeded and allowed to attach for 1h. They were then incubated with conditioned media from EF43.*fgf4* cells overnight. Cells were then treated at 37ºC with one of the following: Alexafluor 555 conjugated S1MP, fd-tet BASP or CRKL targeted BASP under constant linear flow at either $10s^{-1}$ or $100s^{-1}$ shear rates at a concentration of 10^7 particles/mL. Briefly, APTES modified particles ($1x10^9$) were incubated with 0.5mg/mL solution of Alexa fluor 555 (Life Technologies™, NY, USA) for 1h at RT. The particles were then washed to remove unbound dye and again APTES modified before BASP formation. The flow of the particles over the cells was recorded by taking timelapse images in the TRITC channel at 12 frames per second for 1h using a 20X objective on an inverted Nikon microscope. The particles were removed and replaced with fresh media and the cells were monitored for an additional 16h with images being taken every 1h. The velocity of particles rolling on the cell surface and the number of particles attached were analyzed using NIS elements software equipped with 2D tracking component.

2.8 *In vivo* studies

2.8.1 Evaluation of targeting efficiency of CRKL targeted BASP

Breast cancer allografts were grown in immunocompetent Balb/c mice by injecting $5x10^4$ EF43.*fgf4* cells orthotopically in the mammary fat pad. After 10 -14 days, the mice were randomly divided into 4 groups and administered intravenously with one of the following: PBS, S1MP, fd-tet BASP or CRKL targeted BASP formed with $5x10^8$ S1MP (1.6µm quasi-hemispherical). The bacteriophage used in these experiments were either

labeled with Dylight 594 or unlabeled. Four hours following the administration of the systems, the animals were sacrificed and the liver and tumor were collected for histological analysis (conventional and hyperspectral microscopy). Paraffin embedded tissue sections were stained for bacteriophage by incubating with anti-bacteriophage antibody (Sigma Aldrich Co. LLC., USA) at 1:750 dilution for 30min. Frozen tissue sections from mice injected with Dylight 594 labeled bacteriophage containing BASP were counterstained for nucleus with Draq5 (Biostatus Limited, UK). Non-stained paraffin embedded tissue sections were fixed with 4% PFA, mounted with Prolong gold mounting media (Invitrogen, USA) and imaged using a darkfield condenser from CytoViva attached to an Olympus BX41 microscope and DAGE camera/software (CytoViva, Auburn, AL 36830) hyper-spectral imaging system that can identify material at resolutions of less than 100nm based on the material's unique spectral signatures.

2.8.2 Evaluation of therapeutic efficacy of CRKL targeted BASP

Abraxane was purchased from MD Anderson Cancer Center (Houston, TX) pharmacy and diluted in water before use. To assess the therapeutic activity of S1MP or CRKL targeted BASP loaded with Abraxane, Balb/C mice bearing orthotopic EF43.*fgf4* tumors on either side of their body were randomly divided into 4 groups (5 mice/group) and treated with: (i) PBS, (ii) Abraxane (Abx) (75mg/kg), (iii) S1MP-Abx (75mg/kg) or (iv) CRKL targeted BASP-Abx (75mg/kg). The mice were treated every third day and the tumor size was monitored every other day using calipers until the 11^{th} day

2.8.3 Intravital microscopy for studying particle flow characteristics

Orthotopic breast tumor bearing mice were randomly selected for intravital microscopy studies on days 5 and 10. The anaesthetized mice were surgically opened to

expose the tumor mass, positioned on a heated stage and injected with $5x10^8$/100µL particles of either Alexa Fluor 555 labeled S1MP or fd-tet BASP or CRKL targeted BASP. Immediately following injection, three channel images were acquired as a time lapse video at 30 frames per second using a 40x0.6 NA objective. Animals were imaged for 1h and then sacrificed as described above, to collect organs for histological analysis.

2.9 Evaluation of CRKL as a soluble biomarker

2.9.1 Collection of conditioned media (CM) for evaluation of secreted CRKL

Conditioned media (CM) were collected from SUM159 and MCF10A cell lines. The cells were seeded at 50% confluency overnight, washed with PBS and incubated with serum free media for 24h. The media was then collected, centrifuged at 5000rpm for 10min and the supernatant was stored at -80°C until analysis by ELISA.

2.9.2 Evaluation of secreted serum fraction of CRKL in *in vivo* models

Blood from nude mice grafted with patient derived breast tumors (2665A) were collected for enzyme linked immunosorbant assay (ELISA). All animal procedures were approved by the Institutional Animal Care and Use Committee (IACUC) of Houston Methodist Research Institute.

2.9.3 Collection of patient serum samples

Twenty nine breast cancer patients' sera and 9 healthy donor serum samples were purchased from Promeddx, LLC (Massachusetts) and tested for soluble CRKL fraction by ELISA. As in the tissue microarrays, the serum samples were from patients with different stages of disease progression classified using TNM staging. Twenty five out of the twenty nine patients were undergoing treatment. This study was approved by the IRB at Promeddx

LLC. Informed consent was obtained or implied by return of questionnaires at the physician's site.

2.9.4 Evaluation of soluble fraction of CRKL by Enzyme Linked Immunosorbant Assay

The levels of secreted CRKL in cell culture supernatants, serum samples from mice bearing 2665A breast tumors and breast cancer patients sera were analyzed using commercially available ELISA kits (Cloud-Clone Corp., TX, USA) according to manufacturer's instructions. The CRKL concentrations are expressed as pg/mL of blood plasma. Detection limit was 53pg/mL.

CHAPTER 3: RESULTS

3.1 CRKL as a cell surface biomarker

3.1.1 Localization on cell surface

A previous study has shown that CRKL, originally an intracellular protein is secreted by tumor cells into the tumor microenvironment [92]. We speculated that "the secreted CRKL from tumor cell lines would bind to the surface of cells through interaction with β1 integrin. To evaluate the membrane bound fraction of secreted CRKL, non-permeabilized breast cancer cells were analyzed by flow cytometry. The percentage of cells with surface-bound CRKL varied among different cell lines. Cancer cell lines (MCF7, MDA-MB-231 and SUM 159) showed 3 – 5 fold higher percentage of staining than mammary epithelial cell line (MCF10A). For instance 93.7% of MCF7 cells have surface bound CRKL when compared to 55.6% on SUM159 cells and only 17% on MCF10A cells (Figure 10A)." Murine breast cancer cell lines EF43.*fgf4* and 4T1 also showed very high staining for CRKL – upto 80%.

We also looked at the surface localization of CRKL in endothelial cells. The surface fraction of CRKL in endothelial cells can serve as an indicator of the fraction released from cancer cells. Moreover, since β1 integrin is overexpressed on angiogenic vasculature, we hypothesized that higher fractions of CRKL will be bound to the surface of tumor associated endothelial cells. The levels of surface bound CRKL were 82.2±4.7%, 25.9±12.7% and 13.7±1.1% for SVEC, HUVEC and HMVEC respectively (Figure 10B). Addition of cancer cell conditioned media (EF43.*fgf4* – CM) to HMVEC increased the surface localization of CRKL on HMVEC by about 2 fold (Figure 10C).

Immunofluorescence staining of the various cell lines confirmed the presence of CRKL on the cell surface. The lack of co-localization of nuclear (DAPI) and CRKL staining in non-permeabilized cells confirmed that the observed staining is the surface-bound fraction of CRKL. On the other hand, permeabilization of the cells led to the staining of the cytoplasm and the nuclear region showing that, as expected, a large fraction of the protein is present in intracellular compartments (Figure 10D).

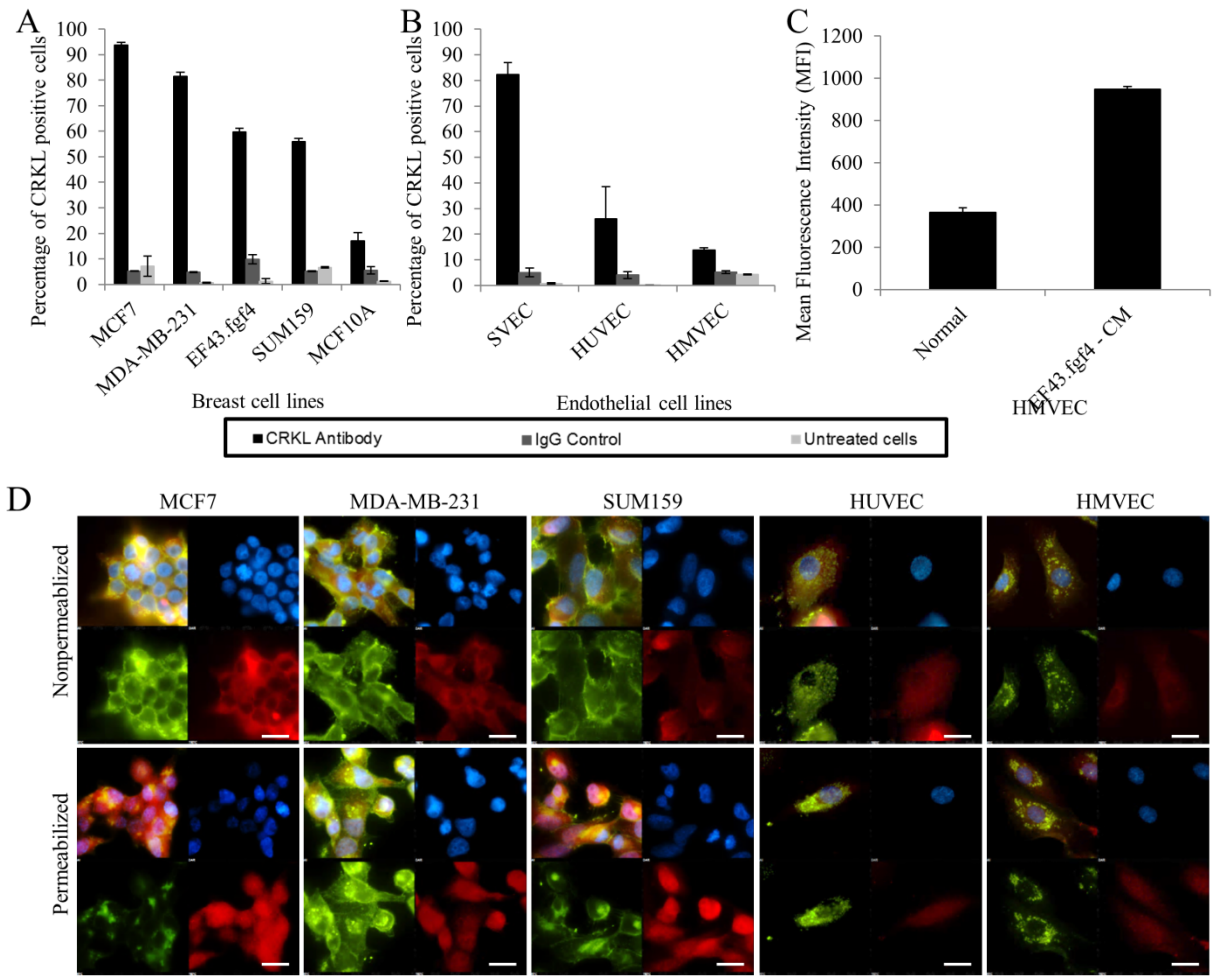

<u>Figure 10:</u> Surface localization of CRKL in breast cancer cells *in vitro*. Flow cytometry on non-permeabilized cells showing surface fraction of CRKL in (A) breast cancer and epithelial cell lines; (B) endothelial cell lines and (C) HMVEC incubated with cancer conditioned media. (D) Immunofluorescence images of human breast cancer and endothelial cells showing the difference in the staining pattern of CRKL (red) in permeabilized (bottom row) and non-permeabilized (top row) cells. The cells are counterstained with wheat germ agglutinin 488 for the cell membrane (green) and DAPI for the nucleus (blue). (Scale bar = 20µm)

3.1.2 Expression in *in vivo* and clinical tumor biopsies

Next, we "evaluated the patterns of CRKL expression in *in vivo* breast tumor models originated from a human clinical specimen (2665A) and human breast tumor cell lines MDA-MB-231 and SUM159. MDA-MB-231 xenografts exhibited cytoplasmic/membranal staining for CRKL, while SUM159 and patient derived xenograft 2665A showed stronger nuclear staining with mild cytoplasmic and extracellular staining." Murine breast tumor models from EF43.*fgf4* and 4T1 exhibited mainly extracellular CRKL staining (Figure 11A).

To evaluate the CRKL expression in human breast cancer specimens, we immunostained paraffin embedded cancer progression tissue microarrays with a total of 94 tumor cores (Figure 11B). It was noted that normal breast tissue stained positive for CRKL only in the ductal epithelium, therefore, during the pathological examination of the tumor tissue, the regions of ductal epithelium were excluded. More than 90% of the patients were Caucasians. Twenty seven patients were estrogen receptor (ER) negative and 46 were progesterone receptor (PR) negative. The average tumor size of the entire set of patients was 2.6 cm (range from 1 to 6.5 cm).

Similar to *in vivo* studies, the staining pattern in tumor tissue varied from nuclear to cytoplasmic to microenvironmental. Overall, about 85% of the breast cancer clinical samples stained positive for CRKL. The average intensity of CRKL (A.U./pixel), as measured by image analysis, was about 12 fold higher in breast tumor biopsies than in the uninvolved breast tissue (46.8±22.1 vs 3.9±1.9 A.U./pixel, respectively, Figure 11C). Table 3 summarizes the correlation of CRKL staining and the clinicopathological factors.

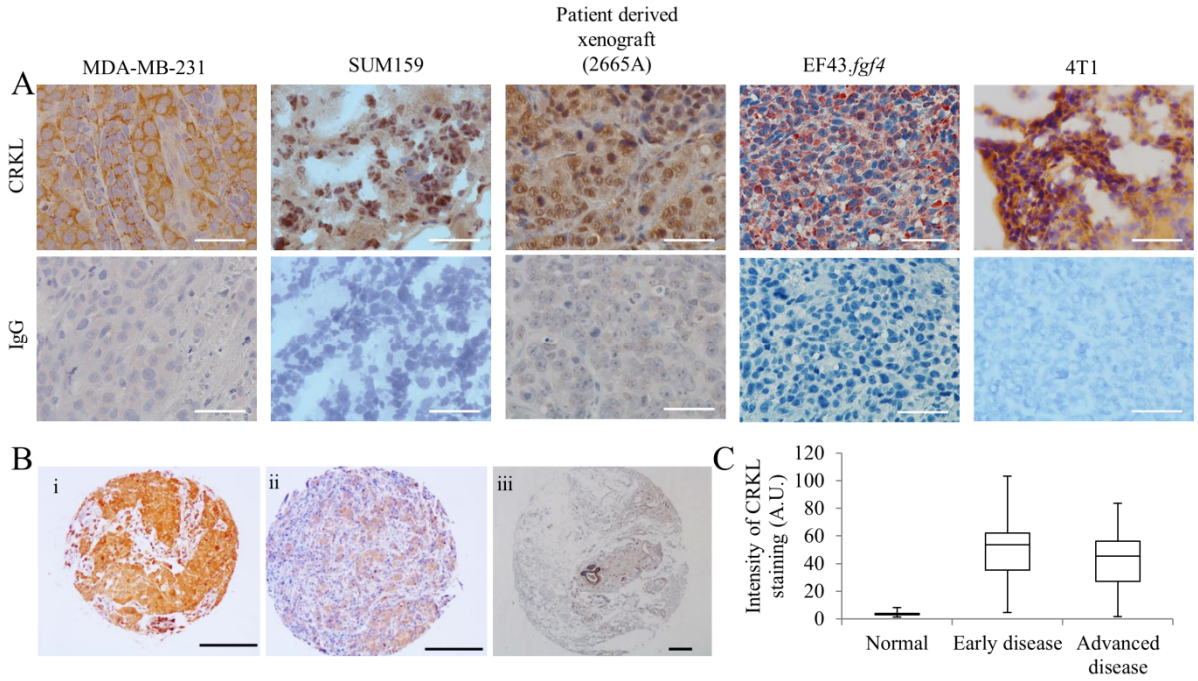

Figure 11: CRKL expression in *in vivo* samples and clinical tumor biopsies. (A) Immunohistochemistry for CRKL in (A) primary breast cancer xenografts (Scale bar = 50µm); (B) Immunohistochemistry of human breast cancer tissue microarray showing (i) strong and (ii) weak staining of invasive ductal carcinoma tissues, (iii) normal breast tissue showing positive staining mainly in the ductal epithelium. (Scale bar = 100µm) (C) Quantitation of intensity of staining through image analysis in tumor cores (early and advanced disease) and normal breast tissues.

To confirm our findings regarding surface fraction of CRKL on endothelial cells from in vitro studies, we tested co-localization of CRKL and endothelial marker (CD31 for breast cancer allografts and CD34 for human tissue microarray) staining in histological tumor sections. A stronger CRKL staining on tumor associated endothelial cells as compared to the overall tumor mass staining was observed in both the animal model (Figure 12A) as well as the tissue microarray (Figure 12B,C,D).

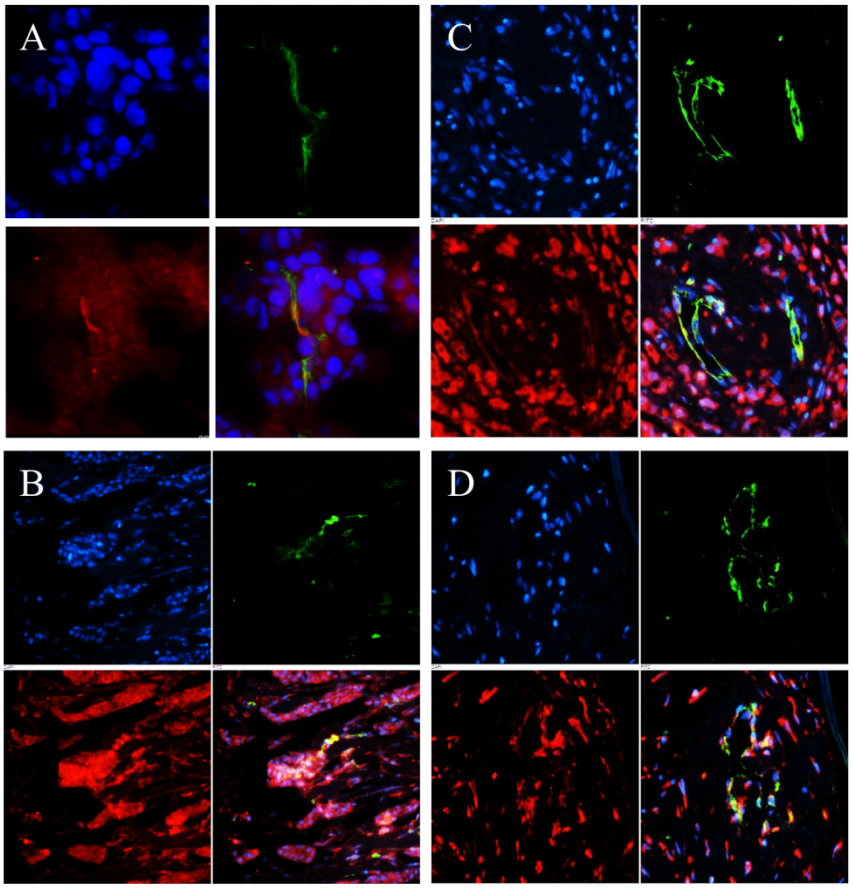

<u>Figure 12:</u> Co-localization of CRKL and tumor associated vasculature. Immunofluorescence staining of CRKL and (A) CD31 in EF43.*fgf4* breast allograft model; (B,C,D) CD34 in human breast cancer tissue microarray biopsies, showing co-localization of CRKL and vascular endothelial cells in the tumor.

Parameters	Staining intensity of CRKL in breast cancer tissue microarray				
	Negative		Positive		
	Number	%	Number	%	P
Age					
<60 years	10	19.6	41	80.4	0.86
>60 years	9	20.9	34	79.1	
T stage					
T1	7	16.2	36	83.8	0.001
T2	8	20	32	80	
T3	1	33.3	2	66.7	
T4	3	37.5	5	62.5	
Nodal involvement					
Negative	3	9	30	91	0.007
Positive	11	24.4	34	75.6	
Metastatic involvement					
Negative	10	16.4	51	83.6	0.08
Positive	9	27.3	24	72.7	
Tumor size					
< 2 cm	7	15.9	37	84.1	0.22
> 2 cm	12	24	38	76	
Estrogen receptor					
Negative	4	14.8	23	85.2	0.27
Positive	15	22.4	52	77.6	
Progesteron receptor					
Negative	7	15.2	39	84.8	0.11
Positive	12	25	36	75	

Table 3: Relationship between CRKL expression and clinicalpathological parameters

Based on the above observations, we decided to see if the extracellular fraction of CRKL could serve as a target for targeted drug delivery of nanovectors.

3.2 Physical characterization of BASP

3.2.1 Assembly of BASP

"BASP are comprised of three components: S1MP, AuNP and bacteriophage. The addition of AuNP to bacteriophage causes instantaneous agglomeration of AuNP noted by the color change from red to purple [105] and the condensation of the system into fibrous

structures as seen in Figure 13A, similar to what was previously reported by Souza et al.[105] Addition of these condensed AuNP-bacteriophage networks to S1MP resulted in spontaneous association between the components forming BASP. To verify the formation of BASP we used confocal microscopy and TEM. Fluorescently labeled bacteriophage used in the assembly of BASP clearly showed co-localization of the bacteriophage (red) and the BSA-FITC loaded S1MP (green) (Figure 13B). Further, TEM micrographs showed the close association of fibrous bacteriophage (white lines) and AuNP (black dots) with S1MP (a large porous structure) (Figure 13C)." [83]

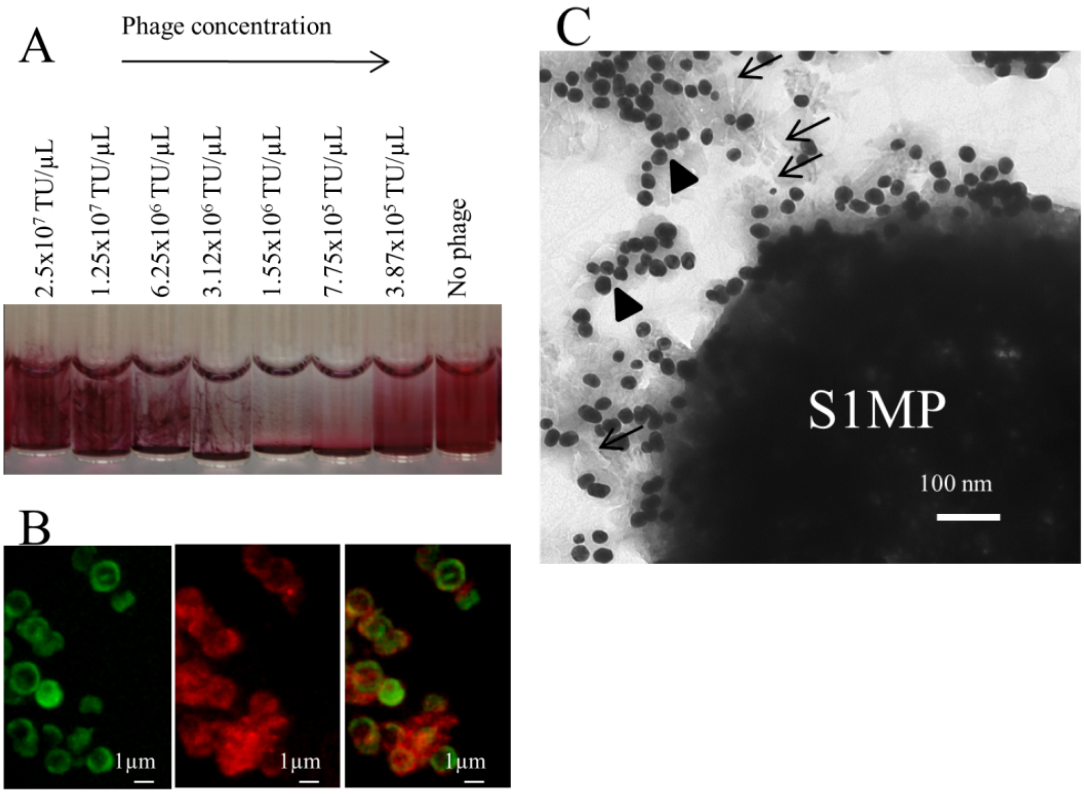

Figure 13: Visualization of the BASP formation. (A) Macroscopic view on network/gel formation corresponding to the association of AuNP-bacteriophage networks with S1MP to form BASP at serial dilutions of the bacteriophage starting from the concentration of 3.87x105 TU/µL ; (B) Confocal microscopic image of BASP with BSA-FITC loaded S1MP(+) (Green) and Dylight594 labeled phage (Red) showing the specific co-localization of the two; (C) TEM image of BASP showing the S1MP surrounded by AuNP(arrow heads) and bacteriophage(arrows). Reproduced from [83] with permission from The Royal Society of Chemistry.

"Optimization processes in the assembly of BASP involved incubation of various concentrations of the components in a systematic manner. It was seen that the concentration of AuNP (OD 1 to 7) did not affect the formation of BASP, while excessively high concentrations of silica beads (>10^6/µL) prevented their formation (Figure 14A). Also, it was found that formation of BASP was most efficient when assembled in a two-step process involving: (1) the formation of dense AuNP-bacteriophage networks; followed by the (2) coating of S1MP by these networks (Figure 14B)." [83]

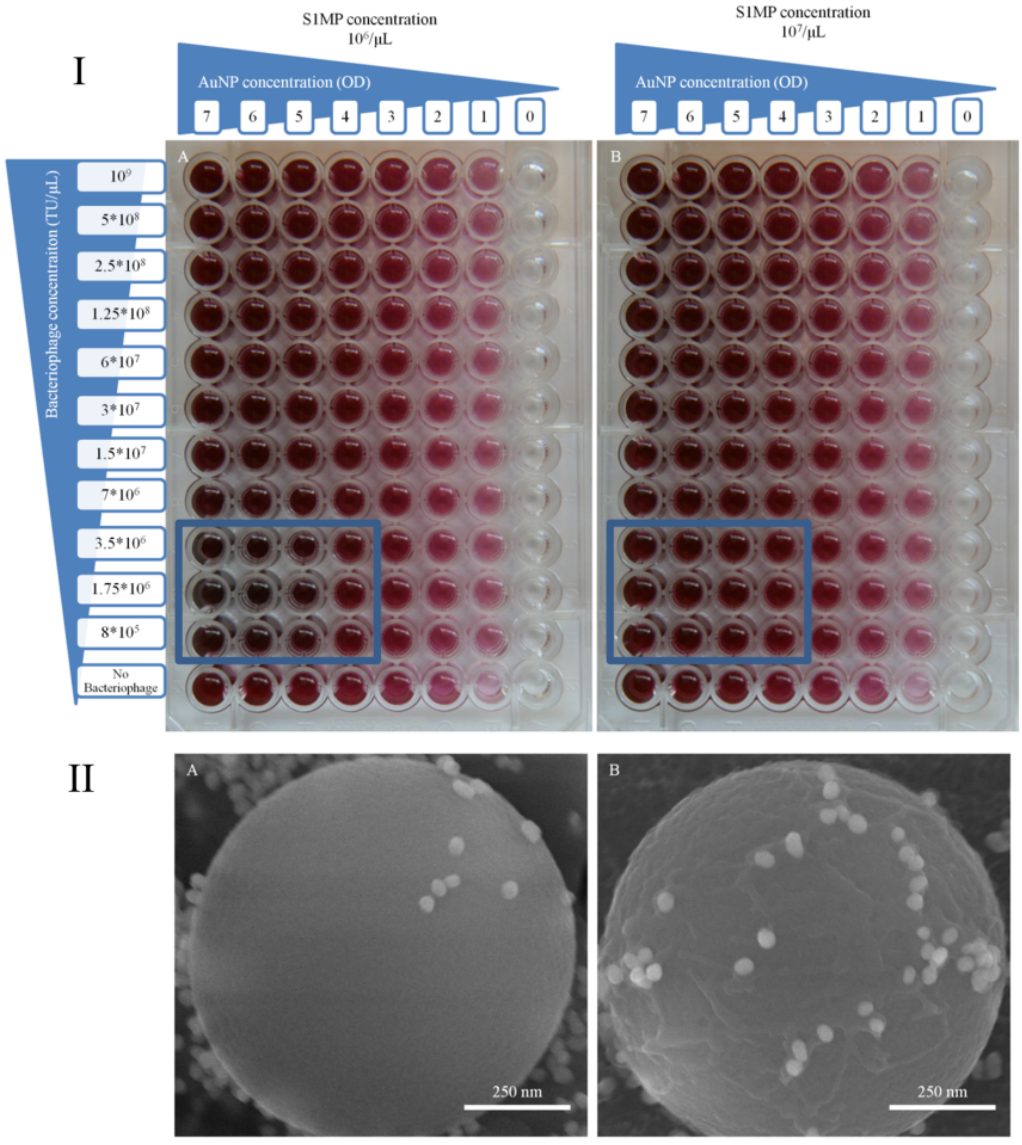

Figure 14: Effect of concentration and order of incubation on the formation of BASP (A) Photographs showing the assembly of BASP with different concentrations of the components. The red color is due to the presence of AuNP. Note the condensation and the color change in the solution (highlighted in the blue box) at bacteriophage concentrations of $3.5x10^6$, $1.75x10^6$ and $8x10^5$ TU/μL in A as opposed to the absence of such changes in B. (B) SEM micrographs of BASP with silica beads. Left: BASP formation when bacteriophage was added to a mixture of silica beads and AuNP. Right: BASP formation when AuNP-bacteriophage networks were added to silica beads. Note the significant increase in the number of AuNP (white dots) and the presence of fibrous coating on the silica beads (bacteriophage) in B. Adapted and reproduced from [83] with permission from The Royal Society of Chemistry.

3.2.2 Effect of porosity and zeta potential of S1MP on BASP formation

"We compared non-porous spherical silica beads to quasi-hemispherical and discoidal mesoporous silicon particles with different pore sizes in their ability to form BASP. Although the shape of S1MP used did not have much effect on the self-assembly of BASP, the association of AuNP to porous particles was evidently better than their association to non-porous silica beads (Figure 15)." [83]

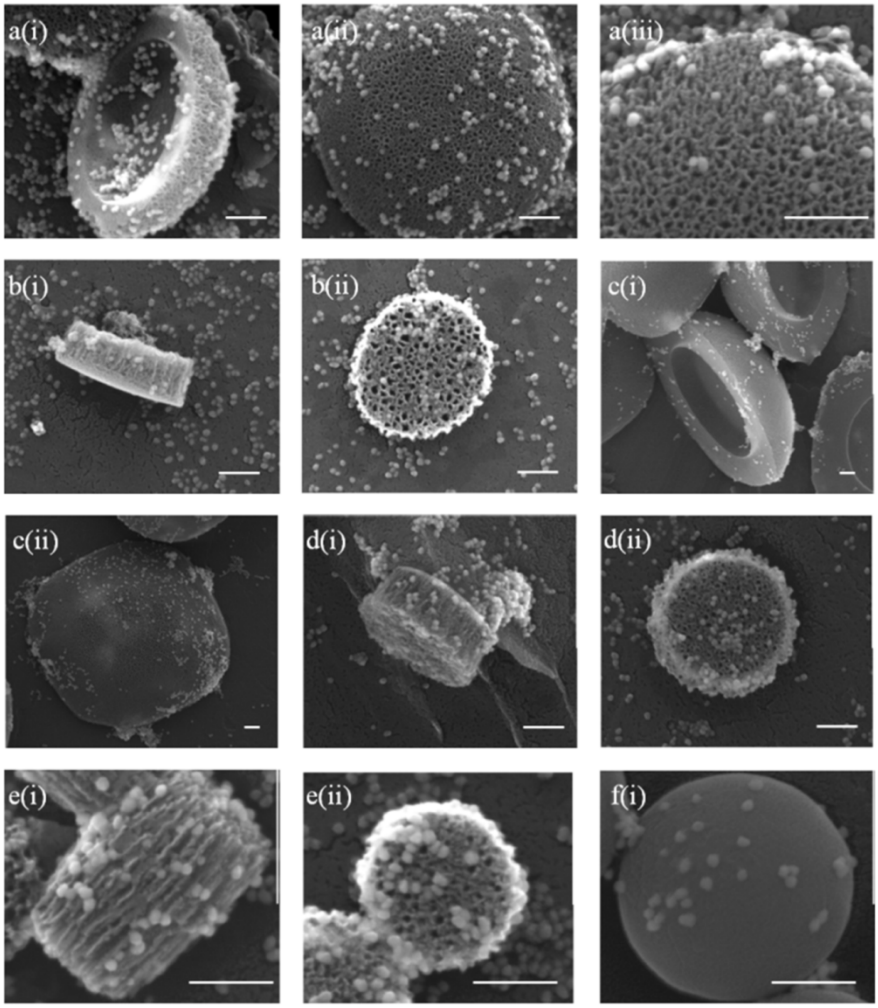

Figure 15: BASP design- effect of S1MP geometry and porosity. (A) SEM images of BASP formed in the presence of S1MP(-) with different geometries and porosities. The images show the association of S1MP with AuNP. The systems are as follows: (a) 1.6µm in diameter quasi-hemispherical HP (b) 1µm in diameter and 0.4µm in height discoidal GP (c) 3.2µm in diameter quasi-hemispherical HP (d) 1µm in diameter and 0.4µm in height discoidal HP (e) 0.6µm in diameter and 0.4µm in height discoidal HP (f) 1µm in diameter spherical solid silica beads. GP – pore size 40 – 60nm, HP – pore size 20 – 30nm, Scale bar - 300µm. Reproduced from [83] with permission from The Royal Society of Chemistry.

"The surface potential of drug delivery vehicles is another important feature to be considered in their design. The effect of zeta potential of S1MP on the formation of BASP was evaluated by comparing BASP containing 1.6μm quasi-hemispherical S1MP(+) and S1MP(-). The initial and final zeta potential values of the systems are presented in Figure 16 For S1MP(+) and S1MP(-), the initial zeta potential values were 8.9 ± 1.9mV and -25.7 ± 1.3mV respectively. The AuNP-bacteriophage networks have a net negative charge. After the formation of BASP, both systems yielded similar negative zeta potentials meaning that the significant shift in zeta potential values occurred only during the formation of BASP containing S1MP(+). Morphological examination of the resulting systems by SEM confirmed this behavior. In agreement with the zeta potential data, SEM micrographs show more efficient association of AuNP-bacteriophage networks with S1MP(+) particles (Figure 16 inset)." [83]

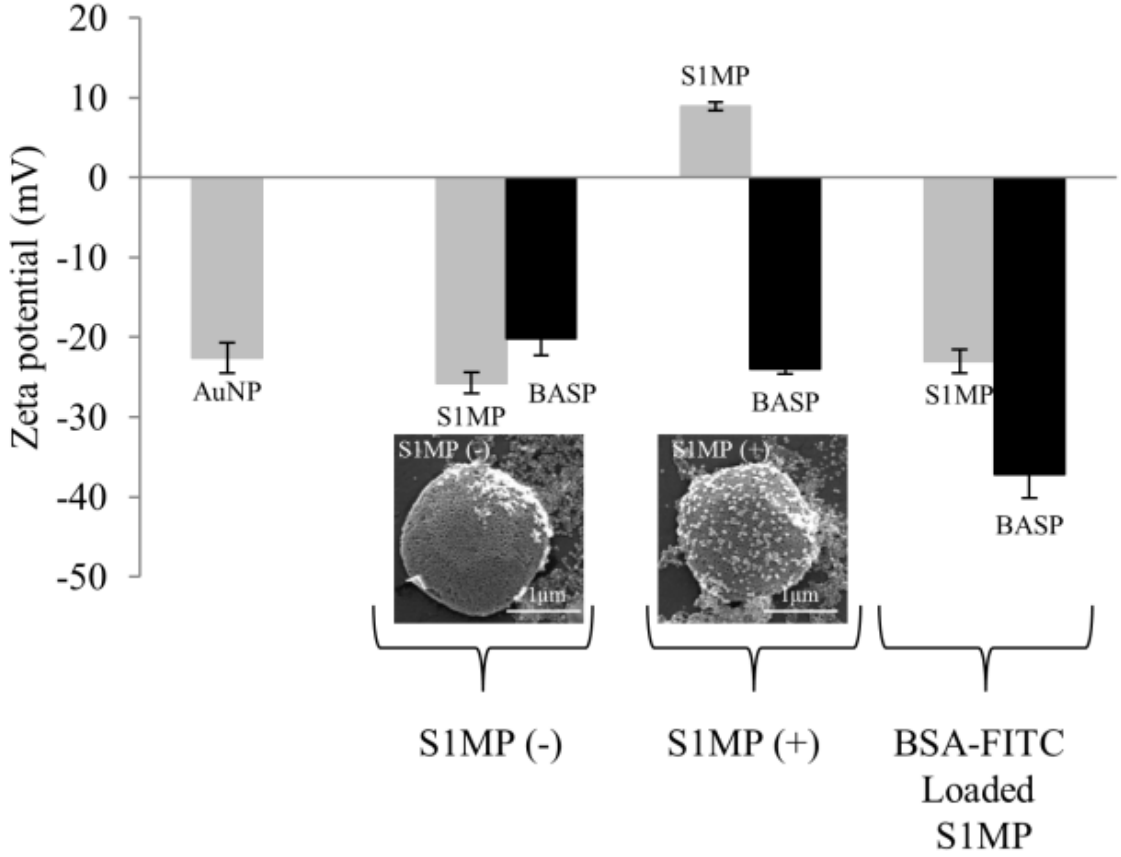

Figure 16: Effect of surface zeta potential of S1MP on BASP formation. Zeta potential of BASP and their components (inset) SEM image of BASP with S1MP(-) and S1MP(+) showing better adhesion of AuNP-bacteriophage networks to the S1MP(+) in comparison to S1MP(-). Reproduced from [83] with permission from The Royal Society of Chemistry.

3.2.3 Evaluation of BASP contact angle

"Hydrophilicity measurements on BASP showed that both types of BASP, containing either S1MP(+) or S1MP(-) (Figure 17) are more hydrophilic than AuNP solution alone, which can be important for avoiding non-specific uptake by cells of the reticuloendothelial system, as shown for nanovectors modified on their surface with hydrophilic polymers, such as PEG [116]." [83]

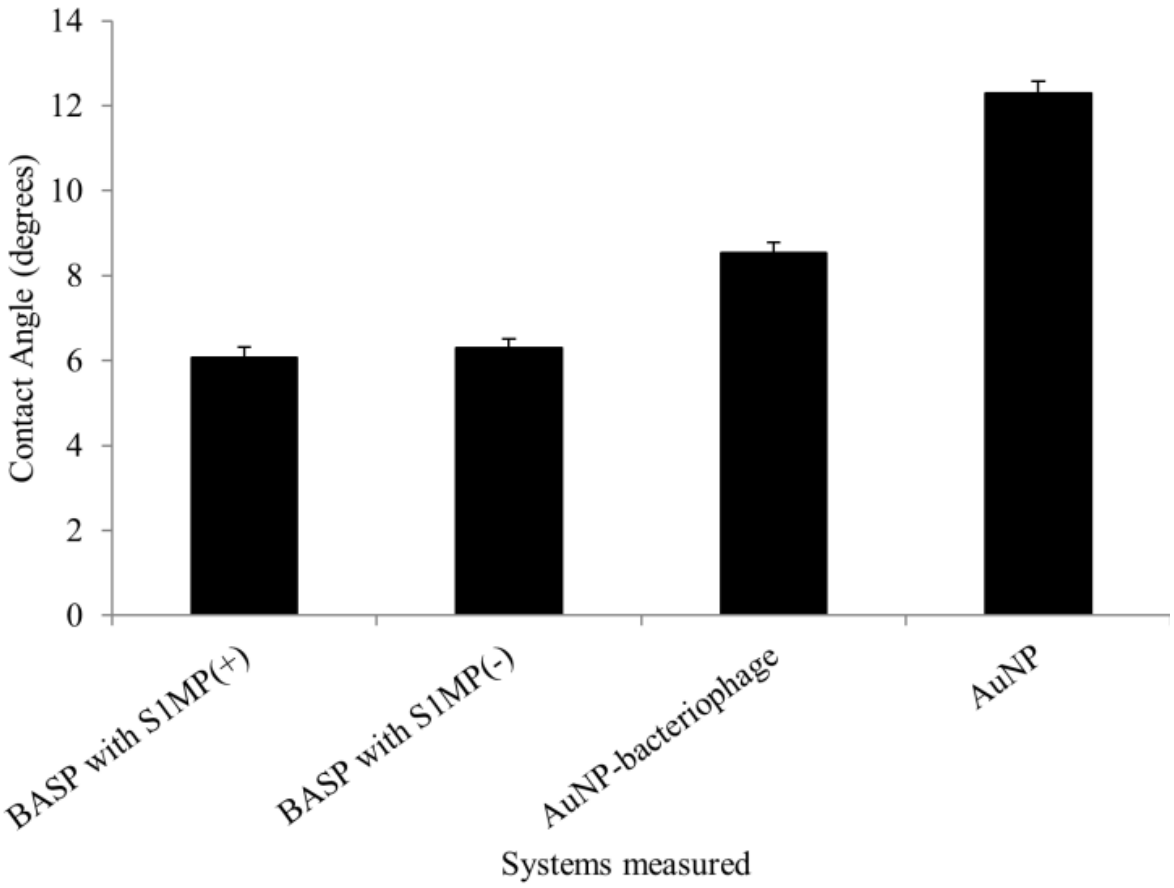

Figure 17: Contact angle measurements of BASP showing an increase in hydrophilicity in comparison to AuNP or AuNP-bacteriophage. Reproduced from [83] with permission from The Royal Society of Chemistry.

3.2.4 Spectral characteristics of BASP

"As mentioned above, the formation of AuNP-bacteriophage networks can be monitored in real-time using UV-Vis spectroscopy. Instantaneous interaction between the components of AuNP-bacteriophage networks in successive serial dilutions of the bacteriophage solution ($5x10^6$ TU/µL to $5x10^5$ TU/µL) is indicated by the broadening and reduction of UV-Vis absorbance at 530nm and simultaneous increase in the absorbance at NIR wavelengths between 650nm and 800nm.[105] This observed 3-4 fold increase in NIR absorbance occurs within 20sec of the addition of AuNP to bacteriophage. The AuNP-bacteriophage with enhanced NIR absorbance are then pooled together and incubated with S1MP to form BASP. The increase of the absorbance in the NIR region was maintained following the formation of BASP (Figure 18)." [83]

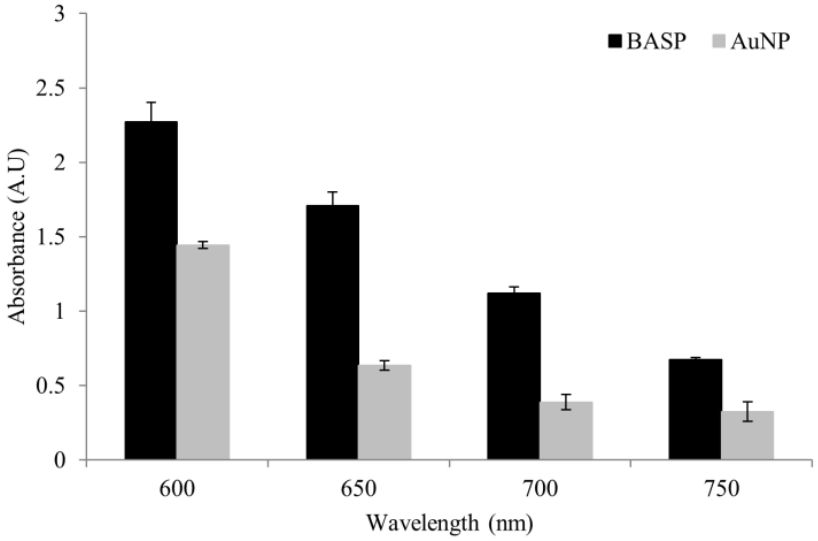

Figure 18: UV-Vis spectra of BASP show 2-3 fold increase in the NIR absorbance of BASP in comparison with the same concentration of AuNP. Reproduced from [83] with permission from The Royal Society of Chemistry.

"The high absorbance in the NIR region enables the use of spectral properties of the systems for diagnostic and therapeutic purposes. As an example, use of SERS as a diagnostic tool was investigated and the NIR-SERS spectra of BASP were recorded. As shown above, AuNP is closely associated with bacteriophage and S1MP in BASP. The close association of AuNP to bacteriophage facilitated an increase (~2000 fold) in the signature Raman peaks of the bacteriophage major coat proteins (such as phenylalanine and alanine). The data presented in Figure 19 illustrates the enhancement of unique peaks, namely wavenumbers 1022cm^{-1}, 1001cm^{-1} and 995cm^{-1}[117; 118; 119], in the NIR-SERS spectra of bacteriophage associated with the BASP." [83]

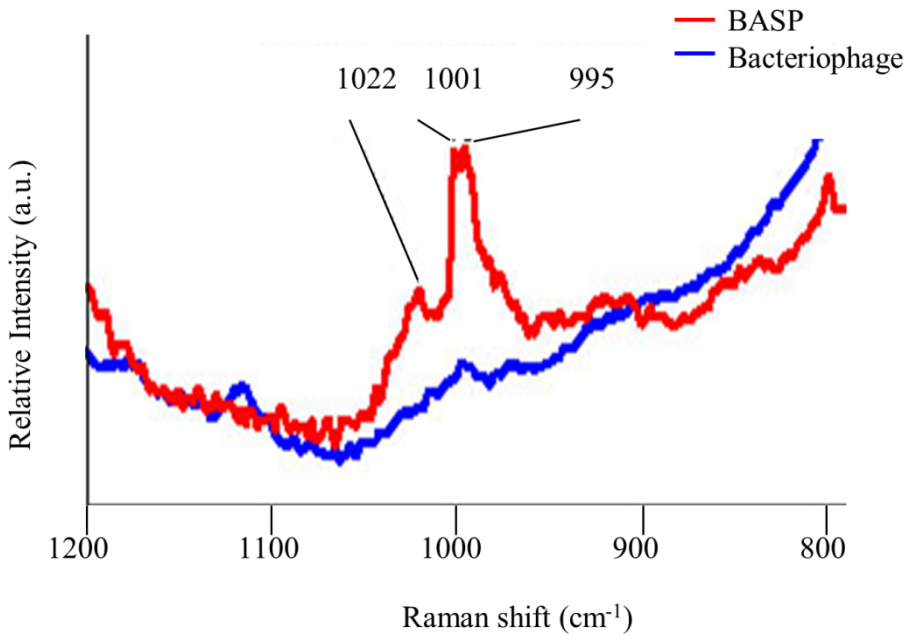

Figure 19: Detection of BASP using NIR-SERS signal of bacteriophage in close association with AuNP and S1MP. Reproduced from [83] with permission from The Royal Society of Chemistry.

3.2.5 Heating efficiency of BASP

"We also investigated the NIR photothermal conversion property of BASP in deionized water. When irradiated by a NIR laser the temperature in BASP increased by 10°C from room temperature within 10min while the AuNP did not heat up significantly (Figure 20). The agglomerations of AuNP seen in BASP absorbed NIR photons from lasers resulting in temperature increase. This heat generation triggered by NIR laser irradiation could potentially be used for thermal ablation." [83]

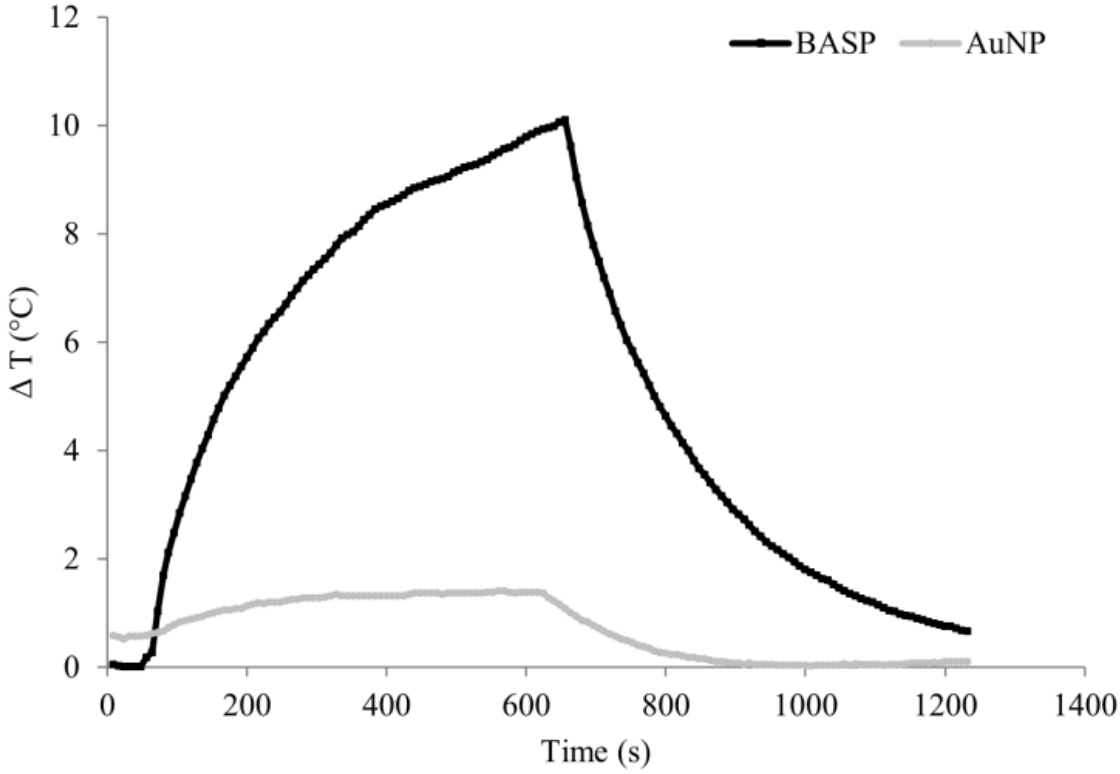

Figure 20: Temperature as a function of NIR laser exposure time of AuNP and BASP. Reproduced from [83] with permission from The Royal Society of Chemistry.

3.3 Loading efficiency of BASP

3.3.1 Superparamagnetic iron oxide nanoparticles

"Payload carrying capacity is another important consideration when designing nanovectors [59; 120]. In MSV, S1MP chemically modified on their surface have a significantly lower loading capacity of S2NP than unmodified S1MP, due to the unavailability of sufficiently open pores [75]. Here we evaluated the encapsulation efficiency of BASP by incorporating either amine functionalized SPION (15nm) or carboxylated QD (15nm). Post-assembly of AuNP-bacteriophage networks on the S1MP to form BASP retains the loaded SPION (1.17±0.34ng of iron/µg of silicon, i.e. ~100%) when compared to naked S1MP (Figure 21A). In contrast, ESTA-S1MP showed 70% lower loading (0.33ng/µg of silicon) similar to previously published study [75]. This demonstrates the ability of BASP to maintain the loading efficiency of S1MP while coupling targeted bacteriophage to their surface. This simple technique of coupling the targeting moiety to the vector enables both targeting as well as efficient payload delivery. NMR relaxometry data also corresponded to the loading efficiency, with SPION loaded S1MP exhibiting the shortest transverse relaxation time as shown in previous work.[78] Correspondingly, the r2 relaxivity (normalized to iron oxide concentration) of the SPION loaded BASP (162.09$mM^{-1}s^{-1}$) was half that of SPION loaded S1MP (258.75$mM^{-1}s^{-1}$) while that of SPION loaded ESTA-S1MP was significantly lower (98.63$mM^{-1}s^{-1}$) (Figure 21B). Conversely, the T2 relaxation times were short for SPION loaded S1MP and BASP (Figure 21C). The relaxation time of BASP (68.31msec) was almost twice as long as that of S1MP (39msec) but about 5 times shorter than that of ESTA-S1MP (354.4msec). These data show that BASP loaded with SPION maintain their

ability of exhibiting transverse relaxation and hence may be used for magnetic imaging applications." [83]

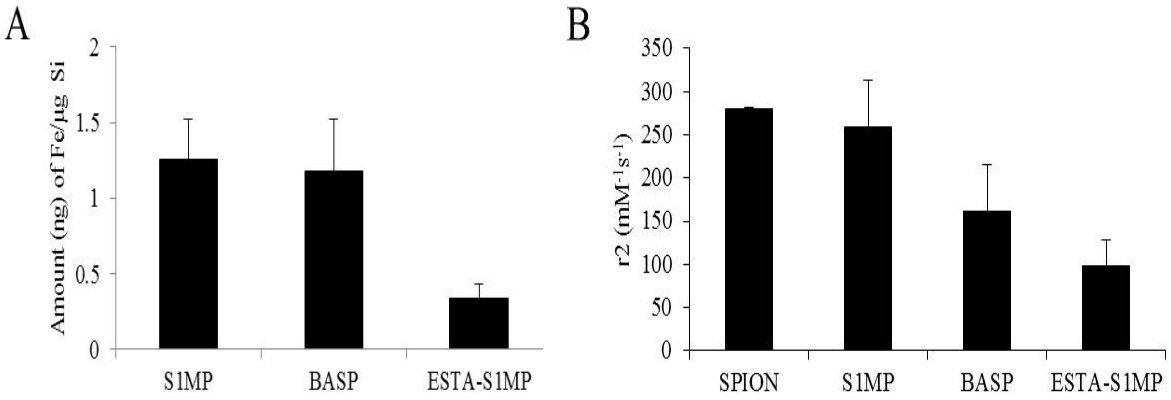

C

Sample	T2 relaxation (msec)
S1MP	3239.7
SPION	3.68
SPION loaded S1MP	39
SPION loaded BASP	68.31
SPION loaded ESTA-S1MP	354.4

Figure 21: Loading of SPION into BASP. (A) Iron content analysis in S1MP, BASP and ESTA-S1MP following loading of SPION using the wet incipient method as quantified by ICP-OES; (B) Comparison of transverse relaxivity, r2 and (C) relaxation times, T2, of SPION loaded particles. Reproduced from [83] with permission from The Royal Society of Chemistry.

3.3.2 Quantum dots

"Next we considered if loaded S2NP were closely associated with S1MP pores or were released from S1MP during BASP formation. QD loading into S1MP and BASP was comparable with 4.5±0.45ng of cadmium loaded in $1.5x10^8$ silicon particles in both naked S1MP and BASP suggesting that QD were not lost during BASP formation. To determine if the QD escaped out of the S1MP and were trapped in the AuNP-bacteriophage networks, we visualized the systems using fluorescence microscopy. We would expect unassociated QD (Figure 22, green) to bind non-specifically to the AuNP-bacteriophage [121]. However, we observed specific localization of the QD (yellow due to co-localization) with S1MP (Figure 22, red) and an absence of any non-specific staining outside the S1MP. AuNP-bacteriophage networks incubated with QD served as controls. We observed non-specific labeling of bacteriophage fibers (green) interspersed with AuNP (red dots)." [83]

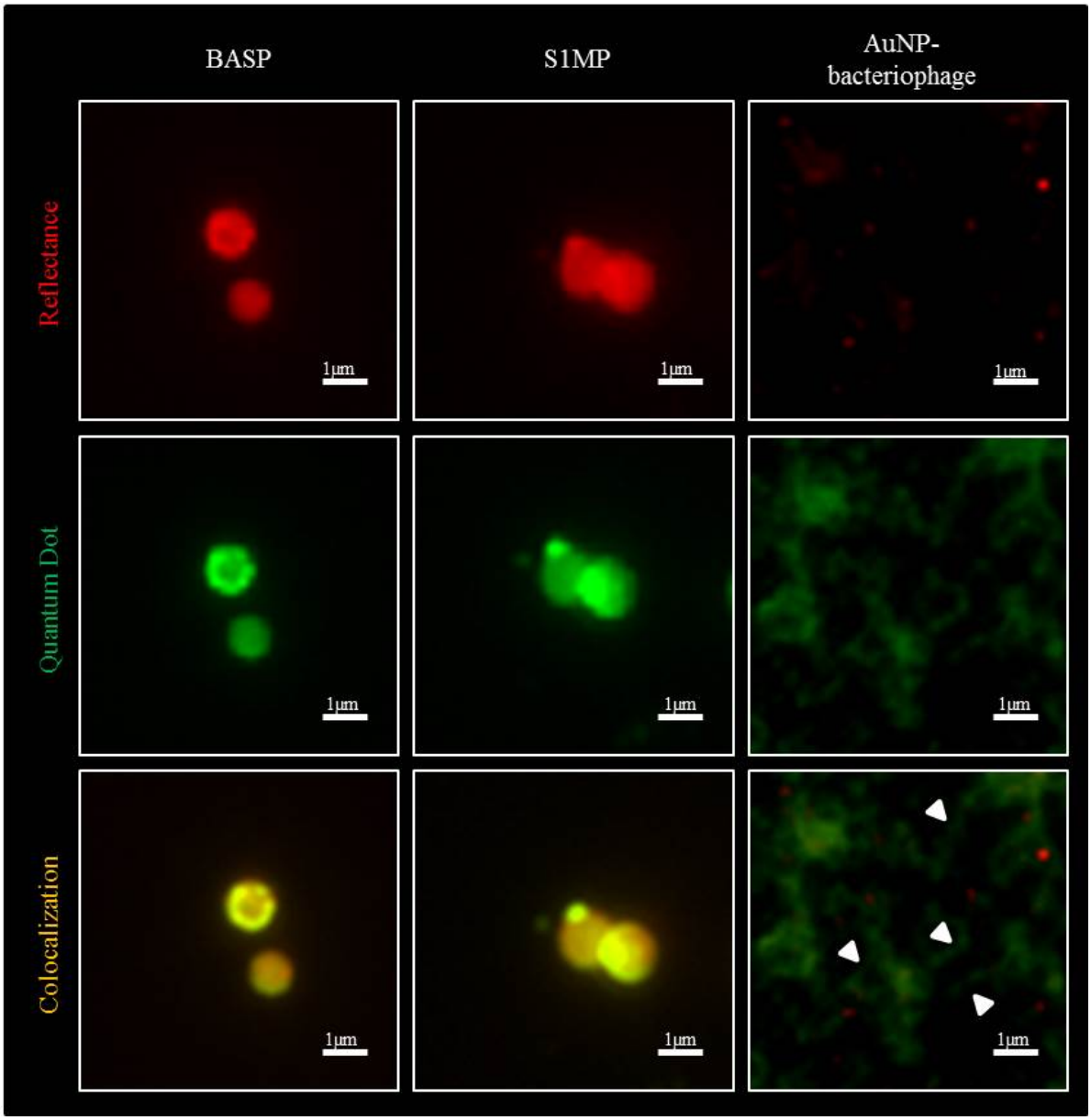

Figure 22: Loading of quantum dots into BASP. Fluorescence microscopic images of QD (green) loaded S1MP and BASP (red) showing S1MP colocalization with QD (yellow). In a control experiment, free QD nonspecifically bound to AuNP-bacteriophage networks (arrow heads) enable the visualization of the bacteriophage fibers (green) while the AuNP appear as red dots. Reproduced from [83] with permission from The Royal Society of Chemistry.

3.3.3 BSA-FITC loading

The macromolecule entrapment efficiency was measured by using a model protein molecule, fluorescently labeled albumin, and was determined to be highly efficient at 85-90%. We used this compound to mimic the loading of the cytotoxic nanodrug, Abraxane® (albumin bound paclitaxel). Since BSA-FITC is a negatively-charged molecule, we loaded it into S1MP(+). It can be seen in Figure 14, that the loading process reverted the zeta potential of S1MP(+) from ~10mV to -30mV demonstrating high efficiency of encapsulation of the protein model.

3.4 Biodegradation of BASP

3.4.1 *In vitro* degradation

"Degradation of the drug delivery system in biological fluids is an important characteristic that determines drug release kinetics as well as biocompatibility of the vector. We evaluated the degradation kinetics of BASP in simulated *in vivo* conditions such as 100% FBS at 37°C under constant motion. SEM micrographs (Figure 23A) and ICP-OES analysis (Figure 23B) show that the presence of AuNP-bacteriophage networks on S1MP in BASP does not affect the degradation kinetics of S1MP. Quantification of the percentage silicon release by ICP-OES showed complete degradation of both S1MP and BASP within 24h, consistent with previously published work.[62] Although the degradation profile of BASP was not different from naked S1MP, the adhesion of serum proteins on particles was significantly decreased in BASP as seen by the open pores in BASP in contrast to the covered appearance of the naked S1MP (Figure 23A). This could potentially translate into

the reduction of opsonization and hence non-specific uptake of particles by cells under *in vivo* conditions (data not shown)." [83]

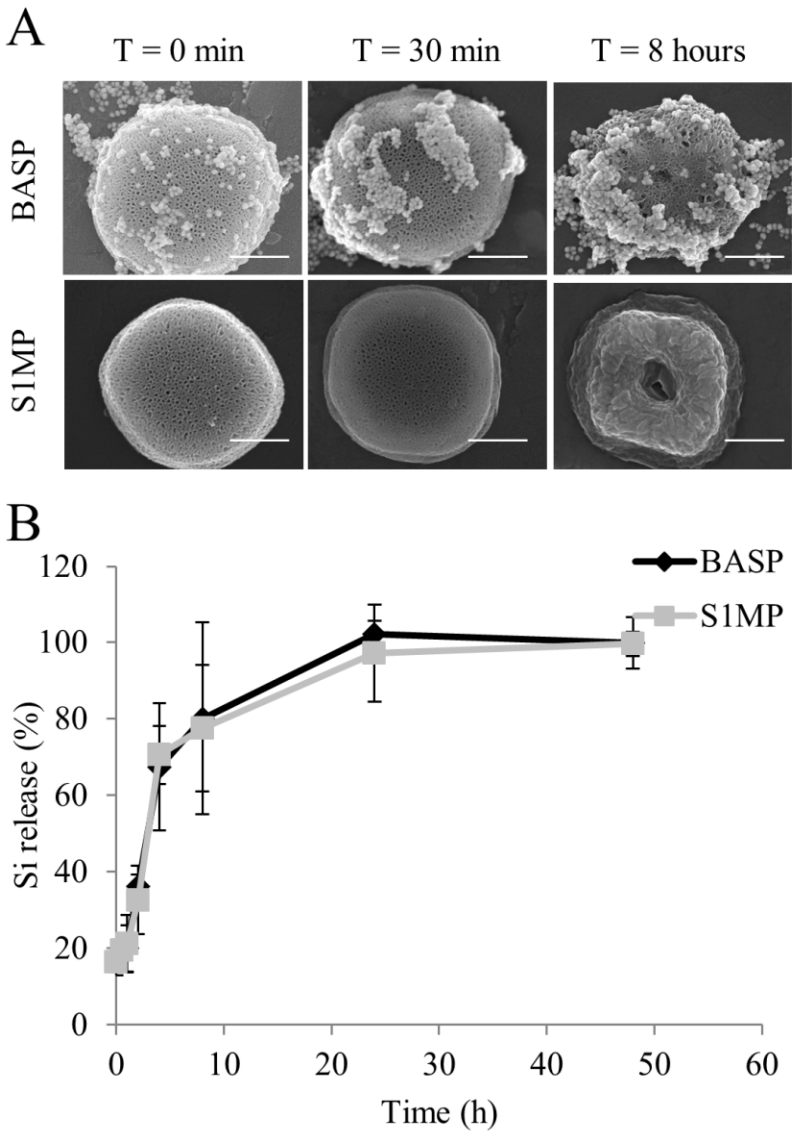

Figure 23: Time dependent degradation of S1MP and BASP in 100% FBS. (A) SEM micrographs showing the pattern of degradation of the porous silicon particles over time (Scale bar = 500nm); (B) ICP-OES quantification of the degradation profile expressed as a percentage of total silicon content released from S1MP over time. Reproduced from [83] with permission from The Royal Society of Chemistry.

3.4.2 *In vivo* integrity

"Since the BASP is not a chemically conjugated assembly and is based on electrostatic interactions, which can be impaired in complex biological fluids (e.g. blood), it was important to verify the integrity of the systems following *in vivo* intravenous administration. We administered CRKL targeted BASP through the tail vein to orthotopic breast tumor bearing mice and analyzed tumor and liver tissue sections for the integrity of the systems *in vivo*. Tumor tissue from mice injected with BASP containing fluorescently labeled bacteriophage show co-localization of the bacteriophage (red) and S1MP (Figure 24A). Similarly, immunohistochemistry staining for bacteriophage (Figure 24B, brown) in tumor tissue shows specific association with S1MP. Thus, we can infer that there is a close association of the bacteriophage and S1MP even after intravenous administration. Hyperspectral imaging provides unique reflectance spectral analysis of materials. Combined with dark field microscopy (Figure 24C(i)), hyperspectral imaging was used to identify the location of BASP. Once the particles were identified, spectra from different pixels on the particles were collected and grouped into libraries (S1MP and AuNP) (Figure 24C(ii)) according to the shape of the spectra. Mapping these libraries to the image of liver tissues shows co-localization of the silicon spectra and AuNP spectra (Figure 24C(iii)). The spectra collected for AuNP show a peak at approximately 650nm, which correlates with the red shift in the UV-Vis absorbance of BASP. These spectra based mapping confirm proximity of AuNP and S1MP and thus, the integrity of BASP." [83]

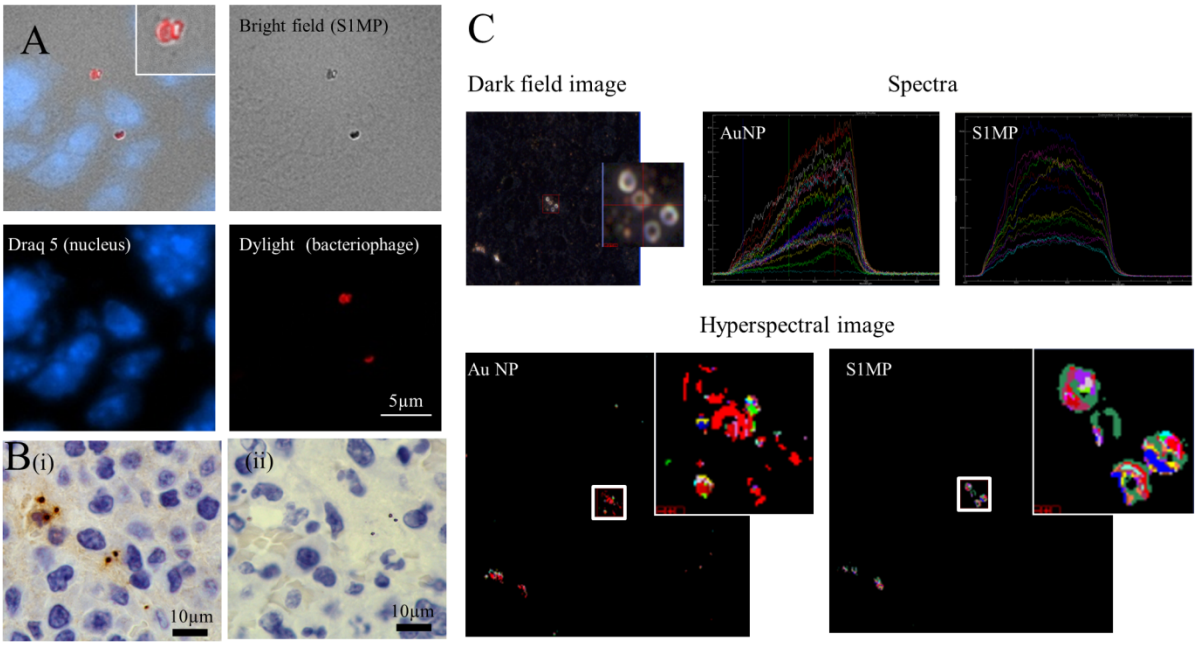

Figure 24: ***In vivo*** **integrity of BASP.** Mice bearing EF43.*fgf4* mammary allografts were injected intravenously with BASP. After a 4h circulation time, the animals were sacrificed and the tumor and liver were harvested and processed for histological analysis. (A) Fluorescence microscopy and (B) Immunohistochemistry analyses for bacteriophage show that the bacteriophage remains associated with S1MP and the assembly is not impaired in the circulation; (C) Hyperspectral images of the liver show superimposed spectral mapping of silicon and AuNP also confirming the close association of the AuNP and S1MP in the BASP. Reproduced from [83] with permission from The Royal Society of Chemistry.

3.5 *In vitro* targeting efficiency of BASP

BASP are designed to enhance the targeting of S1MP to the tumor. We evaluated the specificity of binding of CRKL targeted BASP to breast cancer and endothelial cell lines under static and simulated flow conditions using various microscopic techniques and flow cytometry.

3.5.1 Static conditions

Figure 25 shows flow cytometry data of HUVEC and HMVEC incubated with S1MP, non-targeted fd-tet BASP and CRKL targeted BASP. It was observed that endothelial cells uptake silicon particles non-specifically. There was no statistical significance in the amount of CRKL targeted BASP uptake vs fd-tet BASP or S1MP uptake in both cell types.

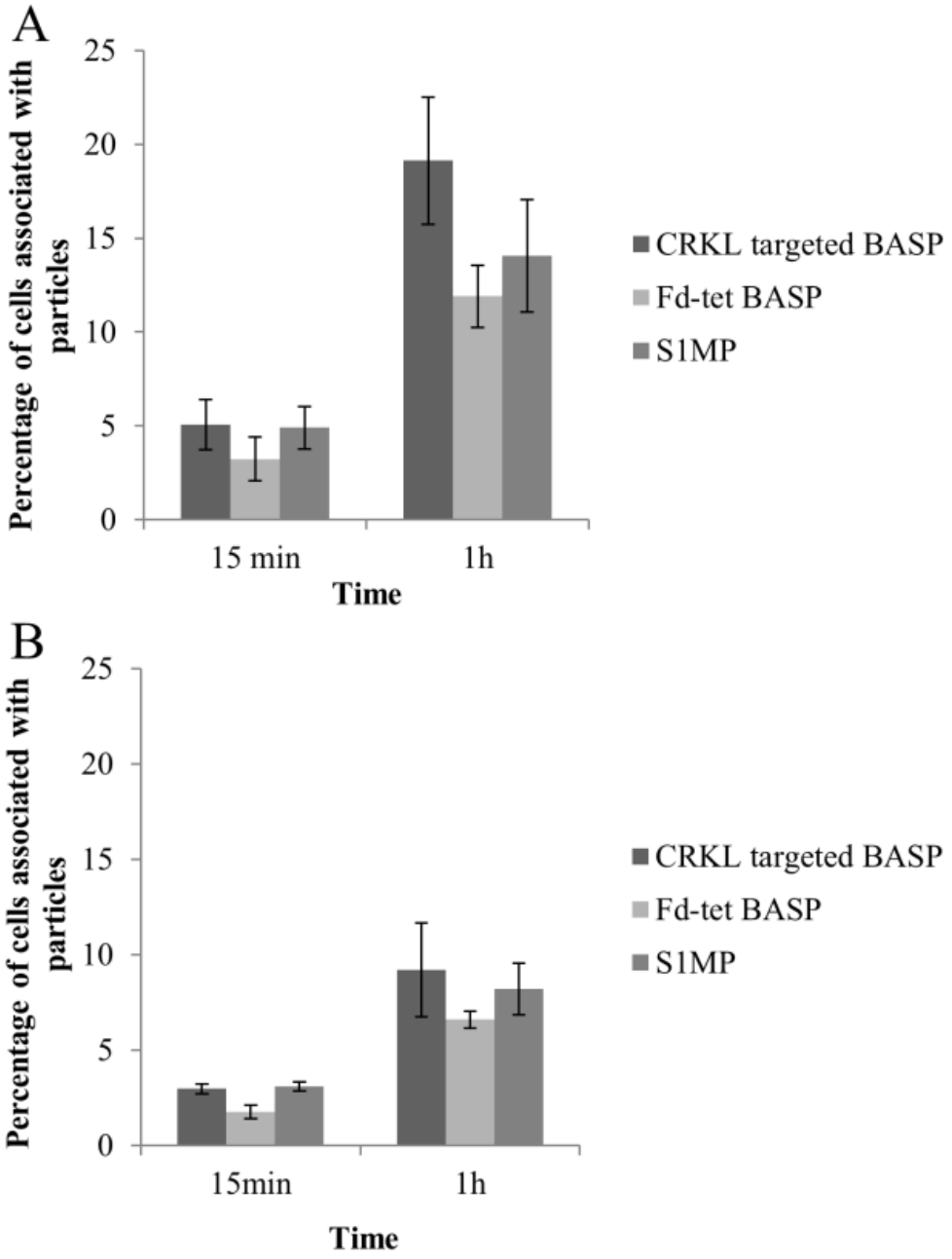

Figure 25: Association of BASP with cells *in vitro* under static conditions. Flow cytometric data showing the percentage of endothelial cells associated with BASP; (A) HUVEC and (B) HMVEC.

We also analyzed the mode of intracellular uptake by confocal and electron microscopy (Figure 26). MCF7 cells expressing the highest level of CRKL among the cell lines tested were used for these experiments. Confocal images demonstrate that CRKL targeted BASP are associated significantly more than the control groups to MCF7 cells. SEM micrographs show that after 6h of incubation some of the naked S1MP and control fd-tet BASP were associated with the cell surface. No internalization of S1MP by the breast cancer cell was observed in these experiments. In contrast, CRKL targeted BASP were internalized by breast cancer cells, indicating the specificity of uptake in the case of CRKL targeted systems. The timeline of internalization is significantly longer than in previous studies performed on endothelial cells where the cells start internalizing untargeted S1MP within 15 min [115; 122]. This could be explained by the fact that the cells used in this study are of epithelial origin and are not considered as professional phagocytes.

TEM has shown that the CRKL targeted BASP appear in a perinuclear vacuole/phagocytic vesicle. The system appears intact with AuNP surrounding S1MP hemispherical structure. This observation is important in light of the diagnostic potential of the system as the close proximity of AuNP and S1MP is essential for their detection using imaging techniques such as CT or NIR-SERS.

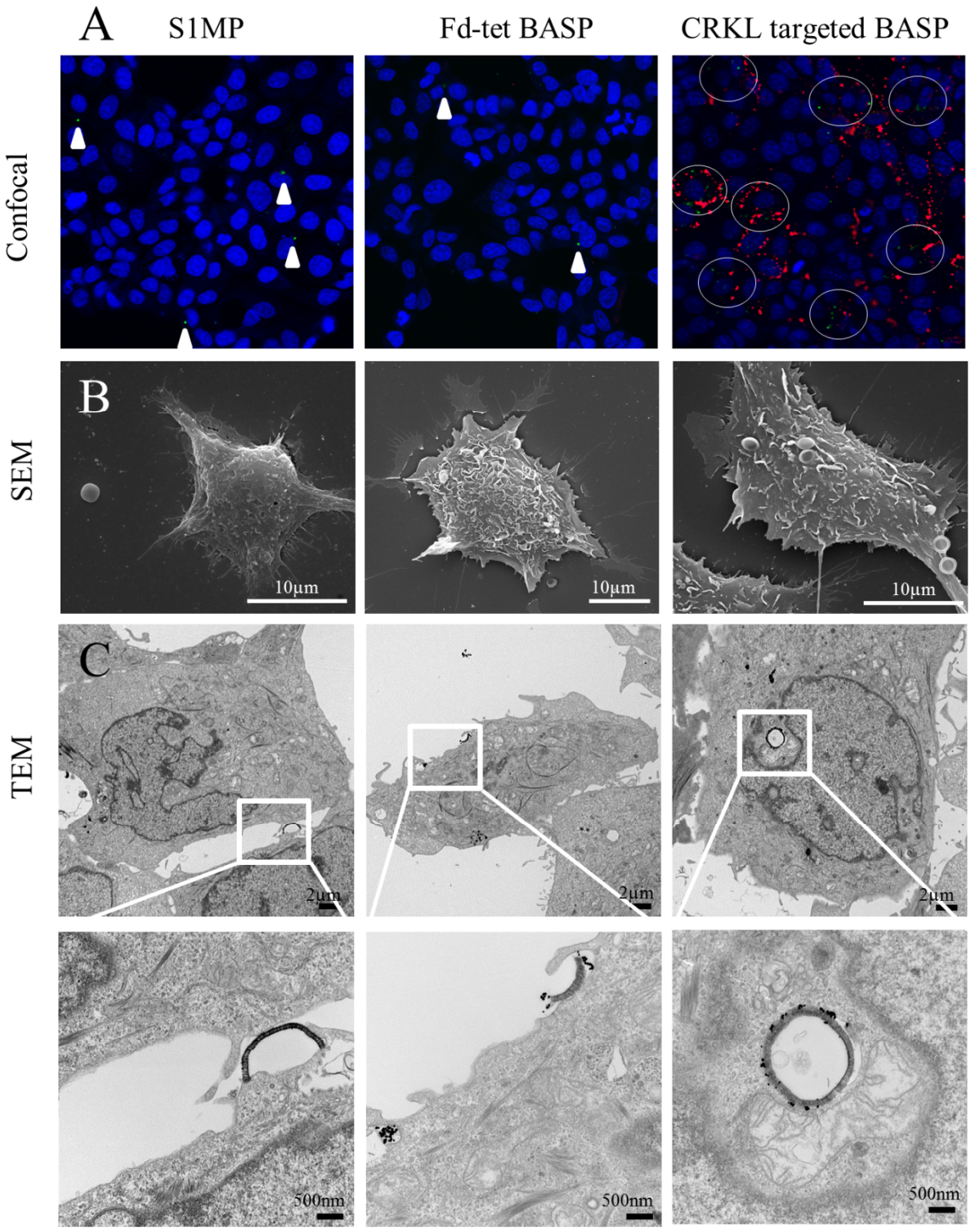
A
S1MP
Fd-tet BASP
CRKL targeted BASP
Confocal
SEM
TEM
B
C
10μm
2μm
500nm

Figure 26: Association and internalization of BASP in MCF7 cells. (A) Confocal microscopy images showing enhanced association of CRKL targeted BASP (circles) compared to non-targeted controls (arrowheads). Green – S1MP, Red – Bacteriophage, Blue – Nucleus; (B) Scanning electron micrographs showing higher number of CRKL targeted BASP associated/cell when compared to the other two particle types; (C) Transmission electron micrograph showing perinuclear localization of CRKL targeted BASP.

3.5.2 Effect of shear stress

Particle margination and specific adhesion under shear stress was studied using Bioflux microfluidic channel plates, traditionally used for leukocyte adhesion and rolling analysis and platelet aggregation [123]. A schematic representation of the setup is shown in Figure 27A. It is comprised of a Bioflux 48 well interface, an inverted fluorescence microscope with a heated biological chamber and Bioflux 200 controller. The hydrodynamic conditions in the channel are controlled by the pneumatic pressure applied in the inlet and outlet wells of the channels. Figure 27B compares the number of particles adhering to cell monolayers in the presence and absence of endothelial cell activation at wall shear rates (S) of 10 s^{-1} (shear rate in tumor microvasculature) and 100s^{-1}(shear rate in normal capillaries) [124; 125]. In contrast to the results in static conditions, it was observed that the number of CRKL targeted BASP adhering to both types of cells, HUVEC and HMVEC were significantly higher than fd-tet non-targeted or S1MP themselves at low shear rates of 10s^{-1}. This difference is even more prominent (2-fold) in the case of HMVEC (microvasculature cells) when compared to HUVEC (normal endothelial cells). As expected, at 100s^{-1},

corresponding to shear rates in the normal microvasculature, the number of particles adhering to the cells was significantly reduced regardless of the activation condition of the cells or the targeting ability of the particles.

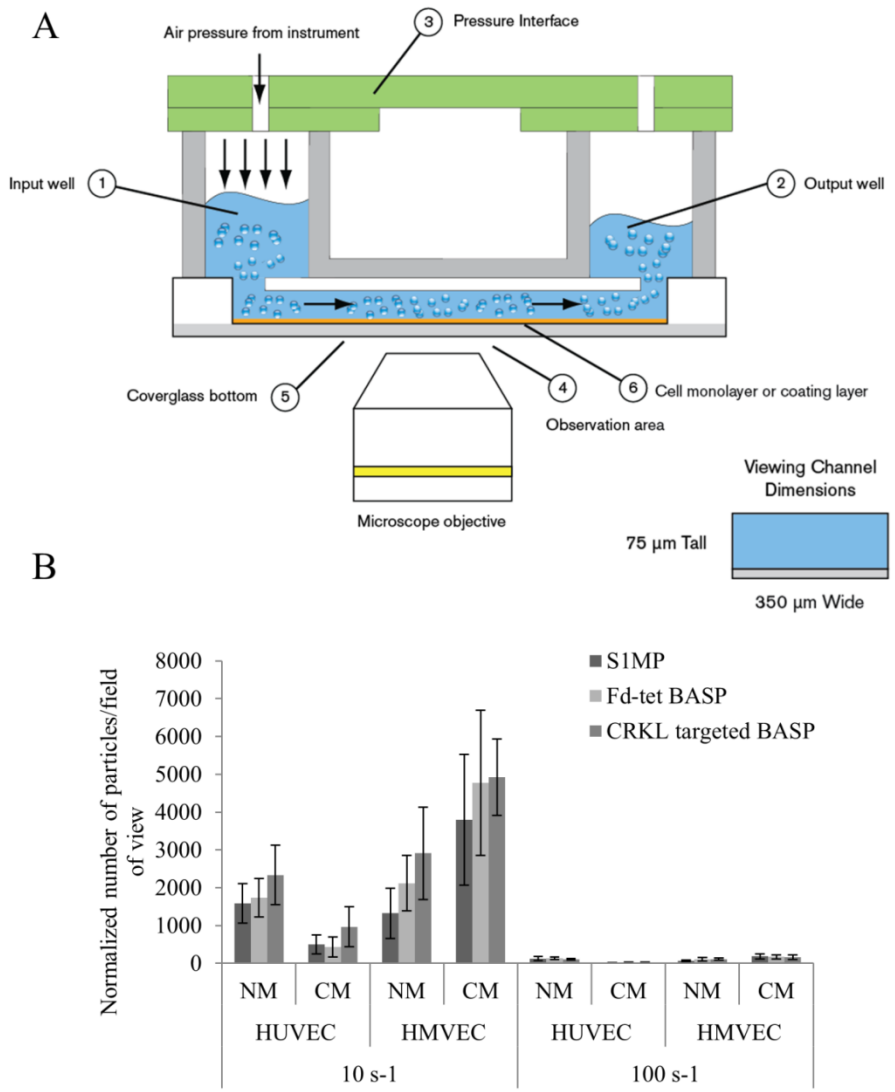

<u>Figure 27:</u> Effect of shear stress on the adhesion of CRKL targeted BASP to endothelial cells. (A) Schematic diagram of the set up showing Bioflux 200 – 48 well flow chamber with dimensions of the viewing channel and (B) Quantitative measurement of the number of particles adhered to endothelial cells after a flow for 1h at 10 and 100 s^{-1} shear rates.

3.6 *In vivo* targeting efficiency

To evaluate the tumor accumulation of BASP, 10^9 1.6μm hemispherical particles (S1MP, fd-tet BASP or CRKL targeted BASP) were injected via the tail vein into mice bearing orthotopic EF43.*fgf4* tumors. Mice injected with PBS served as negative controls. The animals were sacrificed 4h after injection and the tumor was harvested for silicon content analysis by ICP-OES. Figure 28A shows the silicon content of S1MP, fd-tet BASP and CRKL targeted BASP in the tumor. The CRKL targeted BASP showed upto a 3 fold higher accumulation in the tumor tissue when compared to S1MP alone.

Similar experiments using fluorescently labeled 1x0.4μm discoidal particles (10^8/mouse) were conducted and analyzed using intravital microscopy. Figure 28B shows representative images of particle accumulation in the tumor 1h after injection. The accumulation seen was mainly within the first few minutes, after which it leveled off. The number of particles accumulated in the tumor of mice injected with CRKL targeted BASP was almost 4 fold higher than the number of particles that accumulated in the other 2 categories (Figure 28C).

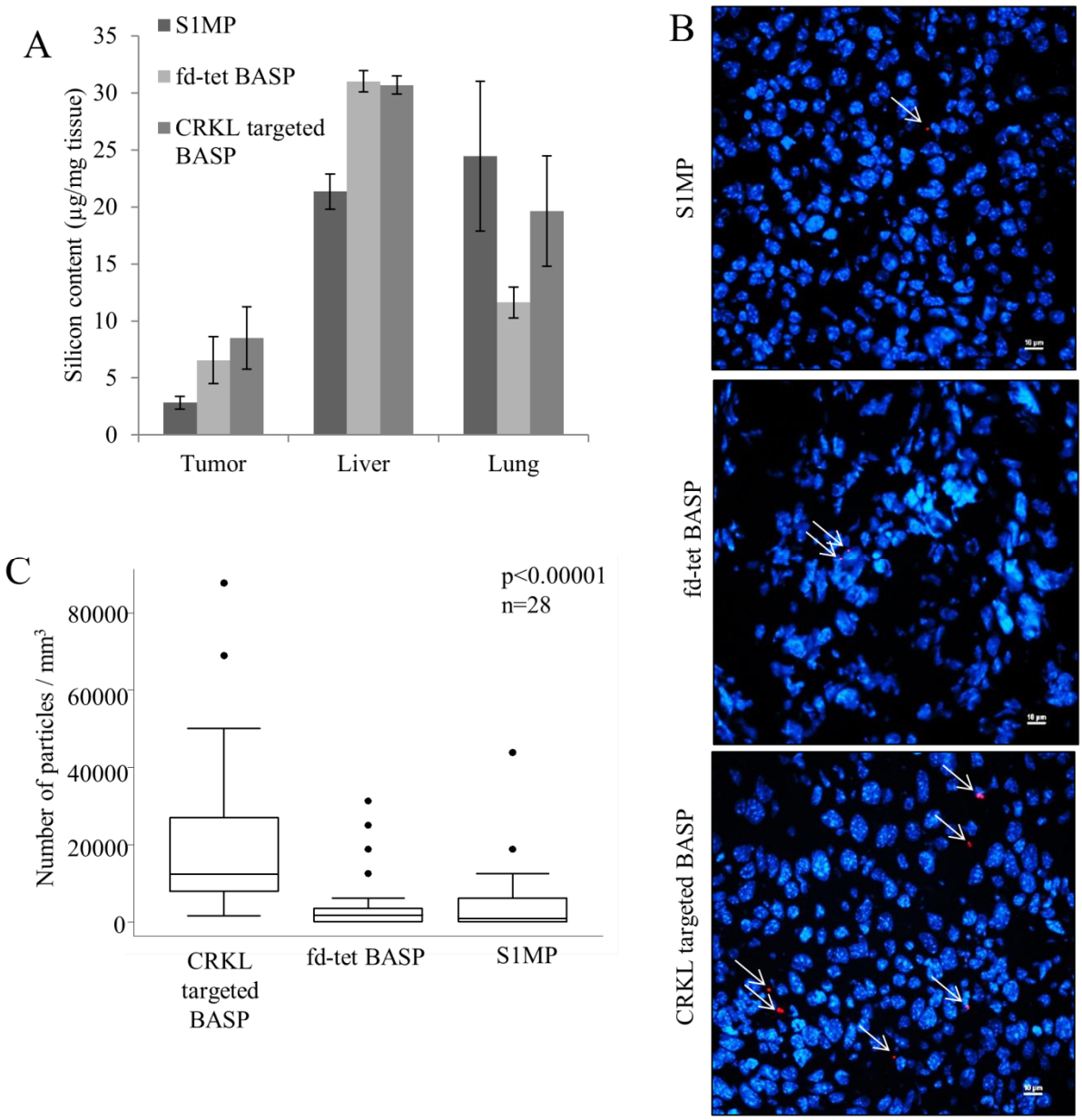

Figure 28: BASP accumulation in breast tumor models. (A) Silicon content in different tissues as measured by ICP-OES; (B) Confocal images of tumor tissue showing enhanced particle (red marked by arrows) accumulation in the CRKL targeted BASP injected mice and (C) Semiquantitative analysis of the number of particles accumulated in the tumor as calculated from images captured at the end of the experiment.

The speeds of particles (1x0.4µm discoidal) injected during the intravital microscopic analysis were measured post acquisition using 2D tracking module in NIS elements software. The speeds of particles were orders of magnitude different for each case. The CRKL targeted BASP travelled at speeds of about 10µm/s, while the fd-tet non-targeted BASP were about 100µm/s and S1MP were the fastest at about 600µm/s (Figure 29).

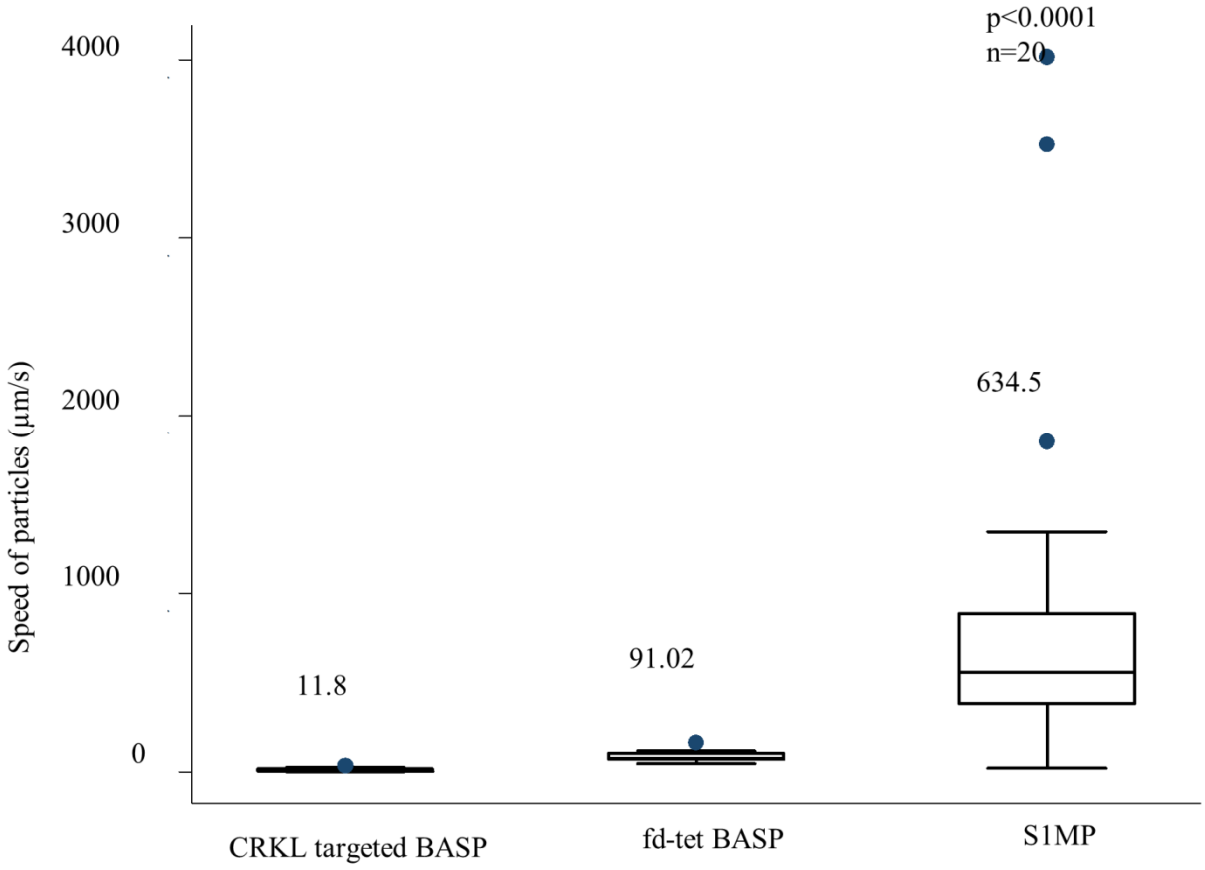

Figure 29: Speed of particles flowing through the tumor vasculature as measured using 2D tracking module in NIS elements

3.7 Therapeutic efficacy

Figure 30 shows the antitumor response of BASP in EF43.*fgf4* tumor bearing mice. Mice were administered Abx, S1MP-Abx, fd-tet BASP-Abx or CRKL targeted BASP-Abx (75mg/kg) twice a week. The Abx and S1MP-Abx treated mice showed marked increase in tumor size (mean final tumor volume 1.1cm^3), while CRKL targeted BASP-Abx treated mice showed minimal increase (mean final tumor volume 0.4 cm^3).

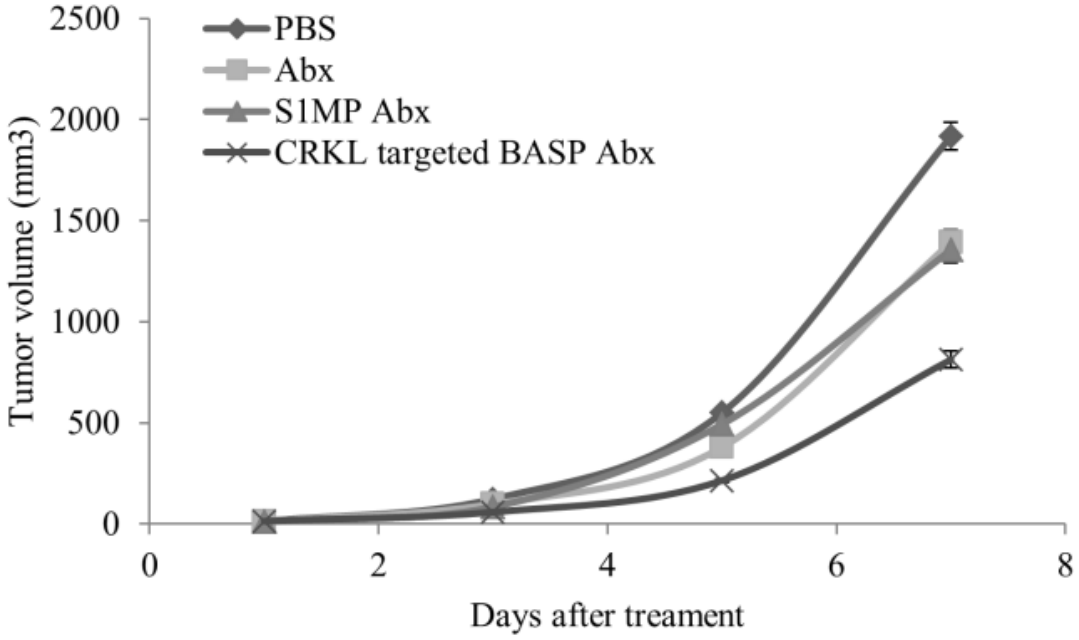

Figure 30: Therapeutic efficiency of Abraxane loaded BASP. Tumor size as a function of time following treatment with Abx, S1MP Abx or CRKL targeted BASP Abx.

3.8 CRKL as a soluble biomarker

As mentioned earlier, a recent study showed that intracellular CRKL was secreted into the extracellular milieu in prostate cancer *in vivo* models (Mintz et al). Our results also confirmed the presence of CRKL on breast cancer cell lines as well as on endothelial cell lines. Based on these, we proposed that the "secreted" CRKL could be detected in both cell culture supernatants as well as the blood. For this purpose, we tested for the presence of soluble CRKL in cell culture supernatants, plasma from tumor bearing mice as well as plasma from clinical breast cancer patients using ELISA.

3.8.1 Evaluation of soluble CRKL in *in vitro* and *in vivo* samples

Conditioned media from cell culture supernatants and serum from breast tumor bearing mice were analyzed by ELISA for secreted CRKL. CM from human breast cancer cell line, SUM159, showed over a 20 fold higher CRKL concentration than that from normal breast epithelial cell line MCF10A (545±7 vs 26±5pg/mL, respectively) (Figure 31A). Mean serum levels of secreted CRKL from mice bearing human derived breast tumors were also significantly higher than control mice. In particular, mice grafted with patient derived tumors had about 13 fold higher serum levels of CRKL than control mice (486±130 vs 37±21pg/mL), comparable to the results from *in vitro* studies (Figure 31B).

3.8.2 Evaluation of soluble CRKL in clinical samples

Soluble CRKL in sera from 29 breast cancer patients and 10 normal donors were measured by ELISA. The median CRKL concentrations in breast cancer patients' sera were more than 1.4 fold higher than in healthy donors (4400±2560 vs 1860±1840 pg/mL, respectively, $p<0.05$). Patients with advanced clinical disease, i.e. stage 3 and 4, exhibited a 2.8 fold (5300±2300pg/mL, $p<0.005$) increase in the serum CRKL concentration in

comparison to healthy donors (Figure 31C). Serum levels of CRKL were elevated from the median value in more than 90% of patients with advanced disease (T3 and T4) and in 100% of patients with metastatic disease. The sera from patients (n=4) who had not undergone any treatment had higher values than those patients who were undergoing treatment (5800±2000 vs 3600±2700pg/mL, respectively, p= 0.13).

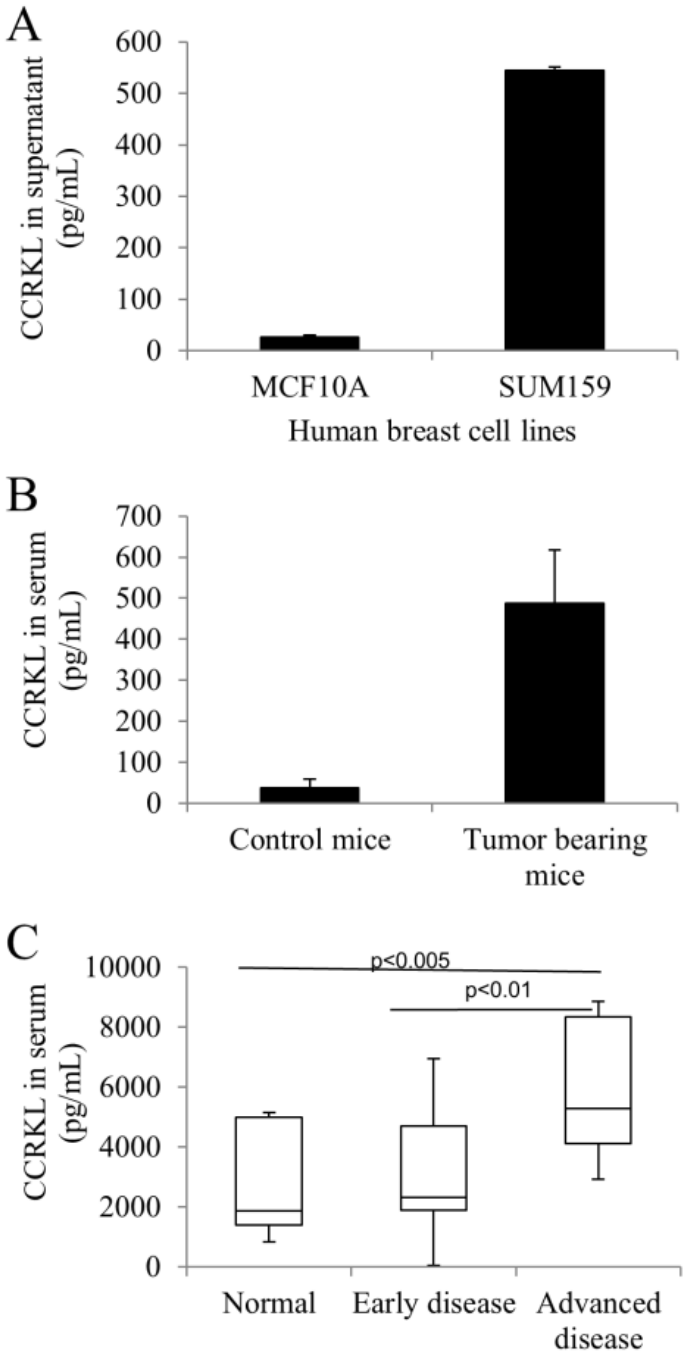

Figure 31: Assessment of secreted CRKL levels in *in vitro, in vivo* and clinical samples. The CRKL concentration (C_{CRKL}) was measured in (A) cell supernatant (B) serum from mice bearing patient derived breast tumor xenografts and (C) serum from breast cancer patients using ELISA.

CHAPTER 4: DISCUSSION

Nanovectors are increasingly used as therapeutic and imaging contrast agents in cancer due to their ability to bypass biobarriers and selectively accumulate in the tumor site [126]. An array of nanovectors has been developed with different features and functionalities over the last few years. While tumor-specific homing of the first nanoparticles took advantage of the disorganized and leaky vasculature of tumors and relied on passive accumulation due to the EPR effect, later nanovectors included more active targeting techniques such as conjugation of molecular recognition moieties, externally guided accumulation by magnetic focusing, etc. The addition of tumor targeting moieties onto the first generation nanovectors has its share of unpredictability depending on the affinity of the moiety to its target. If the affinity is very high, then the nanovectors bind very well to the cells that it first comes in contact with, such as the endothelium thereby limiting their ability to extravasate into the tumor [12]. It is not feasible for a single class of nanovectors to bypass all the sequential biological barriers and reach the tumor in significant quantities, irrespective of their geometry and targeting specificity. A third generation of nanovectors has been proposed that is designed to overcome the time-sequential biobarriers and deliver multiple payloads to the tumor specifically. These “multistage” nanovectors are an assembly of nanovectors nested within each other, each with unique functions [72].

Physical characteristics, such as geometry of nanovectors have been recognized as important parameters that dictate their interaction with biological systems both at the cellular and vascular level [60; 127; 128]. Though size of nanovectors itself does not affect phagocytosis significantly, the shape has a great impact on their uptake by cells. This was

studied in macrophages, where, ellipsoidal particles were compared to spherical particles. Depending on the direction of interaction of ellipsoidal nanovectors and cells, a differential uptake was noticed. On the other hand, phagocytosis of spherical particle were mostly uniform due to its symmetry [129]. Vascular interactions have also been linked to size, shape and density of particles mathematically and experimentally. Under shear flow, discoidal particles exhibited higher adhesion to endothelial cells than spherical particles [127; 130]. Based on these mathematical models, our lab designed non-spherical porous silicon microparticles that serve as first stage particles (S1MP) in multistage vectors. The S1MP are designed to facilitate their preferential concentration on tumor vasculature and the encasing of second stage nanoparticles (S2NP). The S2NP which in turn carry therapeutic or imaging agents are released into the tumor.

The S1MP are fabricated using photolithography and can be tailored to produce various geometries of particles, ranging from discoidal to hemispherical to cylindrical. The pore size and porosity can be tuned by electrochemical etching according to requirements. The pore sizes range from 5nm to 120nm in diameter [69]. Various studies with these particles have been conducted. S2NP, such as SPION [78], quantum dots [59], gadolinium nanotubes [80], paclitaxel containing micelles [79], liposomes [77] and hollow gold nanoshells [81] have been loaded into these particles. The surface of the S1MP has been decorated with peptides [74], thioaptamers [75], biomimetic leukocyte membrane [76] and agarose [24] to either facilitate tumor homing or lysosomal escape or avoid immune recognition.

While the above studies have demonstrated the successful loading and conjugation of targeting moieties independently, combining the two efficiently have been a challenge. The

design of nanovectors governs their accumulation at a specified site. The design parameters include size [131], shape [132; 133; 134], surface charge [135; 136; 137] and deformability [138]. Another important parameter is the surface decoration with targeting ligands specific to the disease microenvironment [139; 140].Typically, the addition of molecular targeting ligands on nanovector surfaces involve covalent conjugation chemistry that may impair the targeting ability of the biological entities as well as reduce the volume of pores available for loading active substances, in the case of porous drug carriers.

In this study, we demonstrate a simple method to immobilize molecularly targeted bacteriophage on S1MP without compromising its payload carrying potential. Immobilization of bacteriophage on various surfaces has been performed for use as antibacterial agents/surfaces [141]. However most of these reports use either covalent/chemical conjugation techniques or genetic modifications for the immobilization. These processes, as described above can be detrimental to the drug carrier or can be complicated and time consuming. We proposed the use of electrostatic interactions to assemble BASP, by co-incubation of S1MP, bacteriophage and AuNP. Since the formation of these electrostatic interactions is spontaneous, we were able to load the S1MP with S2NP and instantaneously cover with the AuNP–bacteriophage networks, thus avoiding loss of loaded S2NP.

Among the physical parameters involved in designing BASP, we studied the effect of shape, size, surface potential and porosity on the BASP formation. It was observed that shape and size of S1MP did not have an effect on the formation of BASP. However, the association of AuNP with S1MP was evidently better with positively charged, porous particles than their association with non-porous silica beads or negatively charged particles.

The porosity of particles provides an increased surface area with more sites for the interaction of the bacteriophage with the particles. This observation that porosity of S1MP enhances the adhesion of AuNP–bacteriophage networks is in agreement with previous studies on the effect of particle porosity on the efficiency of surface adsorption [142].

While positively charged nanovectors have greater efficiency in cell membrane penetration and internalization, compared to negatively charged particles, they also elicit more immune responses when in circulation [143]. On the other hand, negatively charged particles are better at avoiding recognition by the immune system. Our observation that positively charged S1MP form BASP more efficiently also has the advantage that the final BASP formed has a net negative charge and thereby could potentially avoid recognition by the immune system. Further, the negative charge might help in avoiding non-specific internalization of the BASP, allowing them to release S2NP into the tumor microenvironment.

The formation of BASP is characterized by a red shift in the UV-Vis absorbance of AuNP from around 530nm to 710nm explained by dipole-dipole interactions between AuNP when the interparticle distance becomes lesser than its diameter [109]. However, this red shift occurs at very specific ratios of bacteriophage and AuNP. At higher ratios of bacteriophage to AuNP, the placement of AuNP on bacteriophage is sufficiently large to avoid dipole-dipole interactions. In contrast, at lower ratios, the concentration of bacteriophage is very dilute and hence, majority of the AuNP are still in colloidal form and do not interact with each other. Thus, it is important to achieve a delicate balance in the relative concentrations of phage and AuNP during formation of the networks.

Red-shift in UV-Vis absorbance corresponds to an increase in the NIR absorbance. This can be used to advantage because most deep tissue imaging utilizes this NIR window (650-900nm), where hemoglobin is transparent [144], to discern function, localization, affinity and fate of nanovectors through their innate scattering properties [145]. Here we demonstrate that non-invasive, longitudinal imaging techniques such as NIR-SERS can be used to provide critical information at the molecular scale in real-time. Fingerprints of BASP, that appear when bacteriophage and S1MP are in close association with AuNP, can be used as signal reporters for monitoring the formation and presence of BASP. These photonic properties of BASP originating from the quantum confinement of AuNP in BASP are tunable based on the design of the system and offer a direct ability to assess their interaction within biological systems, providing diagnostic capability [83].

As discussed above, one of the major requirements of a good nanovector is high payload carrying capacity. However chemical conjugation of targeting moieties frequently hampers this feature [75]. Here, we demonstrated that S1MP retain their payload carrying capacity even after the incubation with AuNP-bacteriophage networks to form BASP. Solid nanoparticles such as SPION and quantum dots as well as protein molecules such as BSA-FITC (model drug molecule) were loaded into the S1MP successfully. This simple technique of coupling the targeting moiety to the nanovector enables both targeting as well as efficient payload delivery.

Having shown the efficient payload encapsulation, we studied the targeting ability of BASP. In our study, we hypothesized that an intracellular adaptor protein, CRKL, secreted by tumor cells into the microenvironment would bind to the extracellular domain of integrins on both tumor cells as well as endothelial cells' surface. We proposed that this extracellular

CRKL can serve as a good target for homing nanovectors to the tumor site. To confirm our hypothesis, we evaluated the surface localization of CRKL in endothelial cells and breast cancer cells. While only a small percentage of endothelial cells were positive for surface CRKL, incubation with cancer cell CM, increased the surface localization of CRKL. We also showed that CRKL is secreted from tumor cells into the cell culture supernatant. Thus, the enhanced CRKL in CM treated endothelial cells could be the soluble CRKL secreted by cancer cells. Further, *in vivo* allografts showed colocalization of CRKL in endothelial cells, suggesting that CRKL in these endothelial cells can act as a target for nanovectors. We also detected an increased surface-bound fraction of CRKL in various breast cancer cell lines when compared to non-cancerous epithelial cell lines. Immunofluorescence staining of breast cancer cell lines revealed CRKL on both the cell surface as well as in the intracellular compartments.

In accordance with *in vitro* studies, CRKL was over-expressed in tumor sections (Figure 11). Although immunohistochemical staining is not specific for surface-bound CRKL, it is in agreement with previously published data that CRKL is over-expressed in various tumor models, including gastric carcinomas [95], head and neck squamous cell carcinomas [146] and lung carcinomas [97]. Recent work by Zhao et al has shown that CRKL is over-expressed in 37% of breast cancer samples studied and was correlated with progression and malignant proliferation [100]. Our results provide further evidence that tissue expression of CRKL can serve as a potential tissue biomarker for breast tumors. **Moreover, we anticipate that in addition to the use of CRKL as a molecular target, membranal presence of the protein on the surface of endothelial and tumor cells can**

serve as selective target to direct nanoparticle based therapeutics and diagnostics to the tumor.

Thus, we used extracellular CRKL targeted, genetically engineered bacteriophage expressing a peptide sequence, YRCTLNSPFFWEDMTHECHA, homologous to the plexin-semaphorin integrin domain of β1 integrins in the formation of BASP. This phage has been shown to be as effective at targeting prostate tumor cells as the more commonly used RGD peptide [92]. Here we tested the efficiency of CRKL targeted phage to bind endothelial cells. CRKL targeted BASP were compared to S1MP and fd-tet non-targeted BASP. Our data showed that there was no significant differences in the association of CRKL targeted BASP to endothelial cells when compared to the other two particle types *in vitro* under static conditions. This is in correlation with data previous published on endothelial cells [115]. Endothelial cells act like professional phagocytes and uptake nanoparticles non-specifically. We also tested the efficiency of uptake of CRKL targeted BASP in breast cancer cell line, MCF7, that has a significant amount of CRKL on its surface. In this case, we could see a significant enhancement in the association/uptake of CRKL targeted BASP through specific, probably receptor mediated, interactions with the epithelial cell line as evidenced by the presence of BASP inside a vesicle when internalized (Figure 26C).

In contrast to targeting experiments under static conditions, our results from experiments conducted under shear stresses, capitulate better the observed behavior *in vivo*. For example, we saw that the number of CRKL targeted BASP associated with endothelial cells under low shear stress, such as that seen in tumor microcirculation, was twice as much as non-targeted fd-tet BASP or S1MP. This is due to the formation of strong interactions between CRKL on the surface of endothelial cells and the peptide expressed on

bacteriophage coat proteins. In the case of S1MP and fd-tet BASP, although they probably experience similar hemodynamic flow conditions, they do not form strong bonds by means of receptor-ligand interactions. Thus, the hemodynamic forces dislodge the particles before they can form a firm bond with the endothelial cells. As a result, more CRKL targeted BASP remain adhered to the cells than non-targeted particles. On the contrary, at higher shear rates of $100s^{-1}$(healthy microvasculature) the forces are much higher and thus the likelihood of particle adhesion is reduced. At these shear rates, the presence of targeting moieties on the particle surface did not make a significant difference in the binding of particles to endothelial cells, thereby suggesting that addition of targeting moiety onto the S1MP enhances the binding of particles to only tumor microvasculature and not to healthy microvasculature.

When evaluating the systems *in vivo,* we observed that the changes were significantly enhanced when compared to *in vitro* conditions. For example, the number of CRKL targeted BASP bound to the tumor in *in vivo* allografts was 4-fold higher than non-targeted particles. Also, the speeds of particles were orders of magnitude different for each case. The CRKL targeted particles travelled at speeds of about 10µm/s, while the fd-tet BASP were about 100µm/s and the S1MP were the fastest at about 600µm/s. This apparent difference between the *in vitro* and *in vivo* studies could be attributed to the differences in conditions. For example, *in vivo* flow involves not only specific shear rates, as is considered in *in vitro* studies, but also has very tortuous vasculature and whole blood containing multicellular components, all of which can affect the hemodynamics of blood flow.

Finally, we evaluated if this targeted system could efficiently carry therapeutics to the tumor site. For this, we injected tumor bearing mice with Abraxane loaded BASP and

compared their effect to either Abraxane itself or Abraxane loaded S1MP. We found that the targeting of the BASP significantly enhanced their therapeutic efficiency.

CRKL as a serum biomarker

In breast tumors, the majority of clinically used biomarkers are proteins over-expressed in tissue, which can be detected histologically in specimens from biopsies or following tumor resection. Their expression prescribes various treatment settings and is correlated to disease prognosis [147], particularly in the early disease stages. One of such biomarkers, c-erbB2, led to the discovery of trastuzumab [148]. However, the necessitation of invasive biopsies is a drawback that may be addressed by the detection of soluble biomarkers in body fluids. Overexpressed and secreted proteins from cancer cells, detected in the sera of cancer patients, are easy to collect and have been used clinically as diagnostic and prognostic markers for cancers [149]. A few examples of secreted proteins used for cancer diagnosis include prostate specific antigen for prostate cancer [150], carcinoembryonic antigen CA125 for ovarian cancer [151] and cytokine colony stimulating factor-1 (CSF-1) [152] for endometrial carcinoma. A few soluble biomarkers for breast cancers include CA 15.3 and CA 27.59 and vascular endothelial growth factor (VEGF) which have shown to be of prognostic value and are being evaluated in conjunction with diagnostic imaging to monitor metastatic diseases during the course of therapy [147].

In this study, we propose that CRKL, generally considered as an intracellular protein, can serve as a soluble biomarker for breast tumors. It is generally agreed that intracellular signaling of CRKL is involved in tumor progression of various tumor types, however, the role of soluble (secreted) fraction of CRKL have not been explored. For this purpose, we analyzed *in vitro*, *in vivo* and clinical samples to evaluate if the soluble fractions of CRKL

can be detected in cell culture media and blood serum. Our results showing significantly higher levels of soluble CRKL in serum from breast tumor xenograft bearing mice and breast tumor patients to healthy donors, suggest the use of CRKL as a soluble biomarker. The most widely used clinical breast cancer biomarker, CA 15.3, serves as a prognostic marker, to monitor response of breast cancer to treatment or detect early relapse [153]. However, CA 15-3 is elevated in only 3% of patients with localized early stage cancer and upto 70% of patients with metastatic disease [154]. In our study, we found that 100% of patients with metastatic disease have elevated serum levels of CRKL. Thus, soluble CRKL might serve as a stronger biomarker for predicting metastasis. Further, among patients analyzed in this study, four had not undergone treatment and had mean values 1.6 fold higher than the rest of the patients (n=25) who were undergoing treatment. Albeit the small sample size, this clear trend with a p-value of 0.13, suggests that CRKL levels might also be useful in monitoring treatment of breast cancer and requires further evaluation in larger sample size or progressive clinical studies.

CONCLUSIONS AND FUTURE DIRECTIONS

In this study we report a strategy for non-covalent attachment of targeting entities to porous silicon particle surfaces, which enables independent control over the loading of actives into the porous structure of the particles and their targeting to elements in the tumor microenvironment. The attachment of AuNP-bacteriophage networks on the S1MP surface does not impair the loading capacity of naked S1MP. The resulting BASP are biodegradable in serum and maintain their integrity while injected intravenously. This shows that electrostatic interactions of components in the system are stable under constant motion as

well as *in vivo*. We demonstrated that extracellular CRKL (traditionally thought of to be an intracellular protein) served as a very good target for efficient tumor directed accumulation of BASP and subsequently improved therapeutic effect on breast cancer allograft models.

We have also revealed that high levels of secreted CRKL can be detected in the plasma of breast tumor bearing mice and breast cancer patients. To the best of our knowledge, this is the first report about the possibility to detect soluble fractions of CRKL in body fluids from cancer patients. The results of our study suggest that CRKL can be used as a soluble serum biomarker in breast cancer patients especially in the advanced disease stages.

The BASP has more applications that haven't been studied to its full potential, for example, the applications related to the optical properties of AuNP in BASP, such as NIR-SERS imaging and detection *in vivo* and thermal ablation of tumors using NIR lasers. These BASP also present multiple opportunities for future research and improvement. The bacteriophage in BASP can be easily replaced with bacteriophage displaying any other targeting peptide of choice. Based on the targeting moieties chosen, BASP can also be evaluated for use in inflammatory conditions and cardiovascular diseases. Further, the S2NP can themselves be decorated with a targeting moiety or other surface decorations that can be used to overcome additional barriers, such as facilitation of lysosomal escape or subcellular organelle targeting, thereby providing a "two-fold" targeting of the nanovector, i.e. tumor targeting by the S1MP and cellular targeting by the S2NP.

REFERENCES

[1]C.f.D.C.a. Prevention, Breast Cancer Statistics, in, 2013.

[2]A.J. Redig, S.S. McAllister, Breast cancer as a systemic disease: a view of metastasis. Journal of Internal Medicine 274 (2013) 113-126.

[3]A.C. Society, How is breast cancer treated?, in, 2014.

[4]A.T. Perez, G.H. Domenech, C. Frankel, C.L. Vogel, Pegylated liposomal doxorubicin (Doxil) for metastatic breast cancer: the Cancer Research Network, Inc., experience. Cancer Invest 20 Suppl 2 (2002) 22-29.

[5]M. Harries, P. Ellis, P. Harper, Nanoparticle albumin-bound paclitaxel for metastatic breast cancer. J Clin Oncol 23 (2005) 7768-7771.

[6]E.H. Romond, E.A. Perez, J. Bryant, V.J. Suman, C.E. Geyer, Jr., N.E. Davidson, E. Tan-Chiu, S. Martino, S. Paik, P.A. Kaufman, S.M. Swain, T.M. Pisansky, L. Fehrenbacher, L.A. Kutteh, V.G. Vogel, D.W. Visscher, G. Yothers, R.B. Jenkins, A.M. Brown, S.R. Dakhil, E.P. Mamounas, W.L. Lingle, P.M. Klein, J.N. Ingle, N. Wolmark, Trastuzumab plus adjuvant chemotherapy for operable HER2-positive breast cancer. N Engl J Med 353 (2005) 1673-1684.

[7]D. Bilancia, G. Rosati, A. Dinota, D. Germano, R. Romano, L. Manzione, Lapatinib in breast cancer. Ann Oncol 18 Suppl 6 (2007) vi26-30.

[8]U.K. Marelli, F. Rechenmacher, T.R. Sobahi, C. Mas-Moruno, H. Kessler, Tumor Targeting via Integrin Ligands. Front Oncol 3 (2013) 222.

[9]H.B. Frieboes, Yokoi, K., Dave, B., Hussain, F., Godin, B., Modeling the tumor microenvironment as a biobarrier in cancer nanotherapeutics, in: R.E. Serda, (Ed.), Mass Transport of Nanocarriers, Pan Stanford, 2012, pp. 139 -183.

[10]M. Ferrari, Cancer nanotechnology: opportunities and challenges. Nat Rev Cancer 5 (2005) 161-171.

[11]W.H. De Jong, P.J. Borm, Drug delivery and nanoparticles:applications and hazards. Int J Nanomedicine 3 (2008) 133-149.

[12]J.H. Sakamoto, A.L. van de Ven, B. Godin, E. Blanco, R.E. Serda, A. Grattoni, A. Ziemys, A. Bouamrani, T. Hu, S.I. Ranganathan, E. De Rosa, J.O. Martinez, C.A. Smid, R.M. Buchanan, S.Y. Lee, S. Srinivasan, M. Landry, A. Meyn, E. Tasciotti, X. Liu, P. Decuzzi, M. Ferrari, Enabling individualized therapy through nanotechnology. Pharmacol Res 62 (2010) 57-89.

[13]B. Godin, W.H. Driessen, B. Proneth, S.Y. Lee, S. Srinivasan, R. Rumbaut, W. Arap, R. Pasqualini, M. Ferrari, P. Decuzzi, An integrated approach for the rational design of nanovectors for biomedical imaging and therapy. Adv Genet 69 (2010) 31-64.

[14]J.H. Lin, A.Y. Lu, Role of pharmacokinetics and metabolism in drug discovery and development. Pharmacol Rev 49 (1997) 403-449.

[15]A. Parkinson, B.W. Ogilvie, B.L. Paris, T.N. Hensley, G.J. Loewen, Human Biotransformation, in, Biotransformation and Metabolite Elucidation of Xenobiotics, John Wiley & Sons, Inc., 2010, pp. 1-77.

[16]H.S. Choi, W. Liu, P. Misra, E. Tanaka, J.P. Zimmer, B. Itty Ipe, M.G. Bawendi, J.V. Frangioni, Renal clearance of quantum dots. Nat Biotechnol 25 (2007) 1165-1170.

[17]S.D. Li, L. Huang, Pharmacokinetics and biodistribution of nanoparticles. Mol Pharm 5 (2008) 496-504.

[18]Z.J. Deng, S.W. Morton, E. Ben-Akiva, E.C. Dreaden, K.E. Shopsowitz, P.T. Hammond, Layer-by-Layer Nanoparticles for Systemic Codelivery of an Anticancer Drug and siRNA for Potential Triple-Negative Breast Cancer Treatment. ACS Nano (2013).

[19]G. Batist, K.A. Gelmon, K.N. Chi, W.H. Miller, Jr., S.K. Chia, L.D. Mayer, C.E. Swenson, A.S. Janoff, A.C. Louie, Safety, pharmacokinetics, and efficacy of CPX-1 liposome injection in patients with advanced solid tumors. Clin Cancer Res 15 (2009) 692-700.

[20]M. Ferrari, Nanovector therapeutics. Curr Opin Chem Biol 9 (2005) 343-346.

[21]J.O. Martinez, C. Chiappini, A. Ziemys, A.M. Faust, M. Kojic, X. Liu, M. Ferrari, E. Tasciotti, Engineering multi-stage nanovectors for controlled degradation and tunable release kinetics. Biomaterials 34 (2013) 8469-8477.

[22]J.M. Morachis, E.A. Mahmoud, J. Sankaranarayanan, A. Almutairi, Triggered rapid degradation of nanoparticles for gene delivery. J Drug Deliv 2012 (2012) 291219.

[23]K. Na, K.H. Lee, D.H. Lee, Y.H. Bae, Biodegradable thermo-sensitive nanoparticles from poly(L-lactic acid)/poly(ethylene glycol) alternating multi-block copolymer for potential anti-cancer drug carrier. Eur J Pharm Sci 27 (2006) 115-122.

[24]E. De Rosa, C. Chiappini, D. Fan, X. Liu, M. Ferrari, E. Tasciotti, Agarose surface coating influences intracellular accumulation and enhances payload stability of a nano-delivery system. Pharm Res 28 (2011) 1520-1530.

[25]C. Bergin, A. O'Leary, C. McCreary, K. Sabra, F. Mulcahy, Treatment of Kaposi's sarcoma with liposomal doxorubicin. Am J Health Syst Pharm 52 (1995) 2001-2004.

[26]C.H. Smorenburg, S.M. de Groot, A.E. van Leeuwen-Stok, M.E. Hamaker, A.N. Wymenga, H. de Graaf, F.E. de Jongh, J.J. Braun, M. Los, E. Maartense, H. van Tinteren, J.W. Nortier, C. Seynaeve, A randomized phase III study comparing pegylated liposomal doxorubicin with capecitabine as first-line chemotherapy in elderly patients with metastatic breast cancer: results of the OMEGA study of the Dutch Breast Cancer Research Group BOOG. Ann Oncol 25 (2014) 599-605.

[27]M.E.R. O'Brien, N. Wigler, M. Inbar, R. Rosso, E. Grischke, A. Santoro, R. Catane, D.G. Kieback, P. Tomczak, S.P. Ackland, F. Orlandi, L. Mellars, L. Alland, C. Tendler, Reduced cardiotoxicity and comparable efficacy in a phase III trial of pegylated liposomal doxorubicin HCl (CAELYX™/Doxil®) versus conventional doxorubicin for first-line treatment of metastatic breast cancer. Annals of Oncology 15 (2004) 440-449.

[28]A.N. Gordon, J.T. Fleagle, D. Guthrie, D.E. Parkin, M.E. Gore, A.J. Lacave, Recurrent epithelial ovarian carcinoma: a randomized phase III study of pegylated liposomal doxorubicin versus topotecan. J Clin Oncol 19 (2001) 3312-3322.

[29]F. Petrelli, K. Borgonovo, S. Barni, Targeted delivery for breast cancer therapy: the history of nanoparticle-albumin-bound paclitaxel. Expert Opin Pharmacother 11 (2010) 1413-1432.

[30]P. Ma, R.J. Mumper, Paclitaxel Nano-Delivery Systems: A Comprehensive Review. J Nanomed Nanotechnol 4 (2013) 1000164.

[31]T. Negishi, F. Koizumi, H. Uchino, J. Kuroda, T. Kawaguchi, S. Naito, Y. Matsumura, NK105, a paclitaxel-incorporating micellar nanoparticle, is a more potent radiosensitising agent compared to free paclitaxel. Br J Cancer 95 (2006) 601-606.

[32]W.J. Gradishar, S. Tjulandin, N. Davidson, H. Shaw, N. Desai, P. Bhar, M. Hawkins, J. O'Shaughnessy, Phase III trial of nanoparticle albumin-bound paclitaxel compared with polyethylated castor oil-based paclitaxel in women with breast cancer. J Clin Oncol 23 (2005) 7794-7803.

[33]R. Visaria, J.C. Bischof, M. Loren, B. Williams, E. Ebbini, G. Paciotti, R. Griffin, Nanotherapeutics for enhancing thermal therapy of cancer. Int J Hyperthermia 23 (2007) 501-511.

[34]D.B. Shenoy, M.M. Amiji, Poly(ethylene oxide)-modified poly(epsilon-caprolactone) nanoparticles for targeted delivery of tamoxifen in breast cancer. Int J Pharm 293 (2005) 261-270.

[35]D.H. Yan, L.S. Chang, M.C. Hung, Repressed expression of the HER-2/c-erbB-2 proto-oncogene by the adenovirus E1a gene products. Oncogene 6 (1991) 343-345.

[36]S. Prabha, V. Labhasetwar, Nanoparticle-mediated wild-type p53 gene delivery results in sustained antiproliferative activity in breast cancer cells. Mol Pharm 1 (2004) 211-219.

[37]B. Urban-Klein, S. Werth, S. Abuharbeid, F. Czubayko, A. Aigner, RNAi-mediated gene-targeting through systemic application of polyethylenimine (PEI)-complexed siRNA in vivo. Gene Ther 12 (2005) 461-466.

[38]K. Teker, Bioconjugated carbon nanotubes for targeting cancer biomarkers. Materials Science and Engineering: B 153 (2008) 83-87.

[39]Y. Chen, X. Wang, M.K. Hong, C.L. Rosenberg, B.M. Reinhard, S. Erramilli, P. Mohanty, Nanoelectronic detection of breast cancer biomarker. Applied Physics Letters 97 (2010) -.

[40]M.M. Yezhelyev, C; Gao, X; Nie, S; Lewis, M; Cohen, C; O'Regan, R.M., Multiplex molecular profiling of breast cancer cell lines with quantum dot-antibody conjugates, in, Proceedings of American Association for Cancer Research, Anaheim, California, 2005.

[41]K.K. Jain, Personalised medicine for cancer: from drug development into clinical practice. Expert Opin Pharmacother 6 (2005) 1463-1476.

[42]L. Zhang, D. Lv, W. Su, Y. Liu, Y. Chen, R. Xiang, Detection of cancer biomarkers with nanotechnology. Americal Journal of Biochemistry and Biotechnology 9 (2013) 71-89.

[43]O. Rabin, J. Manuel Perez, J. Grimm, G. Wojtkiewicz, R. Weissleder, An X-ray computed tomography imaging agent based on long-circulating bismuth sulphide nanoparticles. Nat Mater 5 (2006) 118-122.

[44]W.R. Sanhai, J.H. Sakamoto, R. Canady, M. Ferrari, Seven challenges for nanomedicine. Nat Nanotechnol 3 (2008) 242-244.

[45]F.M. Kievit, M. Zhang, Cancer nanotheranostics: improving imaging and therapy by targeted delivery across biological barriers. Adv Mater 23 (2011) H217-247.

[46]M. Ferrari, Frontiers in cancer nanomedicine: directing mass transport through biological barriers. Trends Biotechnol 28 (2010) 181-188.

[47]C. Khemtong, C.W. Kessinger, J. Ren, E.A. Bey, S.G. Yang, J.S. Guthi, D.A. Boothman, A.D. Sherry, J. Gao, In vivo off-resonance saturation magnetic resonance imaging of alphavbeta3-targeted superparamagnetic nanoparticles. Cancer Res 69 (2009) 1651-1658.

[48]R. Bardhan, W. Chen, M. Bartels, C. Perez-Torres, M.F. Botero, R.W. McAninch, A. Contreras, R. Schiff, R.G. Pautler, N.J. Halas, A. Joshi, Tracking of multimodal therapeutic nanocomplexes targeting breast cancer in vivo. Nano Lett 10 (2010) 4920-4928.

[49]R. Bardhan, W. Chen, C. Perez-Torres, M. Bartels, R.M. Huschka, L.L. Zhao, E. Morosan, R.G. Pautler, A. Joshi, N.J. Halas, Nanoshells with Targeted Simultaneous Enhancement of Magnetic and Optical Imaging and Photothermal Therapeutic Response. Advanced Functional Materials 19 (2009) 3901-3909.

[50]V. Bagalkot, L. Zhang, E. Levy-Nissenbaum, S. Jon, P.W. Kantoff, R. Langer, O.C. Farokhzad, Quantum dot-aptamer conjugates for synchronous cancer imaging, therapy, and sensing of drug delivery based on bi-fluorescence resonance energy transfer. Nano Lett 7 (2007) 3065-3070.

[51]J. Cheng, B.A. Teply, I. Sherifi, J. Sung, G. Luther, F.X. Gu, E. Levy-Nissenbaum, A.F. Radovic-Moreno, R. Langer, O.C. Farokhzad, Formulation of functionalized PLGA-PEG nanoparticles for in vivo targeted drug delivery. Biomaterials 28 (2007) 869-876.

[52]S.A. Kularatne, P.S. Low, Targeting of nanoparticles: folate receptor. Methods Mol Biol 624 (2010) 249-265.

[53]C.M. Lee, H.J. Jeong, E.M. Kim, D.W. Kim, S.T. Lim, H.T. Kim, I.K. Park, Y.Y. Jeong, J.W. Kim, M.H. Sohn, Superparamagnetic iron oxide nanoparticles as a dual imaging probe for targeting hepatocytes in vivo. Magn Reson Med 62 (2009) 1440-1446.

[54]O. Eniola-Adefeso, M.J. Heslinga, T.M. Porter, Design of nanovectors for therapy and imaging of cardiovascular diseases. Methodist Debakey Cardiovasc J 8 (2012) 13-17.

[55]M.D. Howard, M. Jay, T.D. Dziubla, X. Lu, PEGylation of Nanocarrier Drug Delivery Systems: State of the Art. Journal of Biomedical Nanotechnology 4 (2008) 133-148.

[56]L.E. van Vlerken, T.K. Vyas, M.M. Amiji, Poly(ethylene glycol)-modified nanocarriers for tumor-targeted and intracellular delivery. Pharm Res 24 (2007) 1405-1414.

[57]S.K. Hobbs, W.L. Monsky, F. Yuan, W.G. Roberts, L. Griffith, V.P. Torchilin, R.K. Jain, Regulation of transport pathways in tumor vessels: Role of tumor type and microenvironment. Proceedings of the National Academy of Sciences 95 (1998) 4607-4612.

[58]S.K. Hobbs, W.L. Monsky, F. Yuan, W.G. Roberts, L. Griffith, V.P. Torchilin, R.K. Jain, Regulation of transport pathways in tumor vessels: role of tumor type and microenvironment. Proc Natl Acad Sci U S A 95 (1998) 4607-4612.

[59]E. Tasciotti, X. Liu, R. Bhavane, K. Plant, A.D. Leonard, B.K. Price, M.M. Cheng, P. Decuzzi, J.M. Tour, F. Robertson, M. Ferrari, Mesoporous Silicon Particles as a Multistage Delivery System for Imaging and Therapeutic Applications. Nat Nanotechnol 3 (2008) 151-157.

[60]P. Decuzzi, R. Pasqualini, W. Arap, M. Ferrari, Intravascular delivery of particulate systems: does geometry really matter? Pharm Res 26 (2009) 235-243.

[61]A.J. Goldman, R.G. Cox, H. Brenner, Slow viscous motion of a sphere parallel to a plane wall—II Couette flow. Chemical Engineering Science 22 (1967) 653-660.

[62]B. Godin, J. Gu, R.E. Serda, R. Bhavane, E. Tasciotti, C. Chiappini, X. Liu, T. Tanaka, P. Decuzzi, M. Ferrari, Tailoring the degradation kinetics of mesoporous silicon structures through PEGylation. J Biomed Mater Res A 94 (2010) 1236-1243.

[63]E. Tasciotti, B. Godin, J.O. Martinez, C. Chiappini, R. Bhavane, X. Liu, M. Ferrari, Near-Infrared Imaging Method for the *In Vivo A*ssessment of the Biodistribution of Nanoporous Silicon Particles. Mol Imaging 10 (2011) 56-68.

[64]L.M. Bimbo, M. Sarparanta, H.A. Santos, A.J. Airaksinen, E. Mäkilä, T. Laaksonen, L. Peltonen, V.-P. Lehto, J. Hirvonen, J. Salonen, Biocompatibility of Thermally Hydrocarbonized Porous Silicon Nanoparticles and their Biodistribution in Rats. ACS Nano 4 (2010) 3023-3032.

[65]H.A. Santos, J. Hirvonen, Nanostructured porous silicon materials: potential candidates for improving drug delivery. Nanomedicine (Lond) 7 (2012) 1281-1284.

[66]H.A. Santos, L.M. Bimbo, B. Herranz, M.-A. Shahbazi, J. Hirvonen, J. Salonen, Nanostructured porous silicon in preclinical imaging: Moving from bench to bedside. Journal of Materials Research FirstView (2012) 1-13.

[67]S.P. Low, N.H. Voelcker, L.T. Canham, K.A. Williams, The biocompatibility of porous silicon in tissues of the eye. Biomaterials 30 (2009) 2873-2880.

[68]J.H. Park, L. Gu, G. von Maltzahn, E. Ruoslahti, S.N. Bhatia, M.J. Sailor, Biodegradable luminescent porous silicon nanoparticles for in vivo applications. Nat Mater 8 (2009) 331-336.

[69]C. Chiappini, E. Tasciotti, J.R. Fakhoury, D. Fine, L. Pullan, Y.C. Wang, L. Fu, X. Liu, M. Ferrari, Tailored porous silicon microparticles: fabrication and properties. Chemphyschem 11 (2010) 1029-1035.

[70]P. Decuzzi, B. Godin, T. Tanaka, S.Y. Lee, C. Chiappini, X. Liu, M. Ferrari, Size and shape effects in the biodistribution of intravascularly injected particles. J Control Release 141 (2010) 320-327.

[71]B. Godin, C. Chiappini, S. Srinivasan, J.F. Alexander, K. Yokoi, M. Ferrari, P. Decuzzi, X. Liu, Discoidal Porous Silicon Particles: Fabrication and Biodistribution in Breast Cancer Bearing Mice. Advanced Functional Materials 22 (2012) 4225-4235.

[72]B. Godin, E. Tasciotti, X. Liu, R.E. Serda, M. Ferrari, Multistage nanovectors: from concept to novel imaging contrast agents and therapeutics. Accounts of Chemical Research 44 (2011) 979-989.

[73]K. Yokoi, B. Godin, C.J. Oborn, J.F. Alexander, X. Liu, I.J. Fidler, M. Ferrari, Porous silicon nanocarriers for dual targeting tumor associated endothelial cells and macrophages in stroma of orthotopic human pancreatic cancers. Cancer Lett (2012).

[74]A.L. van de Ven, P. Kim, O. Haley, J.R. Fakhoury, G. Adriani, J. Schmulen, P. Moloney, F. Hussain, M. Ferrari, X. Liu, S.H. Yun, P. Decuzzi, Rapid tumoritropic accumulation of systemically injected plateloid particles and their biodistribution. J Control Release 158 (2012) 148-155.

[75]A.P. Mann, T. Tanaka, A. Somasunderam, X. Liu, D.G. Gorenstein, M. Ferrari, E-Selectin-Targeted Porous Silicon Particle for Nanoparticle Delivery to the Bone Marrow. Advanced Materials 23 (2011) H278-H282.

[76]A. Parodi, N. Quattrocchi, A.L. van de Ven, C. Chiappini, M. Evangelopoulos, J.O. Martinez, B.S. Brown, S.Z. Khaled, I.K. Yazdi, M.V. Enzo, L. Isenhart, M. Ferrari, E. Tasciotti, Synthetic nanoparticles functionalized with biomimetic leukocyte membranes possess cell-like functions. Nat Nanotechnol 8 (2013) 61-68.

[77]T. Tanaka, L.S. Mangala, P.E. Vivas-Mejia, R. Nieves-Alicea, A.P. Mann, E. Mora, H.D. Han, M.M. Shahzad, X. Liu, R. Bhavane, et-al, Sustained Small Interfering RNA Delivery by Mesoporous Silicon Particles. Cancer Res 70 (2010) 3687-3696.

[78]R.E. Serda, A. Mack, M. Pulikkathara, A.M. Zaske, C. Chiappini, J.R. Fakhoury, D. Webb, B. Godin, J.L. Conyers, X.W. Liu, J.A. Bankson, M. Ferrari, Cellular association and assembly of a multistage delivery system. Small 6 (2010) 1329-1340.

[79]E. Blanco, T. Sangai, A. Hsiao, S. Ferrati, L. Bai, X. Liu, F. Meric-Bernstam, M. Ferrari, Multistage delivery of chemotherapeutic nanoparticles for breast cancer treatment. Cancer Lett 334 (2013) 245-252.

[80]J.S. Ananta, B. Godin, R. Sethi, L. Moriggi, X. Liu, R.E. Serda, R. Krishnamurthy, R. Muthupillai, R.D. Bolskar, L. Helm, et-al, Geometrical Confinement of Gadolinium-Based Contrast Agents in Nanoporous Particles Enhances T1 contrast. Nat Nanotechnol 5 (2010) 815-821.

[81]H. Shen, J. You, G. Zhang, A. Ziemys, Q. Li, L. Bai, X. Deng, D.R. Erm, X. Liu, C. Li, M. Ferrari, Cooperative, nanoparticle-enabled thermal therapy of breast cancer. Adv Healthc Mater 1 (2012) 84-89.

[82]L. Chen, A.J. Zurita, P.U. Ardelt, R.J. Giordano, W. Arap, R. Pasqualini, Design and validation of a bifunctional ligand display system for receptor targeting. Chem Biol 11 (2004) 1081-1091.

[83]S. Srinivasan, J.F. Alexander, W.H. Driessen, F. Leonard, H. Ye, X. Liu, W. Arap, R. Pasqualini, M. Ferrari, B. Godin, Bacteriophage associated silicon particles: design and characterization of a novel theranostic vector with improved payload carrying potential. Journal of Materials Chemistry B 1 (2013) 5218-5229.

[84]A.P. Mann, T. Tanaka, A. Somasunderam, X. Liu, D.G. Gorenstein, M. Ferrari, E-selectin-targeted porous silicon particle for nanoparticle delivery to the bone marrow. Adv Mater 23 (2011) H278-282.

[85]N. Gandra, G. Abbineni, X. Qu, Y. Huai, L. Wang, C. Mao, Bacteriophage bionanowire as a carrier for both cancer-targeting peptides and photosensitizers and its use in selective cancer cell killing by photodynamic therapy. Small 9 (2013) 215-221.

[86]G.P. Smith, V.A. Petrenko, Phage Display. Chem Rev 97 (1997) 391-410.

[87]M. Murugesan, G. Abbineni, S.L. Nimmo, B. Cao, C. Mao, Virus-based photo-responsive nanowires formed by linking site-directed mutagenesis and chemical reaction. Sci Rep 3 (2013) 1820.

[88]W. Arap, W. Haedicke, M. Bernasconi, R. Kain, D. Rajotte, S. Krajewski, H.M. Ellerby, D.E. Bredesen, R. Pasqualini, E. Ruoslahti, Targeting the prostate for destruction through a vascular address. Proceedings of the National Academy of Sciences 99 (2002) 1527-1531.

[89]S.A. Nicklin, S.J. White, S.J. Watkins, R.E. Hawkins, A.H. Baker, Selective targeting of gene transfer to vascular endothelial cells by use of peptides isolated by phage display. Circulation 102 (2000) 231-237.

[90]M.A. Burg, R. Pasqualini, W. Arap, E. Ruoslahti, W.B. Stallcup, NG2 proteoglycan-binding peptides target tumor neovasculature. Cancer Res 59 (1999) 2869-2874.

[91]M. Allinen, R. Beroukhim, L. Cai, C. Brennan, J. Lahti-Domenici, H. Huang, D. Porter, M. Hu, L. Chin, A. Richardson, S. Schnitt, W.R. Sellers, K. Polyak, Molecular characterization of the tumor microenvironment in breast cancer. Cancer Cell 6 (2004) 17-32.

[92]P.J. Mintz, M. Cardo-Vila, M.G. Ozawa, A. Hajitou, R. Rangel, L. Guzman-Rojas, D.R. Christianson, M.A. Arap, R.J. Giordano, G.R. Souza, J. Easley, A. Salameh, S. Oliviero, R.R. Brentani, E. Koivunen, W. Arap, R. Pasqualini, An unrecognized

extracellular function for an intracellular adapter protein released from the cytoplasm into the tumor microenvironment. Proc Natl Acad Sci U S A 106 (2009) 2182-2187.

[93]J. ten Hoeve, C. Morris, N. Heisterkamp, J. Groffen, Isolation and chromosomal localization of CRKL, a human crk-like gene. Oncogene 8 (1993) 2469-2474.

[94]R.B. Birge, C. Kalodimos, F. Inagaki, S. Tanaka, Crk and CrkL adaptor proteins: networks for physiological and pathological signaling. Cell Commun Signal 7 (2009) 13.

[95]H. Natsume, K. Shinmura, H. Tao, H. Igarashi, M. Suzuki, K. Nagura, M. Goto, H. Yamada, M. Maeda, H. Konno, S. Nakamura, H. Sugimura, The CRKL gene encoding an adaptor protein is amplified, overexpressed, and a possible therapeutic target in gastric cancer. J Transl Med 10 (2012) 97.

[96]H.W. Cheung, J. Du, J.S. Boehm, F. He, B.A. Weir, X. Wang, M. Butaney, L.V. Sequist, B. Luo, J.A. Engelman, D.E. Root, M. Meyerson, T.R. Golub, P.A. Janne, W.C. Hahn, Amplification of CRKL induces transformation and epidermal growth factor receptor inhibitor resistance in human non-small cell lung cancers. Cancer Discov 1 (2011) 608-625.

[97]Y. Wang, Q.Z. Dong, L. Fu, M. Stoecker, E. Wang, E.H. Wang, Overexpression of CRKL correlates with poor prognosis and cell proliferation in non-small cell lung cancer. Mol Carcinog (2012) 1-10.

[98]C.H. Liu, T.C. Chen, G.Y. Chau, Y.H. Jan, C.H. Chen, C.N. Hsu, K.T. Lin, Y.L. Juang, P.J. Lu, H.C. Cheng, M.H. Chen, C.F. Chang, Y.S. Ting, C.Y. Kao, M. Hsiao, C.Y. Huang, Analysis of protein-protein interactions in cross-talk pathways reveals CRKL

protein as a novel prognostic marker in hepatocellular carcinoma. Mol Cell Proteomics 12 (2013) 1335-1349.

[99]K.E. Fathers, E.S. Bell, C.V. Rajadurai, S. Cory, H. Zhao, A. Mourskaia, D. Zuo, J. Madore, A. Monast, A.M. Mes-Masson, A.A. Grosset, L. Gaboury, M. Hallet, P. Siegel, M. Park, Crk adaptor proteins act as key signaling integrators for breast tumorigenesis. Breast Cancer Res 14 (2012) R74.

[100]T. Zhao, Z. Miao, Z. Wang, Y. Xu, J. Wu, X. Liu, Y. You, J. Li, Overexpression of CRKL correlates with malignant cell proliferation in breast cancer. Tumour Biol 34 (2013) 2891-2897.

[101]E.J. Arnoys, J.L. Wang, Dual localization: proteins in extracellular and intracellular compartments. Acta Histochem 109 (2007) 89-110.

[102]E.N. Fish, S. Uddin, M. Korkmaz, B. Majchrzak, B.J. Druker, L.C. Platanias, Activation of a CrkL-stat5 signaling complex by type I interferons. J Biol Chem 274 (1999) 571-573.

[103]M.G. Ozawa, M. Cardo-Vila, P.J. Mintz, W. Arap, R. Pasqualini, Cracking the code for compartment-specific dual functionality proteins in cancer: the case for CRKL. Cell Cycle 9 (2010) 8-9.

[104]N. Uemura, R. Salgia, D.S. Ewaniuk, M.T. Little, J.D. Griffin, Involvement of the adapter protein CRKL in integrin-mediated adhesion. Oncogene 18 (1999) 3343-3353.

[105]G.R. Souza, D.R. Christianson, F.I. Staquicini, M.G. Ozawa, E.Y. Snyder, R.L. Sidman, J.H. Miller, W. Arap, R. Pasqualini, Networks of gold nanoparticles and

bacteriophage as biological sensors and cell-targeting agents. Proc Natl Acad Sci U S A 103 (2006) 1215-1220.

[106]H. Zhu, B. Cao, Z. Zhen, A.A. Laxmi, D. Li, S. Liu, C. Mao, Controlled growth and differentiation of MSCs on grooved films assembled from monodisperse biological nanofibers with genetically tunable surface chemistries. Biomaterials 32 (2011) 4744-4752.

[107]W. Arap, R. Pasqualini, E. Ruoslahti, Cancer treatment by targeted drug delivery to tumor vasculature in a mouse model. Science 279 (1998) 377-380.

[108]G.R. Souza, E. Yonel-Gumruk, D. Fan, J. Easley, R. Rangel, L. Guzman-Rojas, J.H. Miller, W. Arap, R. Pasqualini, Bottom-up assembly of hydrogels from bacteriophage and Au nanoparticles: the effect of cis- and trans-acting factors. PLoS One 3 (2008) e2242.

[109]G.R. Souza, C.S. Levin, A. Hajitou, R. Pasqualini, W. Arap, J.H. Miller, In vivo detection of gold-imidazole self-assembly complexes: NIR-SERS signal reporters. Anal Chem 78 (2006) 6232-6237.

[110]A. Hajitou, N.E. Sounni, L. Devy, C. Grignet-Debrus, J.M. Lewalle, H. Li, C.F. Deroanne, H. Lu, A. Colige, B.V. Nusgens, F. Frankenne, A. Maron, P. Yeh, M. Perricaudet, Y. Chang, C. Soria, C.M. Calberg-Bacq, J.M. Foidart, A. Noel, Down-regulation of vascular endothelial growth factor by tissue inhibitor of metalloproteinase-2: effect on in vivo mammary tumor growth and angiogenesis. Cancer Res 61 (2001) 3450-3457.

[111]D.A. Handley, Colloidal Gold: Principles, Methods and Applications, in: M.A. Hayat, (Ed.), Colloidal Gold: Principles, Methods and Applications, Academic Press, 1989, pp. 23-27.

[112]D.R. Christianson, M.G. Ozawa, R. Pasqualini, W. Arap, Techniques to decipher molecular diversity by phage display. Methods Mol Biol 357 (2007) 385-406.

[113]C.F. Barbas III, Burton D.R., Scott J.K., Silverman G.J., Phage Display, A Laboratory Manual. (2001).

[114]Y. Aida, M.J. Pabst, Removal of endotoxin from protein solutions by phase separation using Triton X-114. J Immunol Methods 132 (1990) 191-195.

[115]R.E. Serda, J. Gu, R.C. Bhavane, X. Liu, C. Chiappini, P. Decuzzi, M. Ferrari, The association of silicon microparticles with endothelial cells in drug delivery to the vasculature. Biomaterials 30 (2009) 2440-2448.

[116]J.M. Harris, N.E. Martin, M. Modi, Pegylation: a novel process for modifying pharmacokinetics. Clin Pharmacokinet 40 (2001) 539-551.

[117]D. Garfinkel, J.T. Edsall, Raman Spectra of Amino Acids and Related Compounds. XI. The Ionization of Cysteine1-3. Journal of the American Chemical Society 80 (1958) 3823-3826.

[118]R.W. Williams, A.K. Dunker, W.L. Peticolas, Raman spectroscopy and deuterium exchange of the filamentous phage fd. Biochim Biophys Acta 791 (1984) 131-144.

[119]K.L. Aubrey, G.J. Thomas, Jr., Raman Spectroscopy of Filamentous Bacteriophage Ff (fd, M13, f1) Incorporating Specifically-Deuterated Alanine and Tryptophan Side Chains. Assignments and Structural Interpretation. Biophys J 60 (1991) 1337-1349.

[120]B. Godin, E. Tasciotti, X. Liu, R.E. Serda, M. Ferrari, Multistage Nanovectors: From Concept to Novel Imaging Contrast Agents and Therapeutics. Acc Chem Res (2011).

[121]V.H. Chu, N. T.H.L., L. T.H., T.D.T. Ung, Q.H. Le, K.T. Tong, Q.L. Nguyen, H.N. Tran, Attaching quantum dots to HER2 specific phage antibodies. Advances in Natural Sciences: Nanoscience and Nanotechnology 1 (2010).

[122]R.E. Serda, A. Mack, M. Pulikkathara, A.M. Zaske, C. Chiappini, J.R. Fakhoury, D. Webb, B. Godin, J.L. Conyers, X.W. Liu, J.A. Bankson, M. Ferrari, Cellular association and assembly of a multistage delivery system. Small 6 1329-1340.

[123]S. Dwivedi, D. Pandey, A.L. Khandoga, R. Brandl, W. Siess, Rac1-mediated signaling plays a central role in secretion-dependent platelet aggregation in human blood stimulated by atherosclerotic plaque. J Transl Med 8 (2010) 128.

[124]H.B. Frieboes, M. Wu, J. Lowengrub, P. Decuzzi, V. Cristini, A computational model for predicting nanoparticle accumulation in tumor vasculature. PLoS One 8 (2013) e56876.

[125]R.K. Jain, T. Stylianopoulos, Delivering nanomedicine to solid tumors. Nat Rev Clin Oncol 7 (2010) 653-664.

[126]S.M. Moghimi, D. Peer, R. Langer, Reshaping the future of nanopharmaceuticals: ad iudicium. ACS Nano 5 (2011) 8454-8458.

[127]S.Y. Lee, M. Ferrari, P. Decuzzi, Design of bio-mimetic particles with enhanced vascular interaction. J Biomech 42 (2009) 1885-1890.

[128]M. Ferrari, Nanogeometry: Beyond Drug Delivery. Nat Nanotechnol 3 (2008) 131-132.

[129]J.A. Champion, Y.K. Katare, S. Mitragotri, Particle shape: a new design parameter for micro- and nanoscale drug delivery carriers. J Control Release 121 (2007) 3-9.

[130]G. Adriani, M.D. de Tullio, M. Ferrari, F. Hussain, G. Pascazio, X. Liu, P. Decuzzi, The preferential targeting of the diseased microvasculature by disk-like particles. Biomaterials 33 (2012) 5504-5513.

[131]M. Gaumet, A. Vargas, R. Gurny, F. Delie, Nanoparticles for drug delivery: the need for precision in reporting particle size parameters. Eur J Pharm Biopharm 69 (2008) 1-9.

[132]M. Ferrari, Nanogeometry: Beyond drug delivery. Nat Nano 3 (2008) 131-132.

[133]F.R. Kersey, T.J. Merkel, J.L. Perry, M.E. Napier, J.M. DeSimone, Effect of aspect ratio and deformability on nanoparticle extravasation through nanopores. Langmuir 28 (2012) 8773-8781.

[134]J.W. Yoo, E. Chambers, S. Mitragotri, Factors that control the circulation time of nanoparticles in blood: challenges, solutions and future prospects. Curr Pharm Des 16 (2010) 2298-2307.

[135]K. Lind, M. Kresse, R.H. Muller, Comparison of protein adsorption patterns onto differently charged hydrophilic superparamagnetic iron oxide particles obtained in vitro and ex vivo. Electrophoresis 22 (2001) 3514-3521.

[136]O. Garbuzenko, S. Zalipsky, M. Qazen, Y. Barenholz, Electrostatics of PEGylated micelles and liposomes containing charged and neutral lipopolymers. Langmuir 21 (2005) 2560-2568.

[137]D.A. Christian, O.B. Garbuzenko, T. Minko, D.E. Discher, Polymer Vesicles with a Red Cell-like Surface Charge: Microvascular Imaging and in vivo Tracking with Near-Infrared Fluorescence. Macromol Rapid Commun 31 (2010) 135-141.

[138]T.J. Merkel, S.W. Jones, K.P. Herlihy, F.R. Kersey, A.R. Shields, M. Napier, J.C. Luft, H. Wu, W.C. Zamboni, A.Z. Wang, J.E. Bear, J.M. DeSimone, Using mechanobiological mimicry of red blood cells to extend circulation times of hydrogel microparticles. Proc Natl Acad Sci U S A 108 (2011) 586-591.

[139]R. Gaspar, Nanoparticles: Pushed off target with proteins. Nat Nano 8 (2013) 79-80.

[140]D. Peer, J.M. Karp, S. Hong, O.C. Farokhzad, R. Margalit, R. Langer, Nanocarriers as an emerging platform for cancer therapy. Nat Nanotechnol 2 (2007) 751-760.

[141]R. Cademartiri, H. Anany, I. Gross, R. Bhayani, M. Griffiths, M.A. Brook, Immobilization of Bacteriophages on Modified Silica Particles. Biomaterials 31 (2010) 1904-1910.

[142]J. Zong, Y. Zhu, X. Yang, C. Li, Preparation of monodispersed mesoporous silica spheres with tunable pore size and pore-size effects on adsorption of Au nanoparticles and urease. Materials Science and Engineering: C In Press, Corrected Proof.

[143]A. Verma, F. Stellacci, Effect of surface properties on nanoparticle-cell interactions. Small 6 (2010) 12-21.

[144]R. Weissleder, A clearer vision for in vivo imaging. Nat Biotechnol 19 (2001) 316-317.

[145]A.M. Gobin, M.H. Lee, N.J. Halas, W.D. James, R.A. Drezek, J.L. West, Near-infrared Resonant Nanoshells for Combined Optical Imaging and Photothermal Cancer Therapy. Nano Lett 7 (2007) 1929-1934.

[146]H. Yanagi, L. Wang, H. Nishihara, T. Kimura, M. Tanino, T. Yanagi, S. Fukuda, S. Tanaka, CRKL plays a pivotal role in tumorigenesis of head and neck squamous cell carcinoma through the regulation of cell adhesion. Biochem Biophys Res Commun 418 (2012) 104-109.

[147]L. Harris, H. Fritsche, R. Mennel, L. Norton, P. Ravdin, S. Taube, M.R. Somerfield, D.F. Hayes, R.C. Bast, Jr., American Society of Clinical Oncology 2007 update of recommendations for the use of tumor markers in breast cancer. J Clin Oncol 25 (2007) 5287-5312.

[148]S. Verma, S. Lavasani, J. Mackey, K. Pritchard, M. Clemons, S. Dent, J. Latreille, J. Lemieux, L. Provencher, S. Verma, S. Chia, B. Wang, D. Rayson, Optimizing the management of HER2-positive early breast cancer: the clinical reality. Curr Oncol 17 (2010) 20-33.

[149]C.C. Wu, K.Y. Chien, N.M. Tsang, K.P. Chang, S.P. Hao, C.H. Tsao, Y.S. Chang, J.S. Yu, Cancer cell-secreted proteomes as a basis for searching potential tumor markers: nasopharyngeal carcinoma as a model. Proteomics 5 (2005) 3173-3182.

[150]S.P. Balk, Y.J. Ko, G.J. Bubley, Biology of prostate-specific antigen. J Clin Oncol 21 (2003) 383-391.

[151]A. Raamanathan, G.W. Simmons, N. Christodoulides, P.N. Floriano, W.B. Furmaga, S.W. Redding, K.H. Lu, R.C. Bast, Jr., J.T. McDevitt, Programmable bio-nano-chip systems for serum CA125 quantification: toward ovarian cancer diagnostics at the point-of-care. Cancer Prev Res (Phila) 5 (2012) 706-716.

[152]B.M. Kacinski, S.K. Chambers, E.R. Stanley, D. Carter, P. Tseng, K.A. Scata, D.H. Chang, M.H. Pirro, J.T. Nguyen, A. Ariza, et al., The cytokine CSF-1 (M-CSF) expressed by endometrial carcinomas in vivo and in vitro, may also be a circulating tumor marker of neoplastic disease activity in endometrial carcinoma patients. Int J Radiat Oncol Biol Phys 19 (1990) 619-626.

[153]A. Daniele, R. Divella, P. Trerotoli, M.E. Caringella, A. Paradiso, P. Casamassima, I. Abbate, M. Quaranta, A. Mazzocca, Clinical usefulness of cancer Antigen 15-3 in breast cancer patients before and after surgery. Open Breast Cancer Journal 5 (2013) 1-6.

[154]M.J. Duffy, Serum tumor markers in breast cancer: are they of clinical value? Clin Chem 52 (2006) 345-351.

VITA

Srimeenakshi (Meenu) Srinivasan was born and brought up in Chennai, India, on April 26, 1981, the daughter of Jayalakshmi Srinivasan and T. Srinivasan. Following her graduation from Sri Sankara Matriculation Senior Secondary School in Chennai, India in 1998, Meenu received her Bachelor of Dental Surgery from Dr. Tamil Nadu M.G.R Medical University in 2004. She then received her Master of Science degree with a major in Molecular and Cell Biology from the University of Texas at Dallas in 2007. In August 2008 she joined the Ph.D. graduate program at The University of Texas Health Science Center at Houston Graduate School of Biomedical Sciences. She developed drug carriers for targeted delivery to breast cancer under the guidance and mentorship of Dr. Biana Godin and Dr. Mauro Ferrari.